TOOL WEAR ANALYSIS IN VARIOUS MACHINING PROCESSES AND
STUDY OF MINIMUM QUANTITY LUBRICATION (MQL)


By


Kyung Hee Park


A DISSERTATION


Submitted to
Michigan State University
in partial fulfillment of the requirements
for the degree of


DOCTOR OF PHILOSOPHY


Mechanical Engineering


2010

**ABSTRACT**

TOOL WEAR ANALYSIS IN VARIOUS MACHINING PROCESSES AND STUDY OF
MINIMUM QUANTITY LUBRICATION (MQL)

By

Kyung Hee Park

The tool wear analysis on the multilayer coated carbide inserts in turning and milling of
AISI 1045 steels was performed using advanced microscope and image processing techniques. In
turning process, the flank wear evolution, surface roughness and groove sizes on the coating
layers were analyzed to understand the flank wear mechanism(s) involved. The dominant wear
phenomenon was abrasion and, after carbide was exposed, adhesion took over. For flank wear
prediction, 2-body abrasion model was used along the interface conditions from finite element
(FE) model, which provides the temperature on the cutting tool. In a face milling study,
multilayer cutting tools, double (TiN/TiAlN) and triple (TiN/$Al_2O_3$/TiCN) layered coated
carbide, processed by physical vapor deposition (PVD) and chemical vapor deposition (CVD)
respectively, were evaluated in terms of various cutting conditions. Similar to the turning case,
abrasion was found to be the most dominant tool wear mechanism in milling. Edge chipping and
micro-fracture were the tool failure modes. Overall, the double layer coating was superior to the
triple layer coating under various cutting conditions due to the benefit coming from the coating
deposition processes themselves.

On the other hand, drilling of carbon fiber reinforced polymer (CFRP)/titanium (Ti)
stacks has been performed using carbide and PCD drills. The dominant wear mechanism for
carbide tools was the abrasion by fibers in CFRP drilling and Ti adhesion, covering entire cutting

edge while the main wear behavior of PCD drill was edge chipping. The adhesion of titanium seems to be the most important factor in tool wear and micro-chipping because the adhered titanium seems to be brushed away by the fibers in CFRP when drilling the composites, which accelerates tool wear in drilling of stacks. PCD drills have more wear resistance than carbide drills only in terms of the flank wear land. However, due to the inherent brittleness of PCD drills, chipping was observed at the tool edge when drilling titanium.

Finally, for a better understanding of Minimum Quantity Lubrication (MQL) and its effective use in practical industrial applications, MQL parameters such as droplet sizes, the droplet distributions and wetting angles of various types of lubricants were investigated. The measurement method of droplet size and distribution was proposed using confocal laser scanning microscopy (CLSM) and wavelet transform. In addition, the empirical droplet size estimation equation was also introduced for extremely small droplets, which are difficult to be measured. The distribution of the droplets has been also studied to determine the MQL optimal nozzle-workpiece distance and the nozzle discharge pressure. To extent the applicability of MQL to more aggressive machining conditions, a potential additive to MQL lubricant, which is a mixture of exfoliated nano-graphene particles and vegetable oil, have developed. Oil based lubricant, especially nano-enhanced vegetable oil, showed a better wettablility and tribological behavior. MQL-ball milling tests with nano-graphene enhanced lubricant were performed to show a remarkable performance improvement in reducing both central wear and flank wear as well as edge chipping.

To my wife, Jihyun,

my children, Suin, Jeongin, and Haein,

and my beloved family

# ACKNOWLEDGEMENTS

**TABLE OF CONTENTS**

# LIST OF TABLES

# LIST OF FIGURES

x

Chapter 1

# INTRODUCTION

Metal cutting is a complex process where many factors, such as machine tool, work material, tool material and machining conditions, have to be considered. Among the factors, tool wear is one of the most important aspects that affect product quality and cost in metal cutting process. Many research studies regarding of the tool wear have been carried out over 150 years. However, no significant work to understand the mechanism behind tool wear has taken place mainly due to the complexity in metal cutting process. Several tool wear types have been reported in metal cutting including abrasion [Ramalingam and Wright, 1981], adhesion [Wright and Bagchi, 1981], diffusion [Trent, 1963] and dissolution [Kramer and Kwon, 1985; Kramer and Suh, 1980]. In general, abrasive and adhesive wears dominate at low cutting temperatures while the chemical wear such as diffusion and dissolution are dominant at high cutting temperatures [Stephenson and Agapiou, 2006]. Thus, the dominant wear mechanism at flank surface due to relatively low cutting temperature compared to rake surface is abrasion while the combination of abrasion and dissolution wears takes place at rake surface. In addition, the abrasion is strongly dependent upon the hardness of a tool material; therefore, a harder coating can improve the tool life if the abrasive wear is dominant. With the wear mechanisms identified; the effort to develop physics based tool wear models has been made to predict tool life because an empirical approach, that has dominated tool wear studies, only relies on experimental tests for each combination of tool and work material [Rabinowicz, 1964, Wong et al. 2004, Park and Kwon, 2009, and Olortegui-Yume and Kwon, 2010]. Based on the physics based wear model, it is possible to describe tool wear behaviors of various combinations of work and tool material,

1

such as various alloys/composites and single/multilayer coated tools, respectively, without a significant amount of machining experiments.

This study deals with three aspects that directly related to tool wear, which are tool (coating) material, work material and machining process because understanding these aspects can eventually improve the productivity.

First, in chapter 2, the tool wear mechanism of multilayer coating is discussed for turning process. In general, it is known that the multi-layer coated carbide tools can improve the tool life [Cselle and Barimani, 1995, Olortegui-Yume and Kwon, 2007, and Olortegui-Yume et al., 2008]. However, the reason for the wear deterrence of multi-layered coating is not well established. Recently, in the case of turning of AISI 1045 steel with multi-layer (TiN/$Al_2O_3$/TiCN) coated carbide tools, the explanation has been made [Olortegui-Yume and Kwon, 2007 and Olortegui-Yume et al., 2008]. The reason is that the continuous turning process increases the cutting temperature high enough to activate the dissolution wear in addition to abrasive wear at rake. However, the $Al_2O_3$ coating is known to be resistant to the crater wear where the dissolution wear dominates while hard coatings such as TiCN exhibit excellent performance against abrasive wear. In addition, with the exposure of each coating, the locations of maximum cutting temperature, which coincide the location of maximum crater depth, change because the friction condition varies in terms of coating materials. This delays the crater wear evolution. On the other hand, at flank surface, the dominant wear mechanism is abrasion, which can be interpreted as only harder coating (TiCN) is required for flank wear [Park and Kwon, 2009]. In addition, it was commonly believed that the effectiveness of multilayer coating comes from the delay in the crack propagation [Sadik and Myrtveit, 2009] because the crack can propagate along the coating interfaces instead of right through the coatings into the substrate. Under the cyclic loading in

milling process, enhanced toughness and wear resistance against thermal and mechanical impact are required and again multilayer coating has been cited to improve the life of cutting tools [Cselle and Barimani, 1995].

Coatings are deposited onto carbide tools in a single-layer or multi-layer scheme processed by CVD and/or PVD techniques, which have advantages and disadvantages [Stephenson and Agapiou, 2006 and Soldergberg et al., 2001]. For example, CVD-$Al_2O_3$ in multi-layered coating provides thermal barrier and good bonding with other coatings. However, the brittle eta phase can be formed at the coating interface due to high deposition temperature, which could deteriorate the strength of the substrate and weaken the cutting edge. On the other hand, PVD coating process produces the sharp cutting edge and free thermal cracks on the cutting surface. In this regard, the coating materials along with the coating process must be determined depending on machining applications. Jawaid et al. [2000] found that the CVD coating tool was superior to the PVD coating tool due to high adhesion strength of the CVD coating tool despite of the inherent disadvantage from the CVD coating process. Dobranski et al. [2006] compared CVD and PVD in nitride tool ceramics on a 'pin-on disk' method and concluded that the multilayer coating, processed by CVD, was better due to the adhesion strength. Therefore, in chapter 3, tool wear of multilayer coating in milling is studied in terms of coating deposition processes.

In chapter 4, the drilling study of carbon fiber reinforced polymer (CFRP)/titanium (Ti) stack is presented because CFRP/Ti stack has been increasingly used in aerospace industry. However, drilling of CFRP/Ti stack is challenging due to the dissimilar machining characteristics of CFRP and Ti, where each requires the distinct optimal cutting condition. In fact, it is known that the ideal tooling solution for drilling Ti is not the most cost effective for CFRP

drilling while the ideal tooling solution for CFRP cannot cut Ti effectively. The different behaviors of the materials in the stack in drilling can often lead to severe tool wear, which often causes increased drilling forces, poor hole quality and large Ti burrs in CFRP-Ti stack drilling [Kim and Ramulu, 2004]. The CFRP can be a highly abrasive material depending on the direction of the fiber in the matrix while drilling for titanium causes high cutting temperature due to its low conductivity. Considering reduced assembly flow time, reduced cost and improved machined hole quality, tool wear in drilling CFRP/Ti stacks has to be minimized. The possible wear types on drill bits including flank wear, crater wear, chisel edge wear, margin wear and chipping wear were characterized [Kanai and Kanda, 1978, Sanjay et. al, 2005]. Rawat and Attia [2009] investigated the wear mechanism of a tungsten carbide drill in drilling of woven graphite epoxy composites at high cutting speed. The chipping and abrasion by the fractured graphite fibers and tungsten carbide grains lead to flank wear evolution which results in delamination and reduce the hole quality of the work material as well as the cutting forces. PCD tool showed much less wear rate and higher hole quality compared to HSS and carbide tools when drilling a graphite/bismalemide composite [Ramulu et al., 1999]. Sharif and Rahim [2007] observed from Ti drilling experiments with TiAlN-coated and uncoated carbides that TiAlN-coated carbide tools were superior to uncoated carbide tools in terms of flank wear at various cutting speeds and both drills showed similar tool failure modes such as chipping and catastrophic failure. A PCD drill can fracture when drilling Ti at high cutting speeds mainly due to the brittleness of the PCD tool [Garrick, 2007].

In chapter 5, the minimum quantity lubrication (MQL) machining process is discussed. MQL has been applied to reduce the cost associated with the maintenance and disposal of the fluid being used and the conformation to environmental policies [Ueda et al., 2006 and Rahman

et al., 2002]. In MQL, the high pressurized air sprays micro-scale lubricant droplets onto the tool-work interface. Even though it is very promising for many machining applications, several fundamental issues associated with MQL such as optimal operation conditions have not been addressed [Park et al., 2008]. The most important point in MQL is that the lubricant must adequately cover the contact areas, i.e., tool-chip and tool-work interfaces. And another important variable is the wettability of the lubricant on the tool surface. On the other hand, the optimal MQL application conditions such as air pressure, nozzle direction, distance, etc., have to be determined for its effective use prior to machining applications. Therefore, a better understanding of the application conditions such as droplet size and distribution, air pressure, nozzle distance, and flow rate is needed to be effective in industrial applications. Thus, a great interest exists in the machining community in the development of a convenient technique to measure the droplet size. The smaller droplet, which can provide better penetration into the cutting surface, are more preferable especially for micro machining applications, where the cutting surface is relatively small [Jun et al., 2008].

Finally, chapter 6 studies the effect of the MQL lubricant including exfoliated nano-graphene enhanced vegetable oil by conducting wetting angle measurement, friction tests using a ball-on-disk set-up and MQL ball milling test. Several works have been published to evaluate the characteristics of various lubricants for finding optimum lubricants, e.g. oil film on water droplet, in MQL machining [Heinemann et al., 2006, Itoigawa et al., 2006 and Yoshimura et al., 2005]. In addition, solid lubricants (nano-sized) such as molybdenum disulfide ($MoS_2$), graphite and boron nitride have been developed as a lubricant itself or as an additive for lubricant [Jianxin et al., 2009, Krishna and Rao, 2008, Xu et al., 2004 and Reddy and Rao, 2006]. Especially nano-graphene enhanced lubricants are expected to provide better performance because nano-graphene

has not only a higher dissociation temperature but also the high aspect ratio, which naturally orients the graphene phase for better lubricity when applied through MQL process. Therefore, in this chapter, the wetting angles for a variety of commercially available lubricants including nano-graphene enhanced oil were tested to evaluate the wettability of lubricants. And the friction coefficients of each lubricant and a dry nano-graphene coated insert were measured as a function of load and speed. Finally, ball milling tests were performed to evaluate the proposed nano-graphene enhanced lubricant in a practical machining application.

This research work investigates tool wear mechanisms at flank surface in various machining processes, such as turning, milling and drilling, using the combination technique of CLSM and image processing technique including wavelet transform. This technique enables us to characterize 3D topographic profile on flank and ultimately obtain the tool wear evolution in cutting times or distances. In addition, in case of turning test, 2-body abrasive model along with FEM simulation predicts the flank wear and compares with experimental results. On the other hand, a new technique is proposed to measure the droplet sizes and distributions for a typical MQL process after the droplets have been sprayed onto the polished silicon wafer surface. Furthermore, MQL parameters such as wetting angle, nozzle distance and air pressure, which may affect the machining efficiency, are evaluated for optimal MQL conditions. To evaluate the effect of MQL, ball milling test, based on the MQL parameters determined, is also performed in both dry and MQL conditions in addition to tribological test.

## 1.1 TOOL WEAR TYPES

### 1.1.1 Abrasion

Abrasive wear takes place by hard inclusion in work material, which results in the scoring marks on the tool surface (See Figure 19). In the pearlitic microstructure, 2-body abrasion occurs because a complex morphology of the second phase is constrained within a matrix of ferrite while 3-body abrasion can be used because the hard second phase rolls at the cutting interface face. The 2-body and 3-body abrasive wear models were developed by Rabinowicz [1964]. For 2-Body abrasion, the wear volume, $V_{2B}$, is determined to be

$$V_{2B} = \frac{x \cdot F \cdot \tan\theta}{\pi \cdot H_t} \qquad (1)$$

For 3-Body abrasion, the wear volume, $V_{3B}$, is determined to be

$$V_{3B} = \frac{x \cdot F \cdot \tan\theta}{3 \cdot H_t} \quad ; \quad \frac{H_t}{H_a} < 0.8$$

$$V_{3B} = \frac{x \cdot F \cdot \tan\theta}{5.3 \cdot H_t}\left(\frac{H_t}{H_a}\right)^{-2.5} \quad ; \quad 0.8 < \frac{H_t}{H_a} < 1.2 \quad , \quad (2)$$

$$V_{3B} = \frac{x \cdot F \cdot \tan\theta}{2.43 \cdot H_t}\left(\frac{H_t}{H_a}\right)^{-6} \quad ; \quad \frac{H_t}{H_a} < 1.25$$

where $x$ is the sliding length, $F$ is the load between interacting surfaces, $\theta$ is the average roughness angle of the abrasive, $H_t$ is the hardness of the abraded material, $H_a$ is the hardness

of the abrasive. For the abrasive model, hot hardness data for coating materials and abrasives

(Fe$_3$C for low alloy steels) are required [Kwon and Kountanya, 1999; Kwon, 2000; and Wong et

al., 2004] as seen in Figure 1.
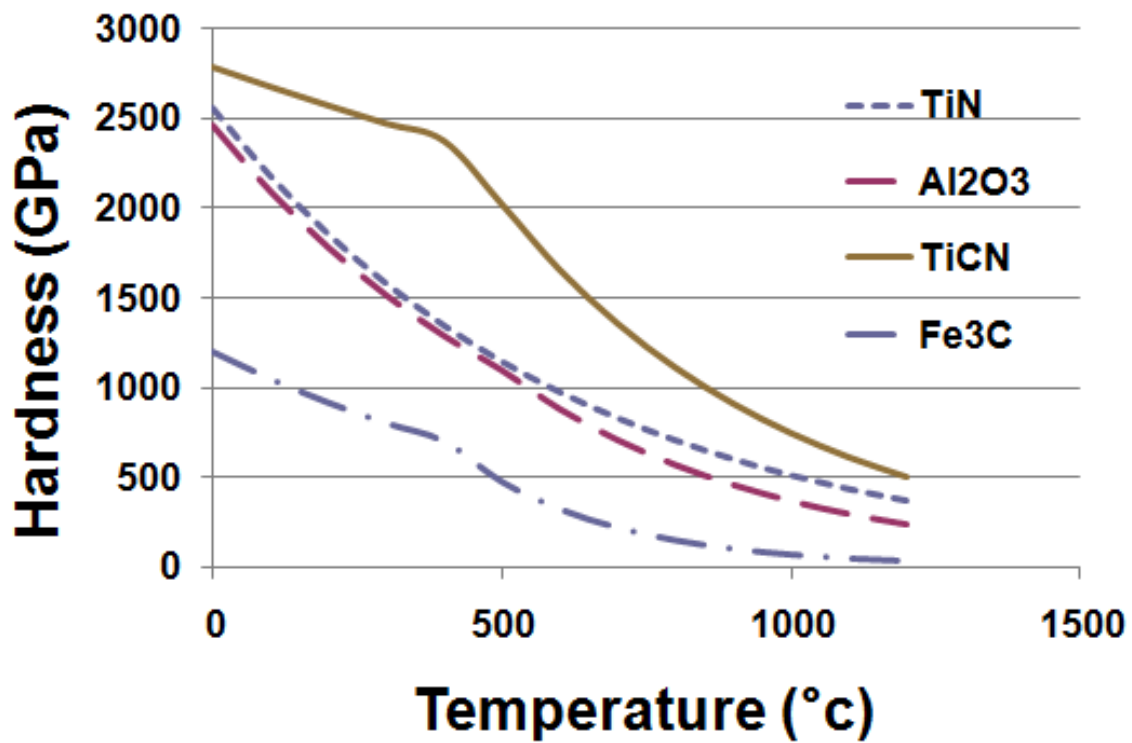


**Figure 1 Hardness of cementite and coating materials**
**(For interpretation of the references to color in this and all other figures, the**
**reader is referred to the electronic version of this dissertation.)**

**1.1.2 Adhesion**

Adhesive wear takes place when one solid material is sliding over the counteracting surface. The interaction between two surfaces can be represented by the metallurgical weld or adhesion joint (See Figure 17 (a)). Adhesive wear takes place by pulling out discrete pieces from the surfaces as they are sliding and separated [Rabinowicz, 1995]. In addition, Rabinowicz, [1964] found the quantitative laws of adhesive wear from the experiment as follows; the amount of wear (1) is directly proportional to the load L between interacting surfaces, (2) proportional to the distance slid $x$; and (3) inversely proportional to the hardness p of tool material being worn away. In metal cutting, adhesion may occur because the work material or the wear debris from the work material forms strong bonds (junction) with the tool under the high interfacial pressure and temperature. If the failure strength of the junction formed is larger than the local failure strength of one of the sliding surfaces, then, the junction will be detached from the surface with the lower failure strength. Thus, Adhesive wear will occur if the lowest failure strength happens to be on the tool. Adhesive wear peaks at intermediate temperatures due to low adhesion tendency at low temperatures and thermal softening at high temperatures [Childs et al., 2000].

**1.1.3 Dissolution**

Dissolution wear occurs at a rake surface due to high cutting temperature generated by severe machining condition. In dissolution wear, the species from the tool material forms a solid solution within the chip. As the chip passes, tool material is constantly removed from the rake face. Dissolution wear depends on the chemical inertness of the tool material as well as the chemical affinity between tool component and work material. A quantitative model was developed by [Kramer 1979, and Kramer and Suh, 1980]. For a given ternary tool material of

composition, $A_xB_yC_z$, the chemical solubility was obtained from thermo-dynamic

equilibrium condition,

$$\Delta G_{A_xB_yC_z} = x\Delta\overline{G}_A + y\Delta\overline{G}_B + z\Delta\overline{G}_C , \qquad (3)$$

where $\Delta G_{A_xB_yC_z}$ is the free energy of formation of the tool material at the interface of chip

and tool, $T$ is the solution temperature, and $\Delta G_i$ ($i = A, B,$ or $C$) is the relative partial molar

free energy of component $i$ within the solution and can be expressed as

$$\Delta\overline{G}_i = \Delta\overline{G}_i^{xs} + RT\ln S_i , \qquad (4)$$

where $\Delta\overline{G}_i^{xs}$ is the molar excess free energy of component $i$ in the solution, $R$ is the universal

gas constant, $T$ is the temperature in Kelvin, and $S_i$ is the solubility concentration of species $i$

in mole fraction. From Eq. (4) and data on $S_i$ at some given $T$, the excess free energy of

component $i$ into the matrix of a work material can be estimated. Furthermore, $\Delta\overline{G}_i^{xs}$ is taken

as a constant in the low limit of solubility (Henry' law). For example, a binary compound, TiN,

has only two terms in the evaluation of free energy of formation as $\Delta G_{A_xB_y} = x\Delta\overline{G}_A +$

$y\Delta\overline{G}_B$ , where $A$ =Ti, $x$ =1, $B$ =N and $y$ =1. Finally, with the definitions of

$$\Delta G^{xs} = x\Delta\overline{G}_A^{xs} + y\overline{\Delta G}_B^{xs} + z\overline{\Delta G}_C^{xs}$$ , $M = x \cdot \ln x + y \cdot \ln y + z \cdot \ln z$ and

$N = x + y + z$ , the chemical solubility, $S_{A_xB_yC_z}$, of a tertiary coating material,

$A_xB_yC_z$, in a work material (in mole fraction):

$$S_{A_xB_yC_z} = \exp\left(\frac{\Delta G_{A_xB_yC_z} - \Delta G^{xs} - RTM}{NRT}\right) \quad (5)$$
,

The dissolution of a tool material is assumed to obey Henry's law because the amount of tool material dissolved into chip during the cutting process is small enough to be considered dilute. Dissolution wear has been successful to predict the tool wear in carbide tools, coated carbide tools [Wong et al., 2004 and Olortegui-Yume, 2009].

## 1.2 IMAGE PROCESSING TECHNIQUE

The important characteristic of CLSM is the confocal aperture which eliminates the reflected light from above and below the focal plane, thus obtaining surface information from a very thin "optical slice" of the surface is feasible. Surface reconstruction is achieved by storing and manipulating a stack of optical slices within a set of the vertical travel of the stage. The final output of the built-in software in confocal microscopes is a z-matrix ($z(x,y)$) containing the height information of the surface. For a better handling of the image data, the z-matrix is encoded in a grayscale, called height encoded (HE) image. Along with HE images, maximum brightness (MB) images, which are extended depth of field views, can be also obtained. It is

important to note that most confocal systems can work in both confocal and optical

(conventional) modes. The basic configuration of CLSM is shown as in Figure 2.
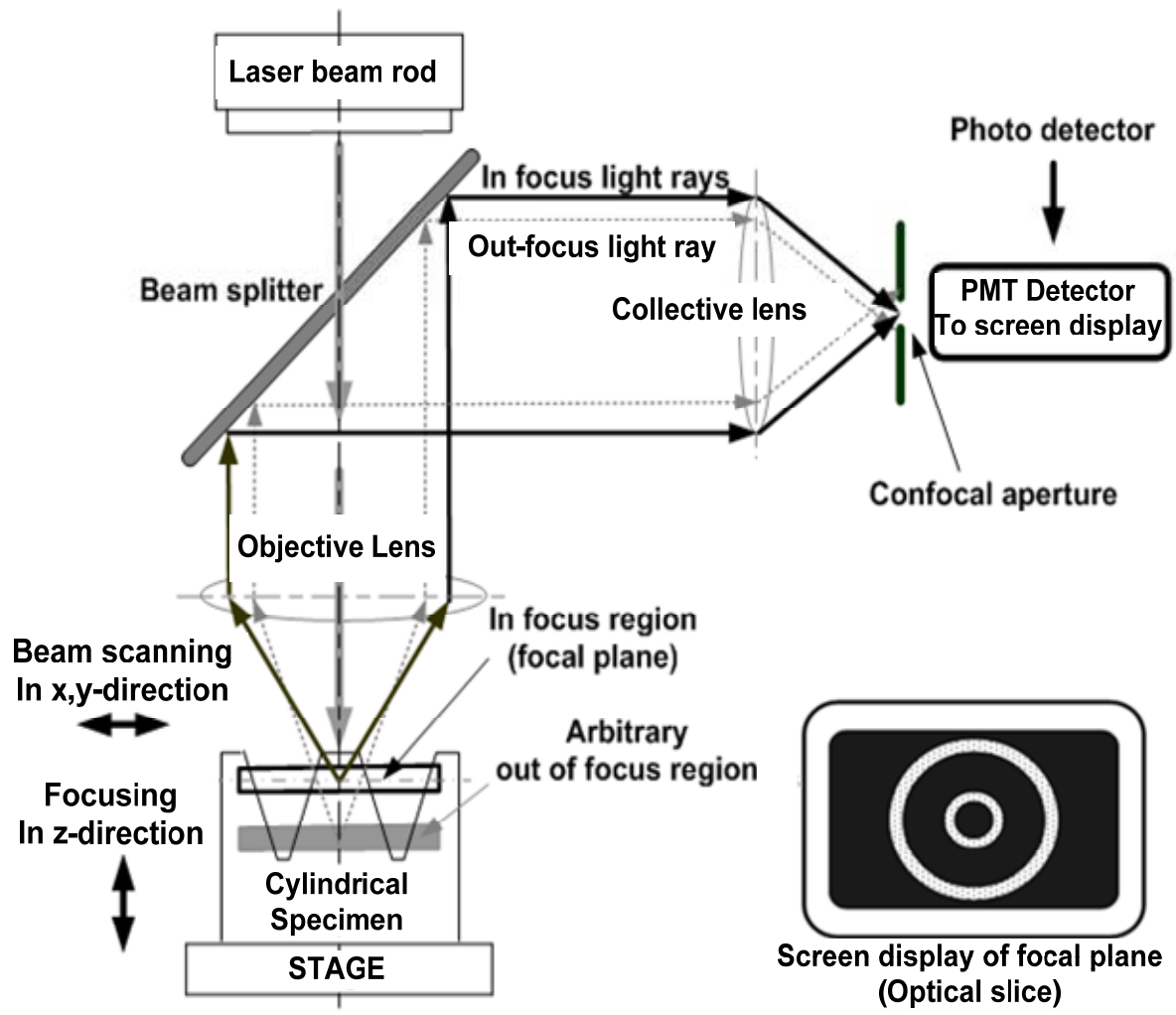


**Figure 2 Typical configuration of CLSM [Olortegui-Yume and Kwon, 2007]**

## 1.3 2D WAVELET TRANSFORM

Many works have been carried out for surface analysis using wavelet transform [Lee et al., 1997, Jiang et al., 1999, Raja et al., 2002, and Fu et al., 2003]. The key advantage of the wavelet transform is the capability of decomposition of the surface profile to various wavelength regimes, which represent the surface conditions such as roughness, waviness and form, while maintaining the surface details [Raja et al., 2002, and Olortegui-Yume and Kwon, 2010]. During the decomposition process, mother wavelet, which can be determined based on characteristic of the surface texture, is required. Using the mother wavelet chosen, for example, 1D discrete wavelet transform (DWT) can bring out two coefficients, approximation and detail, at each level while decomposition process with two channel filter banks, low-pass and high-pass filters in multi-resolution (MR) scheme. By reverse process of the decomposition, called reconstruction or inverse discrete wavelet transform (IDWT), the coefficients obtained can be transformed into the approximation and detail, which are related to the "filtered" surface profile, "form", (low frequency) and surface waviness/roughness (medium to high frequency), respectively [Jiang et al., 1999, Josso et al., 2002, and Yuan et al., 2005]. For 3D topography, in similar way, 2D DWT analysis decouples raw 3D data to 4 sets of wavelets coefficients, which are called approximation (CA), horizontal details (CH), diagonal details (CD) and vertical details (CV) as shown in Figure 3. The surface can be transformed as many levels as possible without losing the original shape. Then 2D IDWT or 2D wavelet analysis reconstruction for these coefficients are needed to obtain the approximation (A), horizontal (H), diagonal (D) and vertical (V) details (See Figure 9 (b)). For the surface roughness analysis, roughness, waviness and form have to be defined in terms of wavelet decoupled components (A, H, D and V). From the literature [Olortegui-Yume and Kwon, 2010, and Jiang et al., 1999], the roughness can be defined as the

sum of details (H+D+V) up to the cut-off level where the scoring mark is observed. In addition, the approximation at the cut-off level can be considered as form. In this work, 2D-DWT is used in a multi-resolution scheme with a two-channel filter bank based on a chosen mother and scaling wavelet [Rioul and Vetterli, 1991] as in Figure 4.



Lo: low-pass fileter
Ho: high-pass filter     $cA_0 = s$     for the decomposition initialization
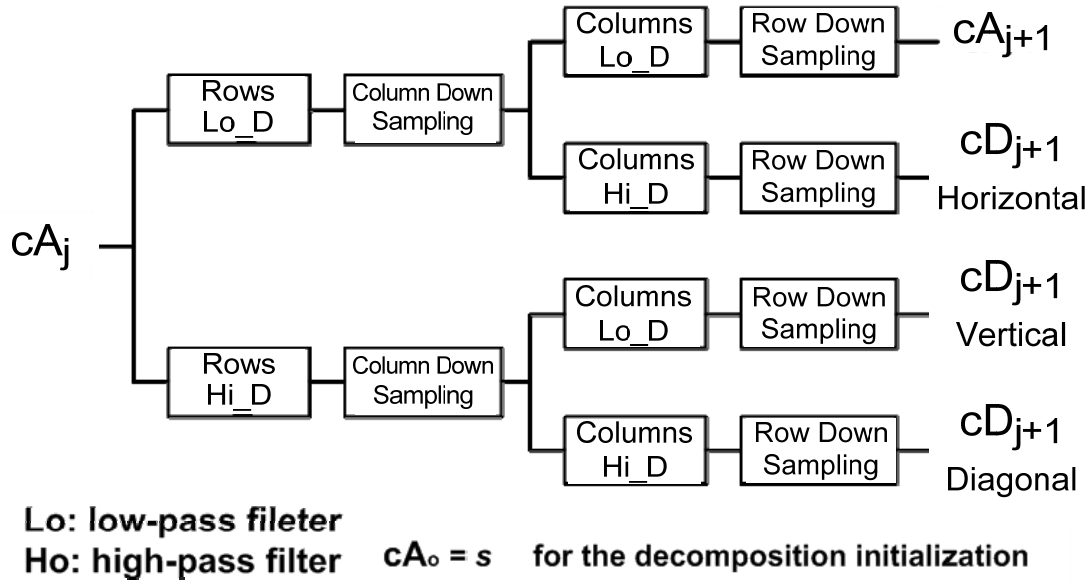
**Figure 3 Decomposition step of two-dimensional discrete wavelet transform**
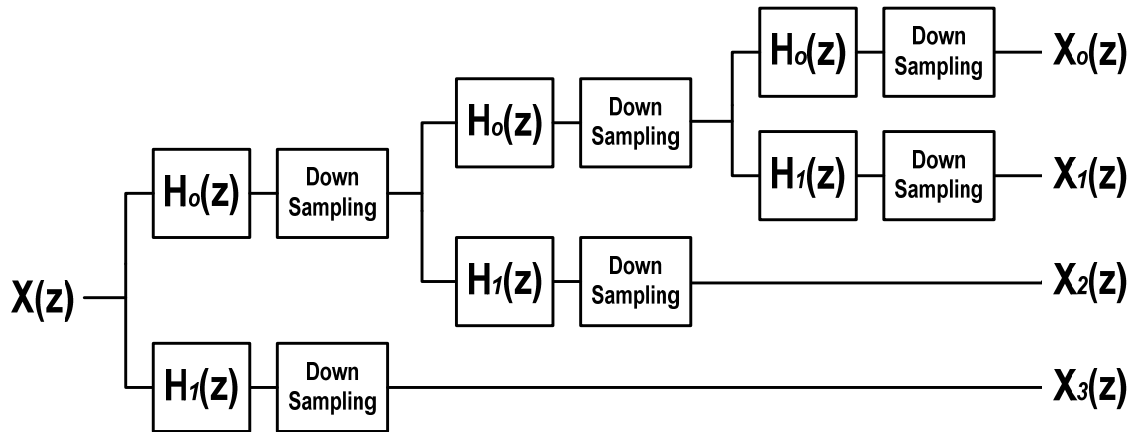


(a) Wavelet decomposition filter bank

**Figure 4 Representation of wavelet filter bank (a) decomposition and (b) reconstruction**

**Figure 4 (cont'd)**
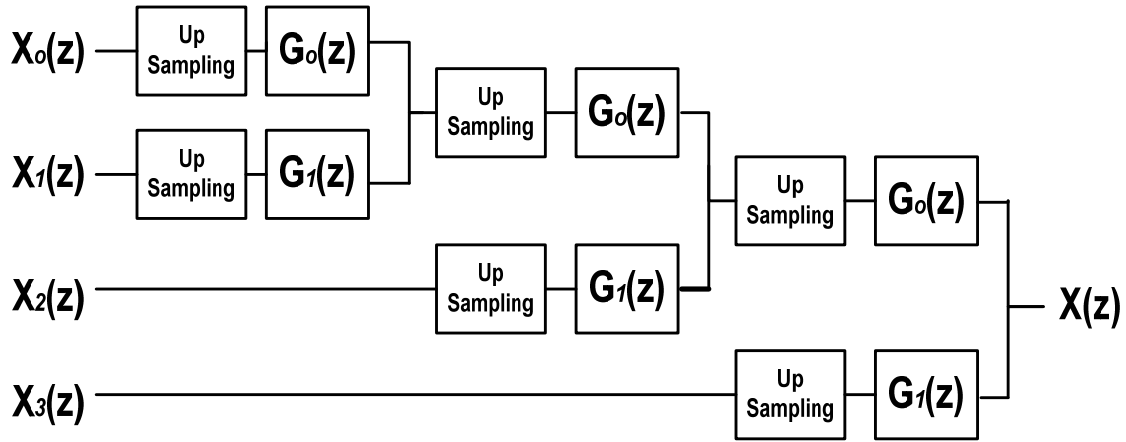


(b) Wavelet reconstruction filter bank

## 1.4 FEM SIMULATION

In the development of flank wear model, the interfacial temperature at the cutting zone is required since the tool wear is strongly dependent on the cutting temperature. However, the interfacial condition can be determined neither experimentally nor theoretically. Thus, Finite Element (FE) simulation of machining process has been widely used for obtaining the temperature on the cutting surface. In addition, Arbitrary Lagrangian Eulerian (ALE) formulation in the adaptive mesh technique has been also utilized for maintaining the high quality mesh throughout the simulation due to the severe mesh deformation associated with the machining process. The multi-layer coated tool can be modeled as a thermally 'equivalent' conductivity of a single composite coating layer on carbide instead of modeling each layer individually because of the difficulty in modeling thin coating layers. This simplification is justified as the simulation with the composite coating showed similar results with individual

coating layers under the same cutting conditions [Yen et al., 2004, and Olortegui-Yume et al., 2008].

The J-C constitutive model, suited for the simulation of metals subjected to large strains, high strain rates and high temperature, is used for AISI 1045 steel. It can be expressed as

$$\sigma = (A + B\varepsilon^n)(1 + C\ln\dot{\varepsilon}^*)(1 - T^{*m}), \qquad (6)$$

where is the stress, $\varepsilon$ is the equivalent strain, $\dot{\varepsilon}^* = \dot{\varepsilon}/\dot{\varepsilon}_0$ is the dimensionless strain rate

($\dot{\varepsilon}_0$=1.0s$^{-1}$) and *A*, *B*, *C*, *n* and *m* are the material constants from [Ozel and Zeren, 2005].

$T^{*m}$ is equal to $(T - T_r)/(T_m - T_r)$ where $T_r$ is a reference temperature (25°C)

and $T_m$ is the melting temperature of the workpiece.

Chapter 2

**FLANK WEAR OF MULTILAYER COATED CARBIDE TOOL AND WEAR
PREDICTION USING 2-BODY ABRASIVE WEAR MODEL**


Flank wear is one of the most important aspects that affect tool life and product quality in

machining process. However, only few works were published to identify the mechanism behind

flank wear mainly due to the complexity in metal cutting process. At the present time, a

dominant flank wear mechanism is believed to be the abrasion by the hard inclusions in a work

material, which results in the scoring marks on the flank surface [Ramalingam and Wright, 1981].

Recently, 2-body and 3-body abrasion models have been developed for the tool wear prediction

in turning of pearlitic and spherodized steels with various coated carbides [Wong et al., 2004]. It

was observed that the 3-body wear model shows an excellent agreement with the experiment

results of spherodized steels while the 2-body model predicts the flank wear trend for pearlitic

steel with some deviations due to the phase transformation during cutting.

Another important wear mechanism for flank wear is adhesion. This type of wear can

take place when one solid material is sliding over the counteracting surface. The interaction

between two surfaces can be represented by the metallurgical weld or adhesion joint. Adhesive

wear takes place by pulling out discrete pieces from the surfaces as they are sliding and separated

[Rabinowicz, 1964]. On the other hand, excessive localized wear at the depth of cut line on the

flank surface is called notch wear. The main concern for the notch wear is that it often leads to

catastrophic tool failure during the machining. Chandrasekaran and Johansson, [1994]

investigated the mechanisms for notch wear in machining of various austenitic stainless steels

with cemented carbide tools. They concluded that the sequence of the severe shear deformation

and lateral extension of the chip leads to excessive abrasion or adhesion wear between the deformed chip and the tool insert at the notch region.

In the development of flank wear model, the interfacial temperature profile at the cutting zone is essential since the tool wear is strongly dependent on the cutting temperature. However, the interfacial condition can be determined neither experimentally nor theoretically. Thus, Finite Element (FE) simulation of machining process has been widely used for obtaining the temperature on the cutting surface. In addition, Arbitrary Lagrangian Eulerian (ALE) formulation in the adaptive mesh technique has been also utilized for maintaining the high quality mesh throughout the simulation in order to avoid the severe mesh deformation associated with the machining process. The multi-layer coated tool can be modelled as a thermally 'equivalent' conductivity of a single composite coating layer on a carbide tool instead of modelling each layer individually because of the difficulty in modelling thin coating layers. This simplification is justified as the simulation with the composite coating showed similar results with individual coating layers under the same cutting conditions [Yen et al., 2004 and Olortegui-Yume et al., 2008].

Olortegui-Yume and Kwon [2010] have conducted a combined experimental and analytical study to reveal the benefit of multilayer coatings for crater wear based on turning experiment with multilayer ($TiN/Al_2O_3/TiCN$) coated carbide, the followings have been concluded,

1. The effectiveness of the multilayer comes from the changes in interface conditions as each layer is exposed. As each layer is exposed, the maximum wear location changes instead of concentrating on one location. This extends the tool life substantially.

2. The middle layer, $Al_2O_3$, resisted tool wear at relatively high cutting speeds due to the excellent resistance against dissolution wear while TiCN provided an excellent resistance against abrasive wear. Therefore, the multilayer coating made of $Al_2O_3$ and TiCN provides the combined effect to resist crater wear whose wear mechanism is a combination of abrasive and dissolution wear.

Does the multilayer coating deter the progress of flank wear? It was reported that the benefit of the multilayer coating is realized by the crack propagation through the coating interfaces, rather than into the cutting tool [Cselle and Barimani, 1995 and Paskvale, 2007]. This conjecture is proved to be false for the crater wear [Olortegui-Yume and Kwon, 2010]. This paper explores if this conjecture works for flank wear.

This chapter studies the flank wear of multi-layered coating using the various microscope techniques, 2D wavelet filtering and FE simulation. The flank wear rate and wear evolution are analyzed and the relationship between the roughness on the tool surface and flank wear are investigated. The abrasion model uses hot hardness data based on the temperature profiles from FEM simulation, which allows us to predict flank wear patterns as a function of cutting time. In addition, the flank wear predicted with the 2-body abrasion model are compared with the experimental data for the validation.

## 2.1 FLANK WEAR MODEL AND IMAGE PROCESSING TECHNIQUE

### 2.1.1 Abrasive wear model

The dominant wear phenomenon on the flank surface is abrasion by hard inclusion, cementite, which results in groove on the tool surface. In the pearlitic microstructure, 2-body abrasion occurs because a complex morphology of the second phase is constrained within a matrix of ferrite. In this work, The 2-body abrasive wear models was used (see Chap. 1.2.1) For the abrasive model, hot hardness data for coating materials and abrasives, which are shown in Figure 1, were used [Wong et al., 2004]. In addition, wear constants were determined by conducting calibration based on cutting experiments in conjunction of FEM temperature profiles. For validation, the predicted wear evolution was compared with experimental measurements.

### 2.1.2 Finite element model

FE metal cutting simulation was carried out using ABAQUS/Explicit version 6.6 to determine the interfacial temperature profiles between flank surface and work material at the various flank wear land ($V_B$) (from 70μm to 300μm). The flank wear land ($V_B$) was defined as in Figure 5 (a) in the FE model used. The Johnson-Cook (JC) constitutive model was adapted to model the work material and ALE adapted meshing technique was used to avoid severe mesh distortion. In addition, extremely fine meshes were applied around the interface between cutting tool and work piece. Four node bilinear displacement and temperature quadrilateral elements (CPE4RT), which has been used in other metal cutting simulation studies [Ozel and Zeren, 2005, Nasr et al., 2007 and Madhavan and Adibi-Sedeh, 2005], were used. A single composite coating

on top of the carbide has the 'equivalent' conductivity by combining thermal conductivity of

individual coatings (TiN/Al$_2$O$_3$/TiCN) [Yen et al., 2004]. The cutting tool with the composite

coating layer was assumed as a mechanically rigid and thermally conductive body. Boundary

conditions and initial temperature are shown in Figure 5 (b). The coefficients for JC constitutive

model and material properties of tool and work material are summarized in Tables 1 and 2,

respectively [Olortegui-Yume et al., 2008]. The simulation results, mainly interfacial

temperature, were fed to the abrasive wear prediction models.
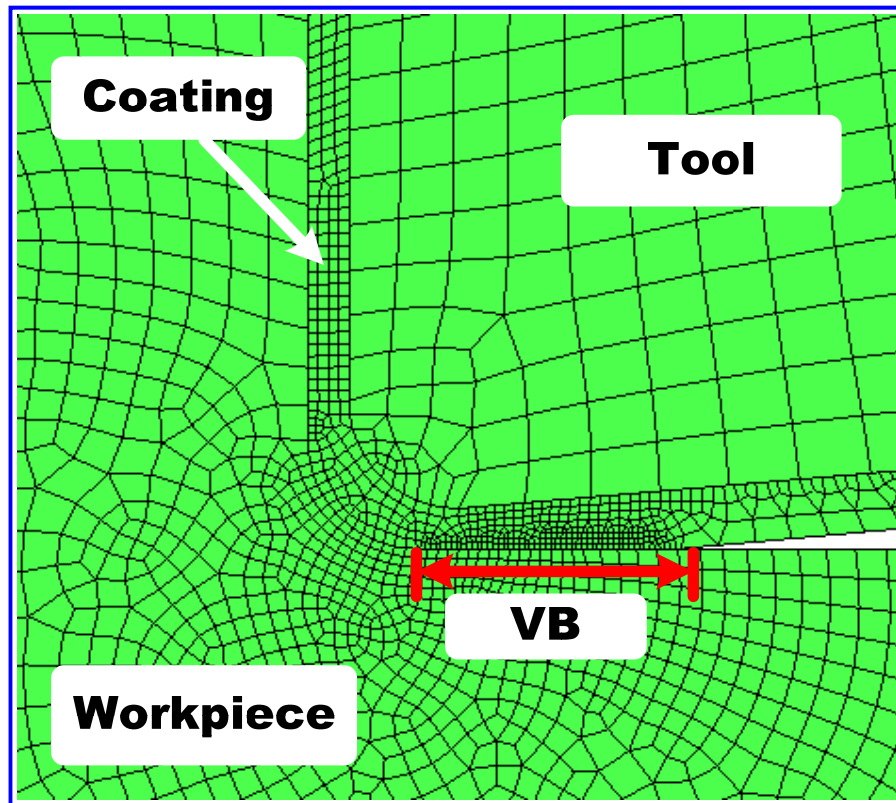


(a) Flank wear land (V$_B$) in FEM model

**Figure 5 Flank wear land (V$_B$) and boundary conditions for FE simulation**

**Figure 5 (cont'd)**
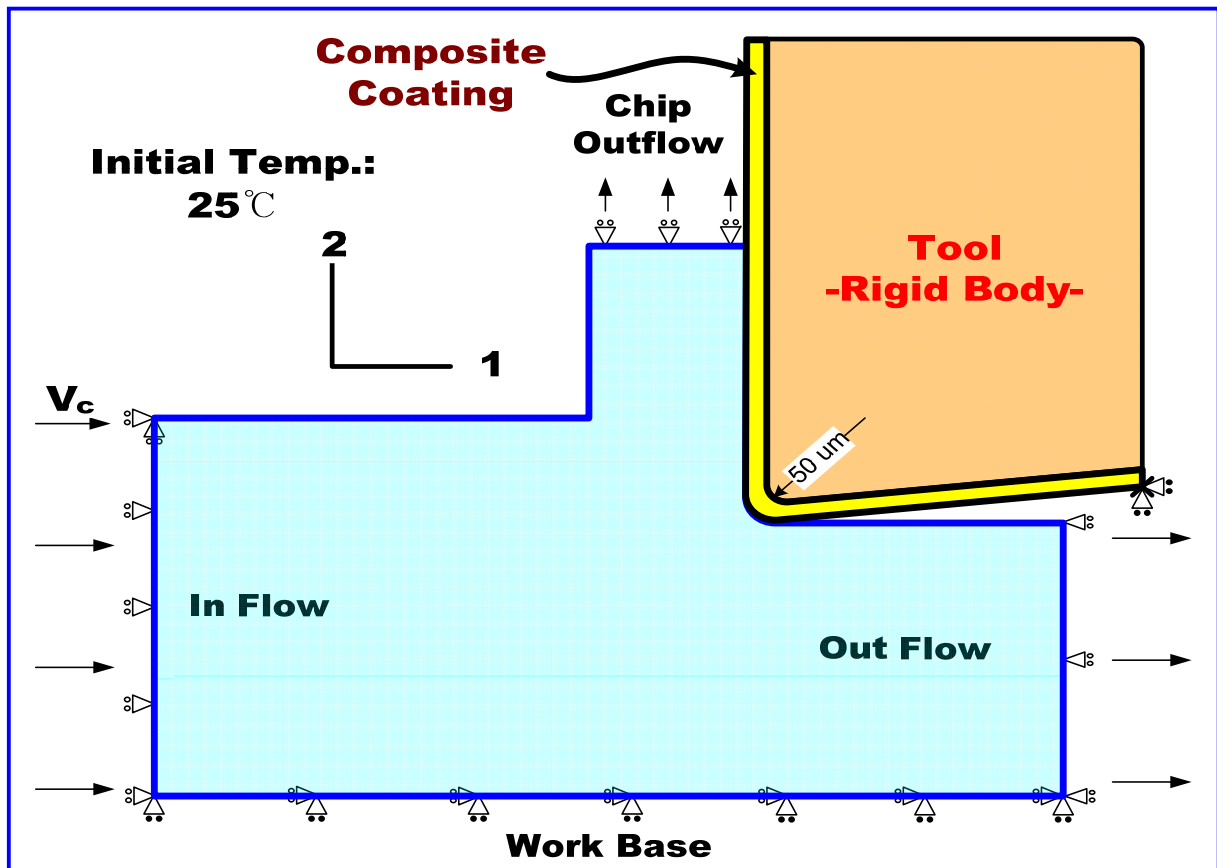


(b) Boundary conditions

**Table 1 Material constants for the JC model**

| A (MPa) | B (MPa) | C | n | M | $T_m$ |
|---------|---------|-------|-------|---|-------|
| 553.1 | 600.8 | 0.0134 | 0.234 | 1 | 1460 |

**Table 2 Material properties of tool and work material**

|  | AISI 1045 | WC-Co |
|---|---|---|
| Young's modulus (GPa) | 212 (20°C)<br>207 (100°C)<br>192 (300°C)<br>175 (500°C) | 612 |
| Poisson's ratio | 0.3 | 0.22 |
| Density (kg/m$^3$) | 7844 | 11900 |
| Conductivity (W/m°C) | 50.7 (100°C)<br>41.9 (400°C)<br>30.1 (700°C)<br>26.8 (1000°C) | 86 |
| Specific heat (J/kg°C) | 486 (75°C)<br>548 (275°C)<br>649 (475°C)<br>770 (675°C)<br>548 (875°C) | 334.01<br>+0.12T(°C) |
| Thermal Expansion (μm/m°C) | 11.9 (20°C)<br>12.5 (100°C)<br>13.6 (300°C)<br>14.5 (500°C)<br>15.1 (700°C) | 4.9 (200°C)<br>5.2 (400°C)<br>6.5 (600°C) |

**Coating materials**

|  | TiN | TiN/Al$_2$O$_3$/TiCN |
|---|---|---|
| Young's modulus, E (GPa) | 250 |  |
| Poisson's ratio, ν | 0.25 |  |
| Density , ρ (kg/m$^3$) | 4650 |  |
| Thermal Expansion, α (μm/m°C) | 9.4 |  |
| Conductivity, K (W/m°C) |  | 22/26/27 (25°C)<br>23/18/30.5(200°C)<br>26/8/34 (727°C)<br>26.5/4/35 (927°C)<br>27/6/36 (1200°C) |
| 'Equivalent' Conductivity, (W/m°C) |  | 25.9 (25°C)<br>22.21(200°C)<br>12.96 (727°C)<br>7.25 (927°C)<br>10.33 (1200°C) |

## 2.1.3 Image acquisition and wavelet transform

A JEOL JSM-6400 SEM, which includes both secondary electrons (SE) and backscattered electrons (BSE), and a CLSM (Zeiss LSM210) were used for the flank wear analysis at cutting times. The flank wear images taken by SEM can be mainly used for the measurement of flank wear land ($V_B$) and the observation of the wear evolution (behavior) for the coating materials. On the other hand, CLSM can provide the height information (3D surface profile) of the tool surface with high axial resolution (50nm) by an axial optical slicing process throughout the surface from top to bottom of the surface height [Yuan et al., 2005 and Olortegui-Yume and Kwon, 2010]. For each optical section, the maximum brightness, which is associated with the surface profile, is detected at a focal plane and stacked up to total number of the sections so that the HE image can be built up with a series of these optical sections. In this study, for the 3D topography of the flank surface, HE images, corresponding to each maximum bright (MB) images, were obtained with an objective of 50X as shown in Figure 6 (a) and (b). The 200 optical sections with a step size of 200nm were used for high accurate surface profile.

In present work, the HE images were obtained from CLSM and wavelet denoising technique was used to eliminate the noise and artifacts in HE raw image (See Figure 6 (c)). Finally, the wavelet-filtered wear profiles (See Figure 6 (d)) were obtained for analysis of the flank wear mechanism. In addition, roughness analysis on the tool surface was performed. The mother wavelet, Daubechies20 ('db20'), was chosen for 2D DWT from the reference [Olortegui-Yume and Kwon, 2010].
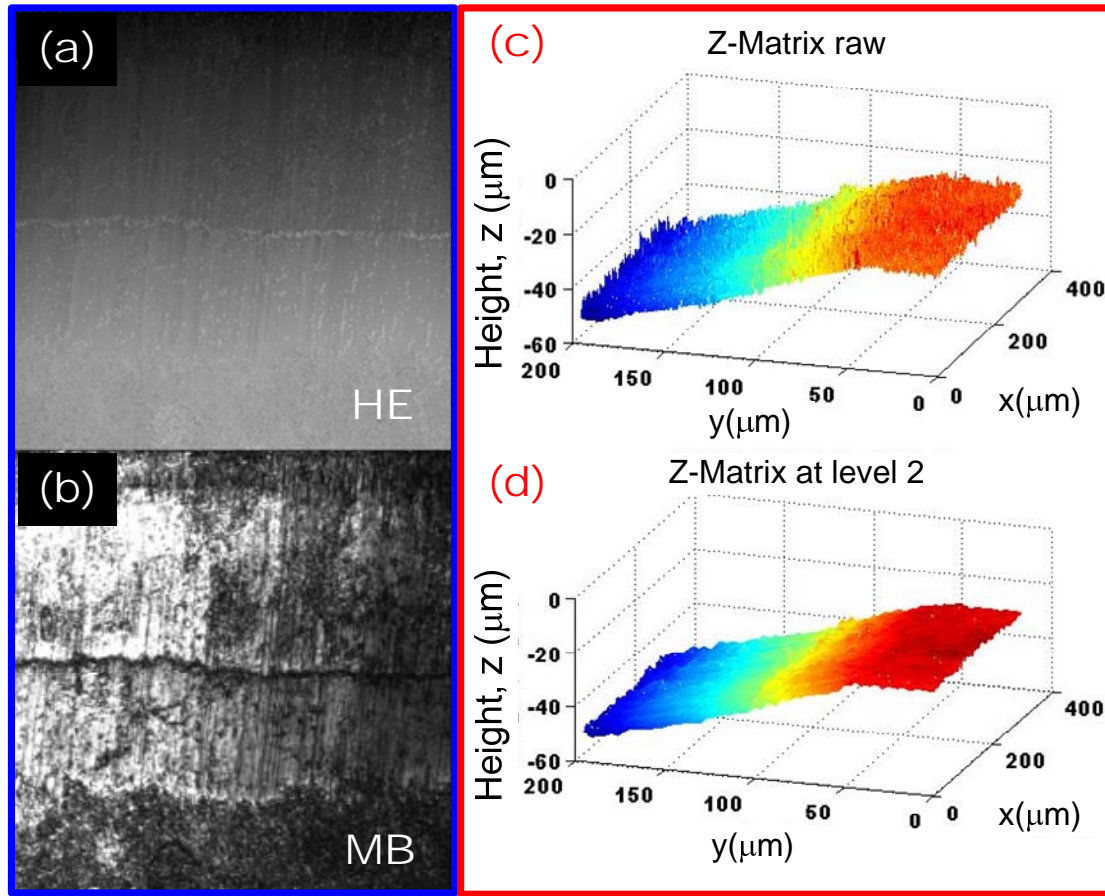
**Figure 6 (a) HE and (b) MB images from CLSM at 7min cutting time and (c) raw z-matrix and (d) wavelet filtered images from HE image**

## 2.2 EXPERIMENTAL SETUP

To study the wear mechanisms on the flank surface, turning tests with refined AISI 1045 steel were performed at the cutting time of 1, 2, 3, 4, 7, 10, 12, 20 and 23 min, where each test was starting from a fresh insert corner. A multilayer coating (SNMA 190612 - ISO) on C6 cemented carbide for substrate (KC9315 grade) was used. For multilayer coating, TiCN coating layer was deposited on the carbide substrate followed by $Al_2O_3$ and TiN layers. The thicknesses

of each coating are shown in Table 3. The cutting conditions consist of cutting speed, feed rate and depth of cut (DOC), which are 250m/min, 0.3175mm/rev and 1.905mm, respectively.

**Table 3 Thickness of the coatings**

| Coating Materials | TiN | $Al_2O_3$ | TiCN |
|---|---|---|---|
| Thickness | 1.940μm | 9.160μm | 7.584μm |

**2.3 RESULTS AND DISCUSSION**

Figure 7 illustrates the SEM images of flank wear land with the 60X objective at each cutting time. The flank wear land ($V_B$) was uniformly distributed throughout the cutting edge up to the cutting time of 12 min. However, the wear increased substantially at the notch region at 20 min and 23 min. On the other hand, BSE was obtained, as shown in Figure 8 to characterize the wear evolution on the coatings at cutting times. Wear took place mostly on the alumina ($Al_2O_3$) coating, which is shown black in the BSE images, from 1 min to 3 min and then titanium carbon nitride (TiCN) coating started to be exposed at 4 min. The carbide substrate was exposed after 12 min and the carbide layer was entirely covered by the steel (see 20 and 23 min in Figure 8).
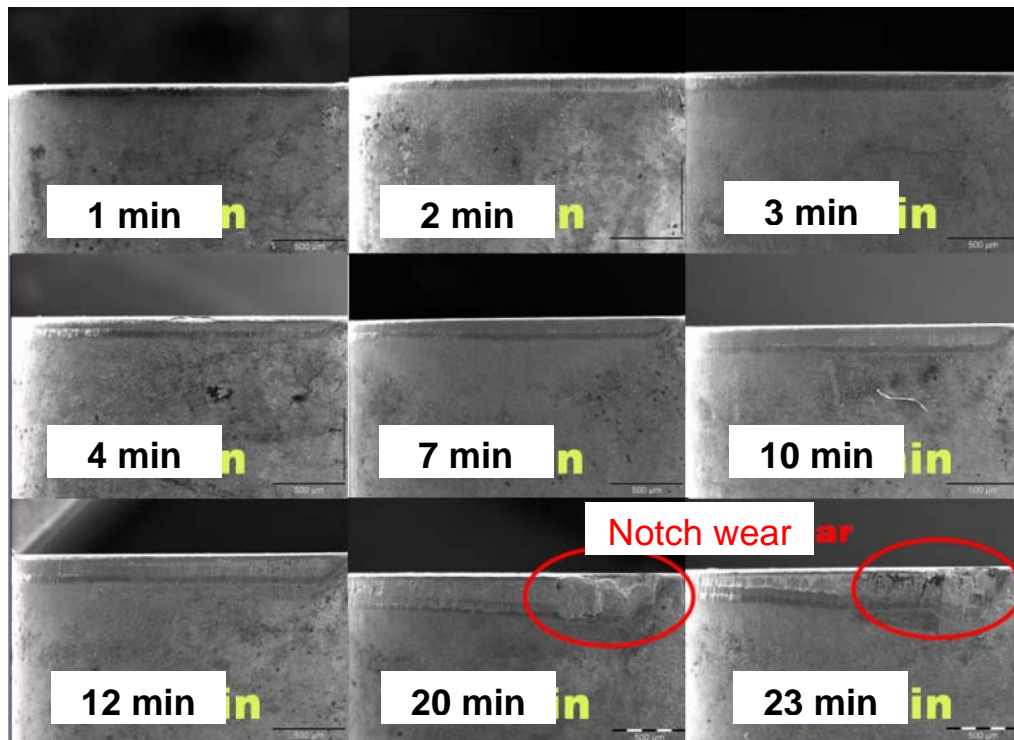
**Figure 7 Evolution of flank wear observed by SEM**
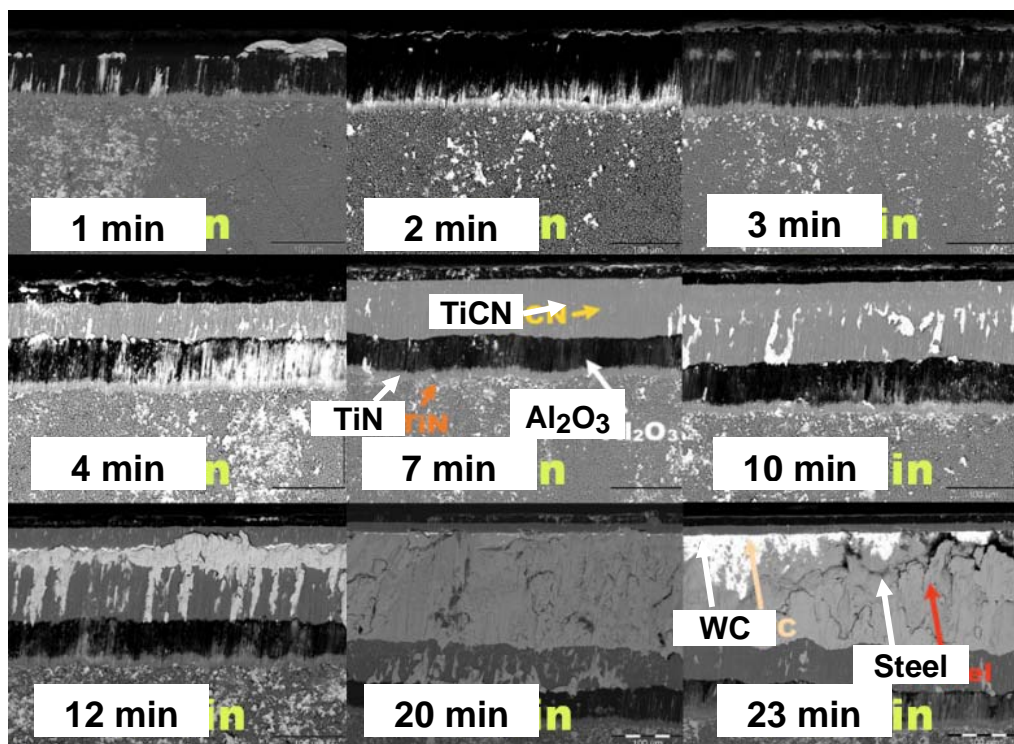


**Figure 8 BSE images on flank surface**

**2.3.1 Roughness analysis**

Figure 9 (a) shows the confocal image obtained from CLSM while Figure 9 (b) shows the approximation (A) and details (H, D and V) at the level 3 of decomposition, corresponding of Figure 9 (a), after the wavelet decomposition and reconstruction process. The decomposition level has to be determined to obtain more accurate data for surface analysis. Thus, by comparing the approximations at various levels, the maximum decomposition level was selected to be A6 since the 'approximation' surface at the level 7, A7, has been significantly distorted and the directionality of the scoring mark has been lost for details (H, V and D).

The details (H, D and V) obtained from the 2D DTW can be used to identify the small features on the flank surface associated with surface roughness, waviness as shown in Figure 10. The roughness can be regarded as high frequency components of tool surface which can be correlated with the scoring marks, while the waviness from the medium frequency, which has greater spacing than the roughness, represents irregularities from a mean line. Waviness may come from vibrations of machine tool. The form can be considered to be the low frequency components [Raja et al., 2002 and Whitehouse, 2002]. These features can be obtained by adding wavelet-decoupled details obtained at different levels of the decompositions up to the criterion (level 6) determined above [Olortegui-Yume and Kwon, 2010, and Jiang et al., 1999]. The roughness and waviness are defined as in Eqs. (7) and (8), respectively.
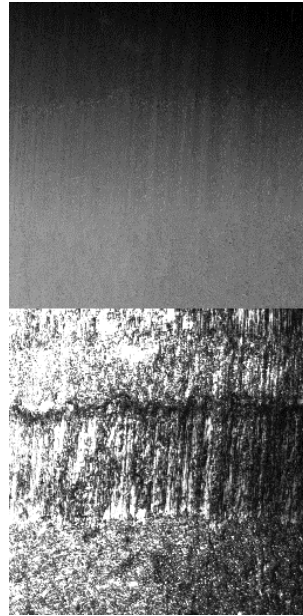
(a) CLSM Image
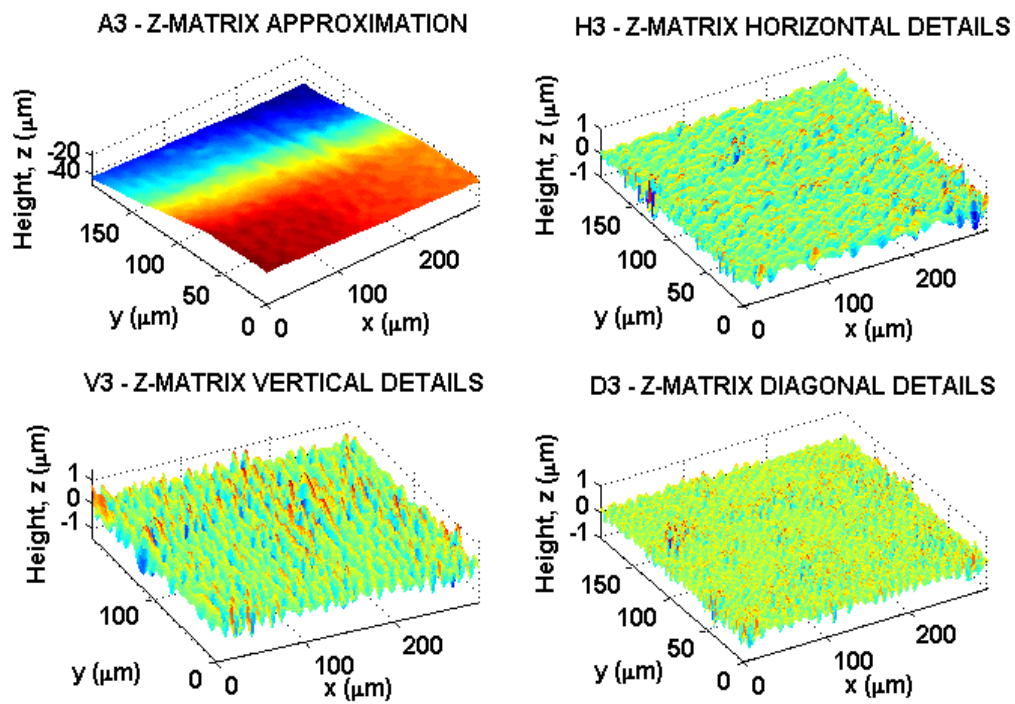


(b) Approximation (A) and Details (H, D and V)

**Figure 9 CLSM image for the flank surface at 4 min (a) and wavelet decoupled components (b) at Level 3**

29

$$\text{Roughness} = \sum_{\text{Level}=1}^{6} (H_{\text{Level}} + V_{\text{Level}} + D_{\text{Level}})$$

(7)

$$\text{Waviness} = \sum_{\text{Level}=7}^{10} (H_{\text{Level}} + V_{\text{Level}} + D_{\text{Level}})$$

(8)

The roughness image obtained by adding the details (H, D and V) up to the level 6 shows

the scoring marks on the flank wear with the directionality to the abrasion path on the wear land

as seen in Figure 10 (b). For the surface roughness statistical analysis, the root mean square ($R_q$)

of the profiles was used rather than average surface roughness ($R_a$) because with $R_a$ detailed

information is lost [Gadelmawla et al., 2002].
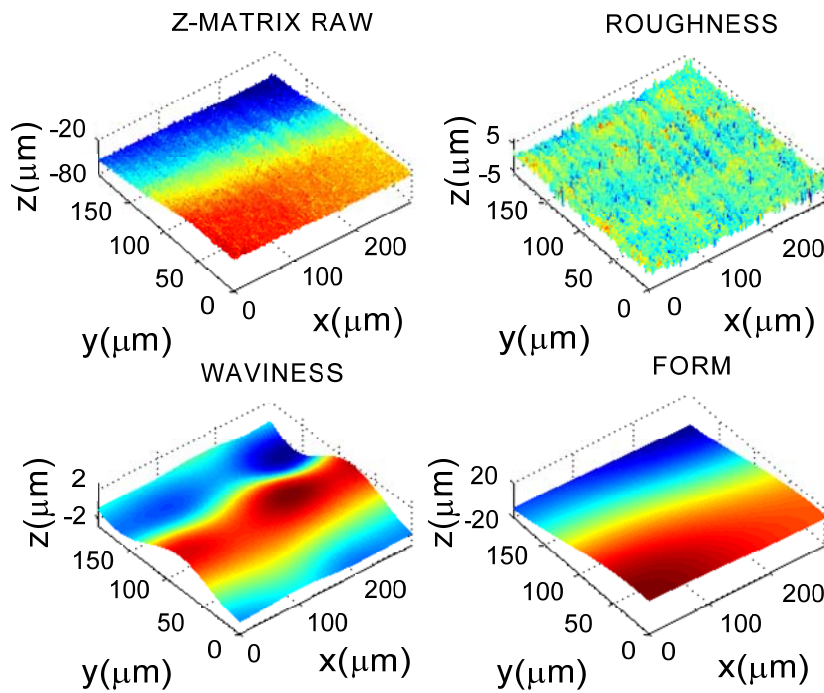


(a) Surface features on flank surface

**Figure 10 Roughness, Waviness and Form**

**Figure 10 (cont'd)**
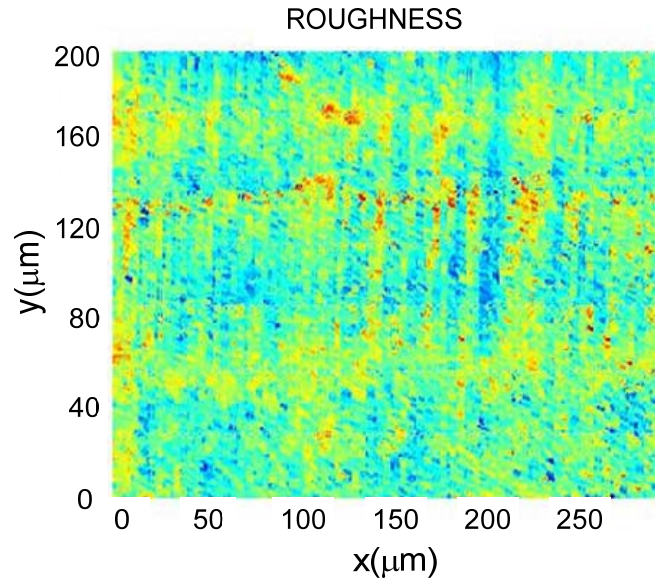


(b) Roughness

On the tool after cutting 1 min, surface roughness ($R_q$) as a function of distance from the edge was measured on $Al_2O_3$ coating at three locations indicated by three short lines in Figure11 (a). The green line on Figure 11 (a) is closest from the trailing edge or furthest away from the cutting edge. As seen in Figure 11 (b), the roughness deviation has been reduced as we assumed that larger cementite phases may be broken down or embedded into the matrix of softer ferrite. Thus, the abrasion damage becomes more uniform along the flank wear land. Furthermore, to observe the roughness change at cutting times on $Al_2O_3$ coating at the trailing edge, the roughness on $Al_2O_3$ coating was measured at cutting times up to 12 min as summarized in Table 4. The roughness value with the cutting time of 12, 20 and 23min was disregarded since the roughness data were distorted due to the adhesion on the tool surface. The items on the first column in table 4 represent each event during the wear evolution as each layer of the multi-layer

coating is exposed. Initially, the roughness increases with cutting time up to 3min at which only

$Al_2O_3$ coating was exposed but after TiCN coating was exposed (between 4 and 10 min), the

roughness at the trailing edge (on the $Al_2O_3$ coating) slightly decreased with cutting time. This

might be because the abrasive, cementite, in the work material may be 'driven' into the softer

matrix by the hard TiCN layer, while traversing across the flank land.

Figure 12 (a) and (b) present the roughness and groove size of the flank surface at the

cutting time of 7 min. The tool after cutting 7 min was chosen for this observation, as the steel

was not adhered to the tool. As was done in Figure 11, the locations, where the roughness and

groove size were measured, are presented with the short colored lines in Figure 12 (a). The

measurements at four locations are presented in Figure 12 (b) with the corresponding coating

materials. The $Al_2O_3$ coating being the softest had the largest roughness and groove size

demonstrating the consequence of abrasive wear while the TiCN coating being the hardest had

the least roughness and groove size. This trend became more obvious at 23 min as seen in Figure

13 (b). Thus, it was confirmed that the hardest coating TiCN among the multi-layer coatings has

the most significant role against abrasion wear while alumina coating has a great resistance

against thermal shock and chemical wear [Olortegui-Yume et al., 2008].
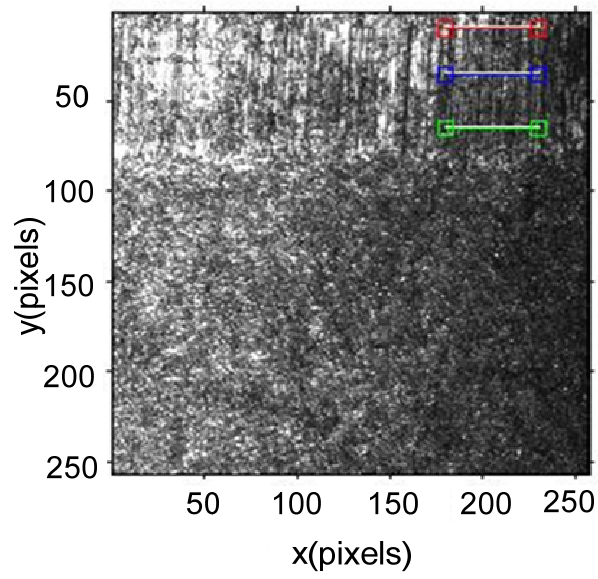
(a) Locations measured on $Al_2O_3$ coating
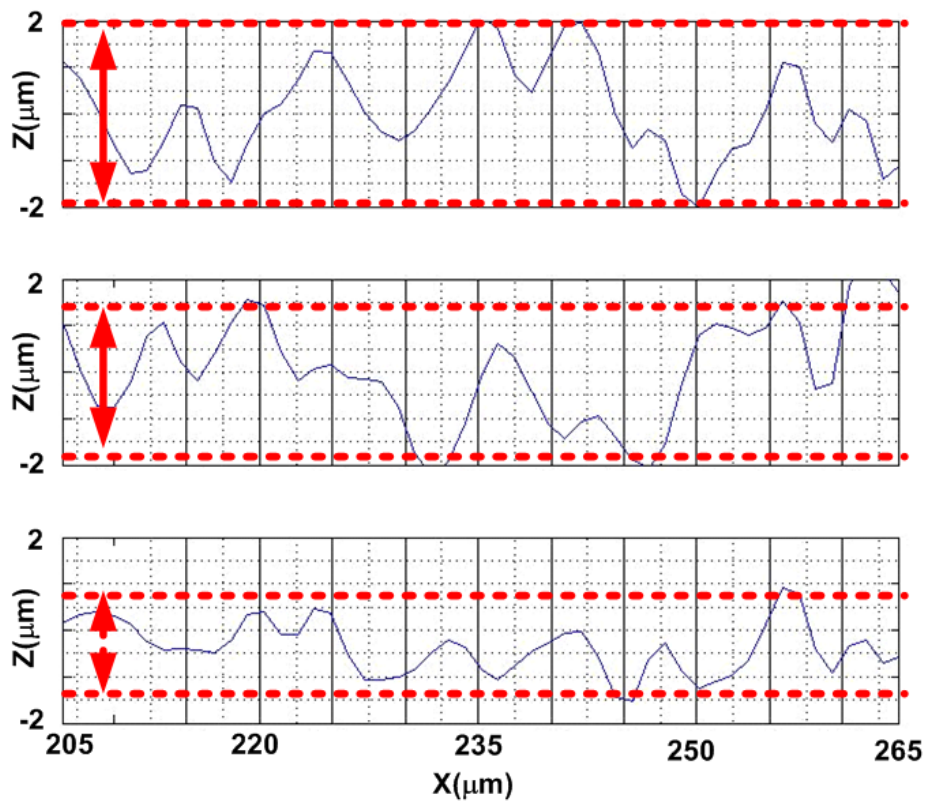


(b) Roughness at the locations in (a)

**Figure 11 Roughness Data on Tool after Cutting for 1 min**

**Table 4 Roughness data on the coatings**

| | Time (min) | $Al_2O_3$ | TiN |
|---|---|---|---|
| The exposure of $Al_2O_3$ | 1 | 0.6717 | 0.7225 |
| | 2 | 0.7707 | 0.6709 |
| | 3 | 0.9100 | 1.7413 |
| The exposure of TiCN | 4 | 0.7814 | 1.0473 |
| | 7 | 0.5299 | 0.6533 |
| | 10 | 0.4777 | 0.5480 |
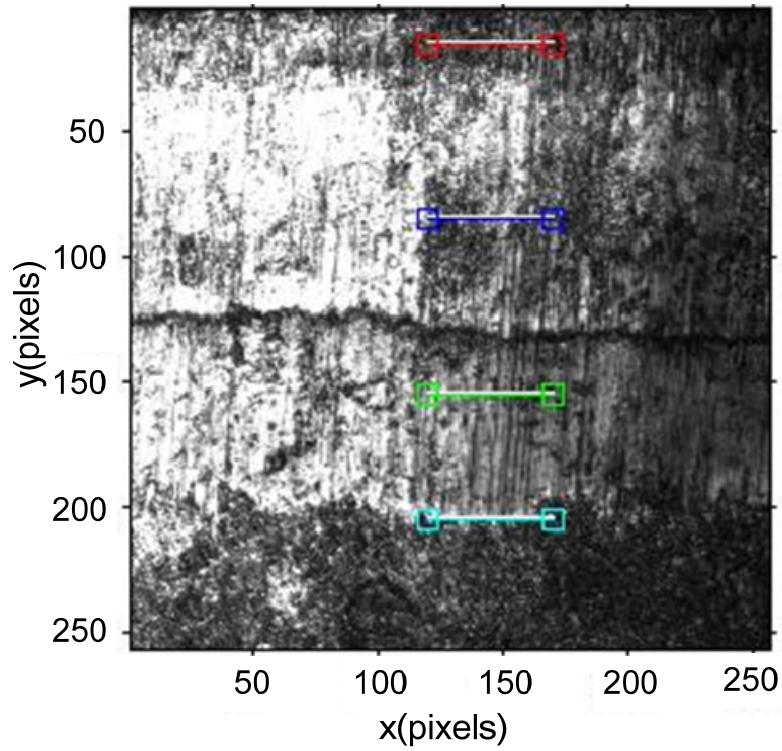


(a) Locations of roughness measured

**Figure 12 Roughness data and Groove sizes on the tool after cutting of 7 min**

**Figure 12 (cont'd)**
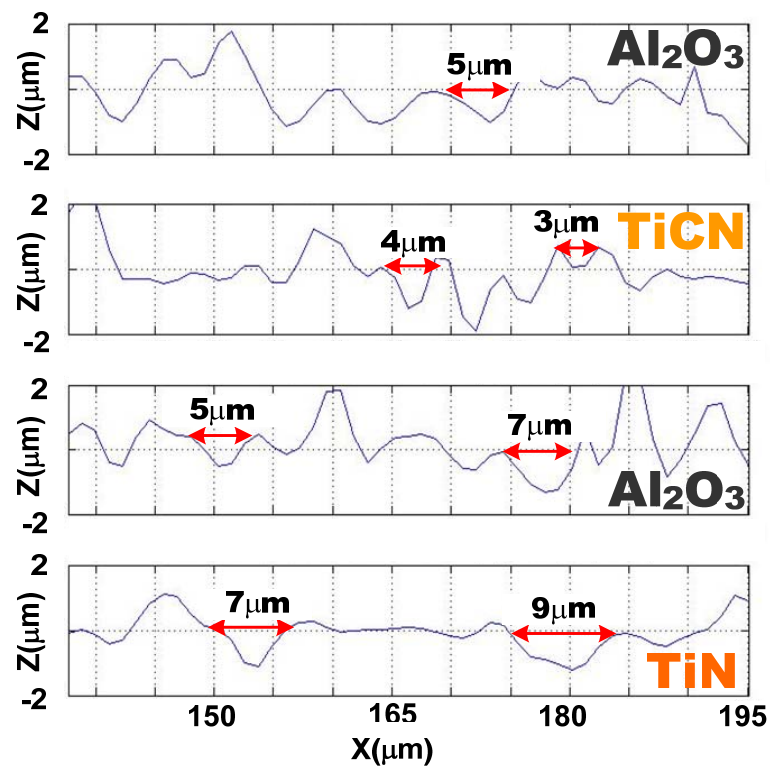
(b) Groove sizes at the locations in (a)
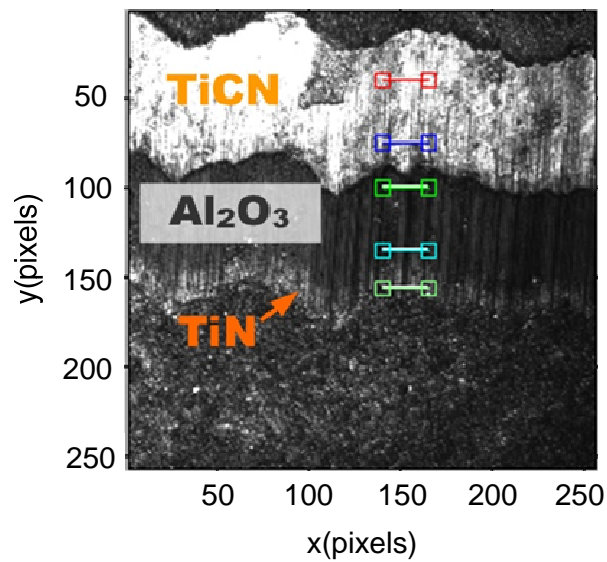


(a) Locations measured

**Figure 13 Roughness on the tool after cutting for 23 min after etching of steel**

**Figure 13 (cont'd)**
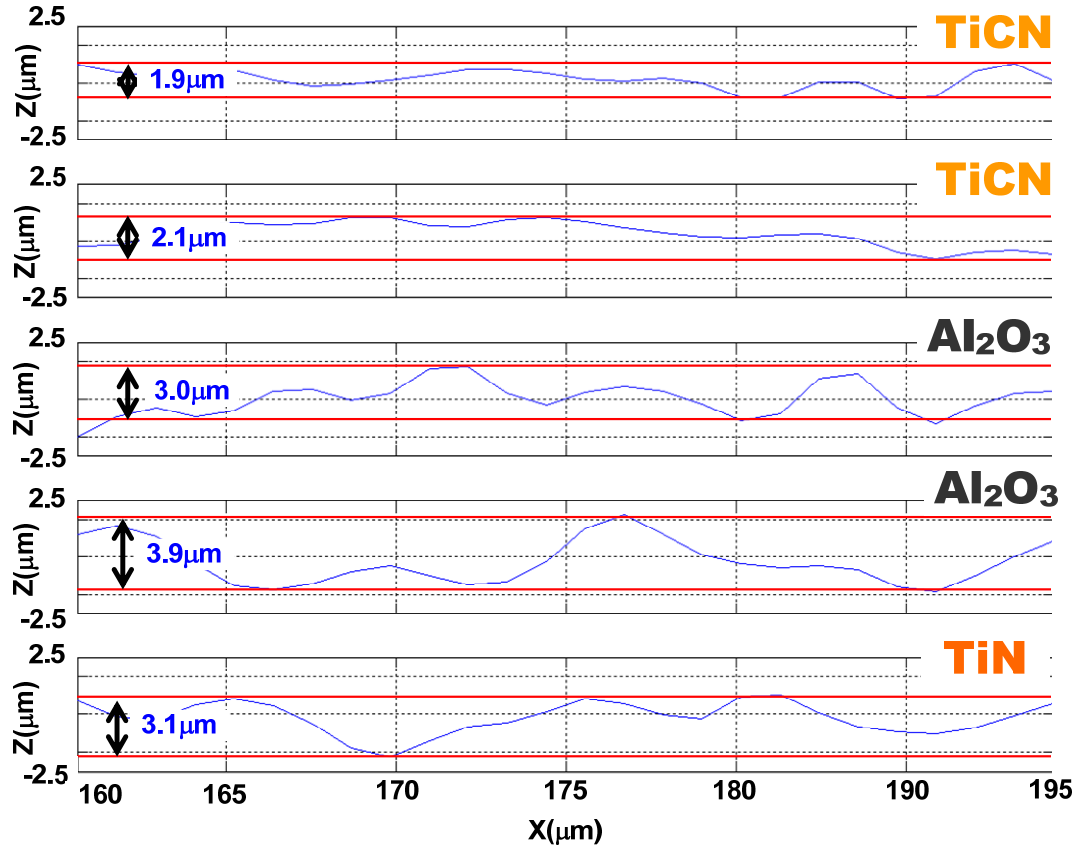


(b) Roughness at the locations in (a)

Figure 14 (a) shows the microstructure of the work material used, refined AISI 1045 steel. The groove size should be related to the size of the cementite due to the fact that abrasion wear takes place by the hard cementite phase. However, the size of each cementite in pearlite colony is too small (~0.5μm) to be matched with the size of scoring mark (3~10μm) observed. Nonetheless, if the angle of the cementite orientation in pearlitic phase to the tool surface and the size of pearlite conlony are considered, the groove size can be identified. For example, if the angle is 90º as in Figure 14 (b), very small groove size should be detected. However, the hard cementite in pearlitic phase can attack in any orientation, which can attribute to the observed

groove size. On the other hand, the size of the pearlite phase shown in Figure 14 (a) is between

20μm and 35μm. Despite of the fact that a larger size of pearlite phase observed compared to the

groove size, it should be considered that only small segments of pearlite colony might be

involved in abrading action as seen in Figure 14 (b). In addition, the groove size can be also

dependent upon the penetration depth, D. This is why groove depth observed on TiCN was

smaller than other coatings as seen in Figure 12 (b) and Figure 13 (b). Another possible scinerio

is that pearlite can be broken down to smaller pieces due to the severe shear deformation in the

cutting process so that only smaller fractured pearlites generate the scoring mark. In both cases,

the abrasive wear takes place by the pearlite grains rather than individual cementite lamella.
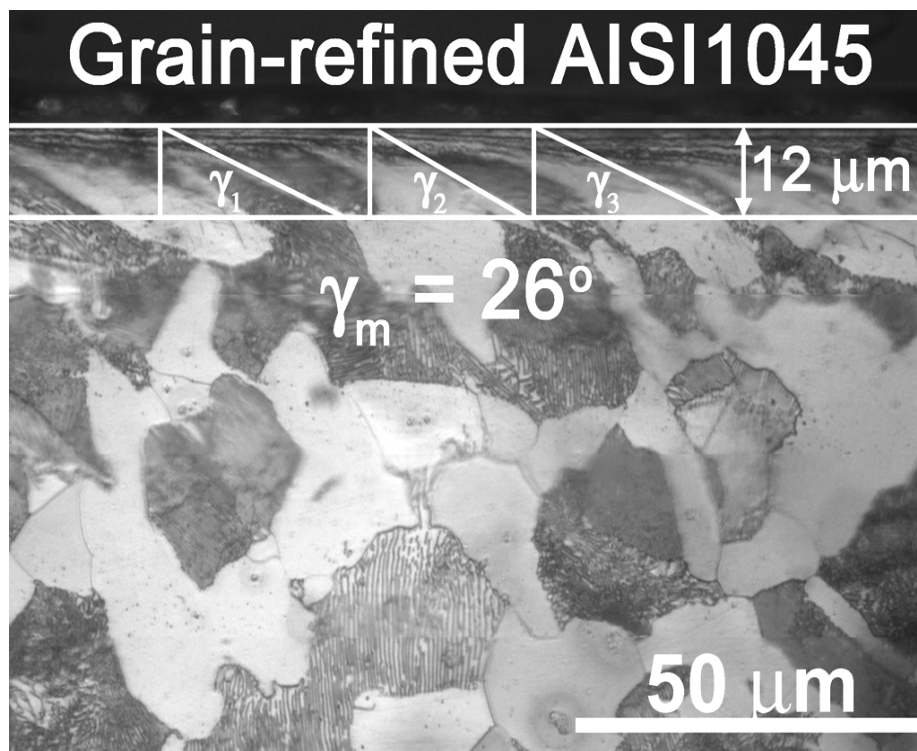


(a) Microstructure of refined AISI 1045 steel

**Figure 14 Microstructure (a) and a pearlitic colony size (b) of refined AISI 1045 steel**

**Figure 14 (cont'd)**



CEMENTITE

25μm

PEARLITE

90º

COATING

6μm

GROOVE SIZE

GROOVE SIZE

D

Θ
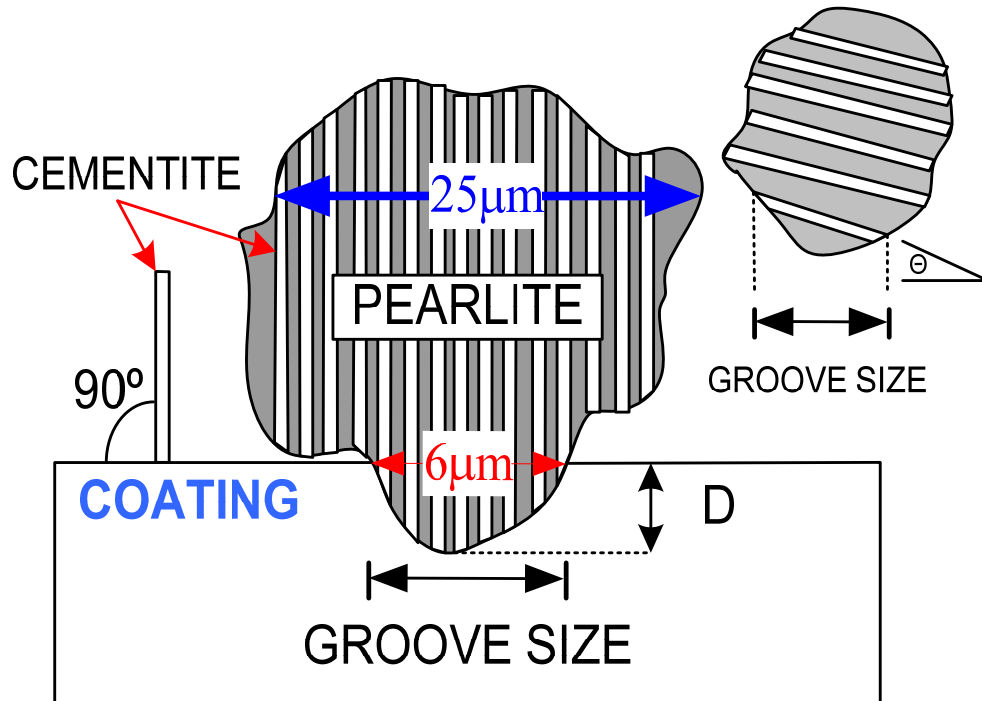
(b) Groove size by a pearlite colony

## 2.3.2 Flank wear analysis

To study the flank wear evolution, the surface profiles on the flank were extracted from the HE images obtained by CLSM using wavelet-denoising and 2D DWT process. The decomposition level 2 was selected for 2D DWT since the wavelet-filtered profile (approximation) was too smoothed after the level of 2. Figure 15 shows both 3D and 2D cross-sectional profiles of the flank wear for the raw image and the wavelet filtered image (A2) at the decomposition level 2. The cross-sectional profiles at the cutting times were collected and finally merged on to the mask of the coating materials in order to analyze the flank wear evolution as presented in Figure 16. Up to 3 min., TiN and $Al_2O_3$ coatings were worn down quickly and no TiCN coating layer was exposed. However, after cutting 4 min., TiCN layer was exposed and

stayed exposed until the cutting time of 12 min. It indicates that TiCN did not wear at such high rates between 4 min and 12 min. due to its high hot hardness. Subsequently, the carbide was substantially worn down at 23 min due to the fact that the carbide substrate has a lower wear resistance associated with the lower hot hardness compared to the coating materials. This is easily depicted in Figure 15. Interestingly, the flank wear rate slightly decreased from 12 min to 23 min while the tool got close to the tool failure as in Figure 16 (b). Actually, the cutting experiments had to be repeated few times due to the catastrophic fracture of the cutting tool right before the cutting time reached 23 min. However, as shown in Figure 16 (c), the volume wear rate, indeed, significantly increased after the cutting time of 12 min. It means that once the carbide is exposed, the wear front will attack mostly the softer carbide without extending the flank wear land. Thus, the standard flank wear, $V_B$, does not adequately describe the state of tool wear and the wear volume and profiles may be considered for the flank wear analysis.

The accelerated wear rate of the carbide comes also from the adhesion. Figure 17 (a) shows the steel adhesion on the carbide at cutting time of 23 min. Once the carbide substrate was exposed, the steel adhesion can take place due to the excellent affinity between steel and carbide. The adhered steel was pulled out the carbide grain when the steel detached from the carbide substrate. To identify the amount of adhesion, the cutting insert was etched ultrasonically with hydrochloric acid for 20 min. and compared the surface profiles before and after etching at 23 min. Finally, it was found that the adhesion thickness was around 20μm as shown in Figure 16 (a). In addition, the deterioration of TiCN coating due to the accelerated wear of carbide substrate was observed in Figure 17 (b). On the other hand, it is commonly believed that multilayer coating can enhance the resistance of coatings against crack propagation [Cselle and

Barimani, 1995 and Paskvale, 2007]. However, the argument does not agree with our experimental data as shown in Figure 16 (a).
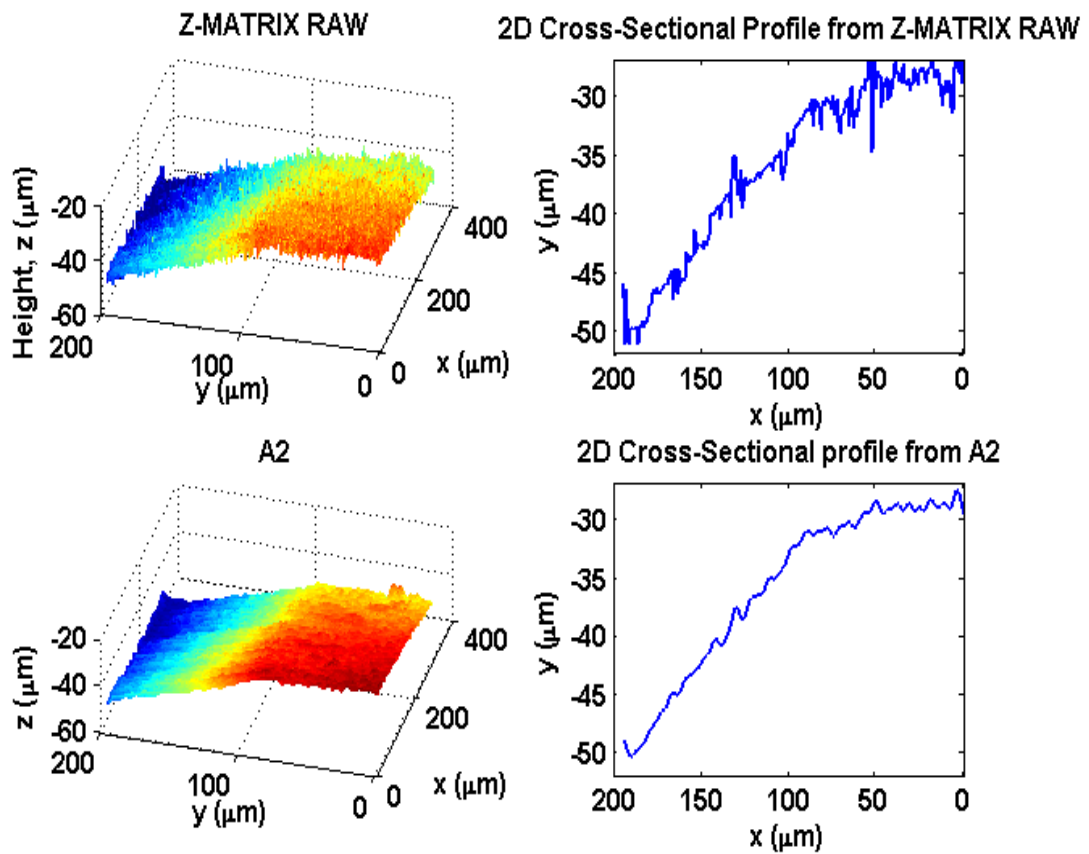


**Figure 15 3D and cross-sectional profiles of raw data and wavelet-filtered at level 2**
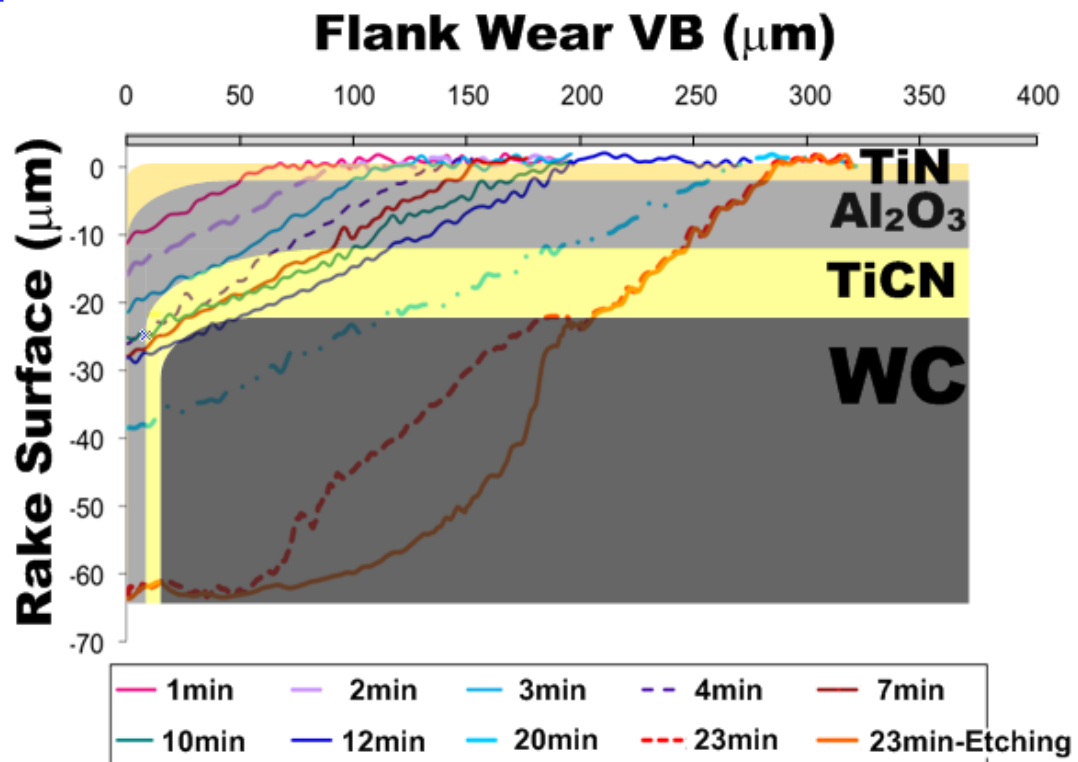
(a) 2D Flank wear profiles at cutting times
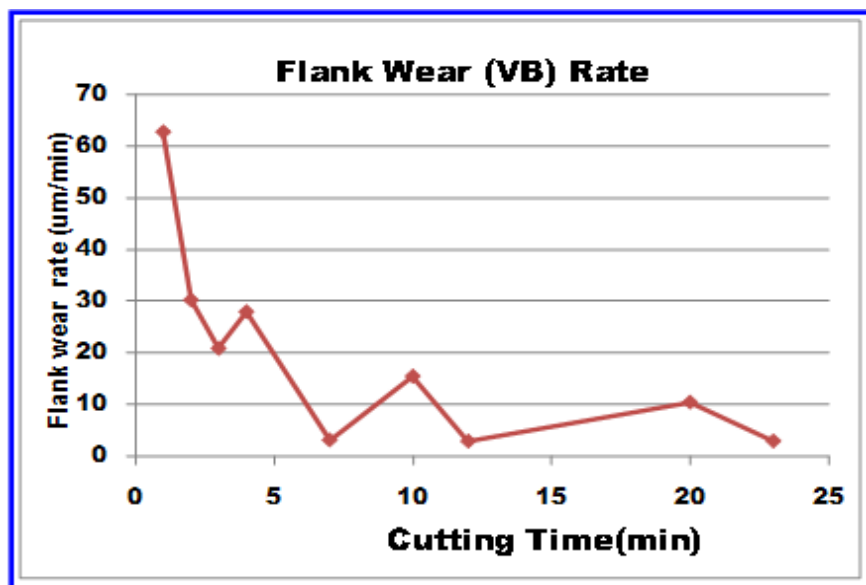


(b) Flank ($V_B$) wear rates

**Figure 16 Flank wear profiles and wear rates**

**Figure 16 (cont'd)**
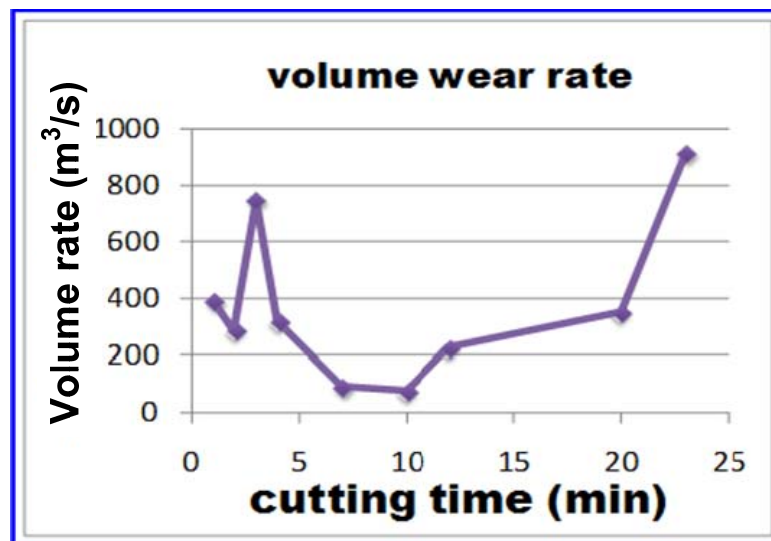


(c) Volume wear rates
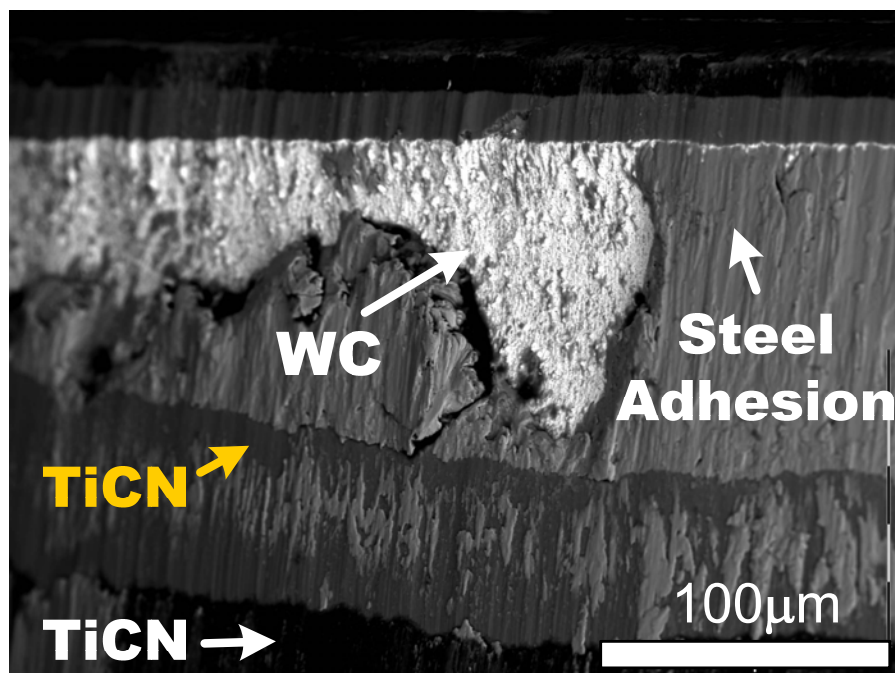


(a) Steel adhesion on the carbide

**Figure 17 Adhesion on the carbide and coating delamination at cutting time of 23 min**
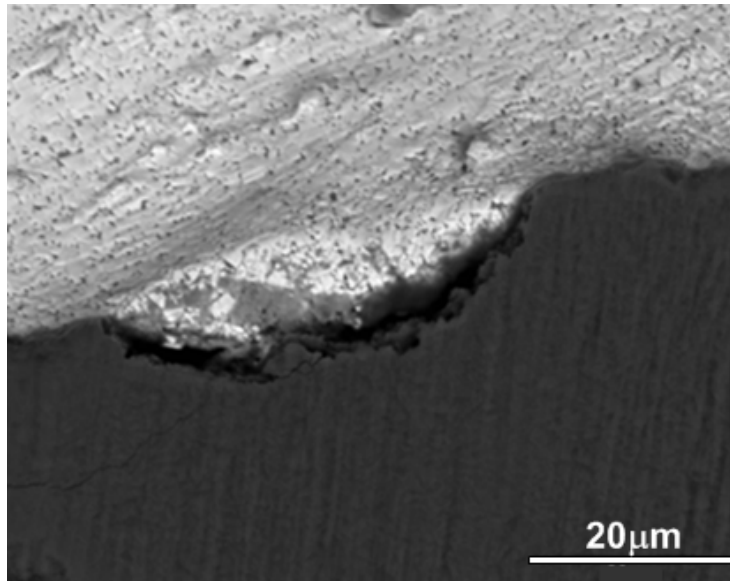
(b) Coating delamination

Figure 18 presents the notch wear on the tool at depth of cut line (DCL) at cutting time of 20 min. and 23 min. The chip material suffers the severe shear deformations and the lateral extension of the chip at DCL was reported [Chandrasekaran and Johansson, 1994]. The possible notch wear mechanism was proposed as the chip at the DCL region with relatively high micro hardness can plough or adhere to the tool surface depending upon the affinity between the materials. In our cutting test, notch wear become significant between 20 and 23 min. at which carbide was exposed. Thus, the 'extended chip' abrades the tool surface until carbide was exposed and the adhesion wear takes over as soon as the carbide was exposed. Note that the notch wear was not detectable up to 12 min. due to the high wear resistance of the ceramic coatings against the abrasion. The intermittent and repeating process of the adhesion/abrasion between carbide and work material produces the severe notch wear, which eventually contributes to the catastrophic tool failure around 23 min. Notch wear can be observed more clearly after

etching away the steel as seen in Figure 19 (a) and the size of scoring mark on the alumina coating in notch wear zone is much bigger than that in the uniform flank wear zone as in Figure 19 (b). This is because the blunt edge at notch region cannot cut the pearlite colony sharply so the size of pearlite becomes bigger and pearlite surface gets rougher so that the roughness on the coating became much larger at notch wear zone.
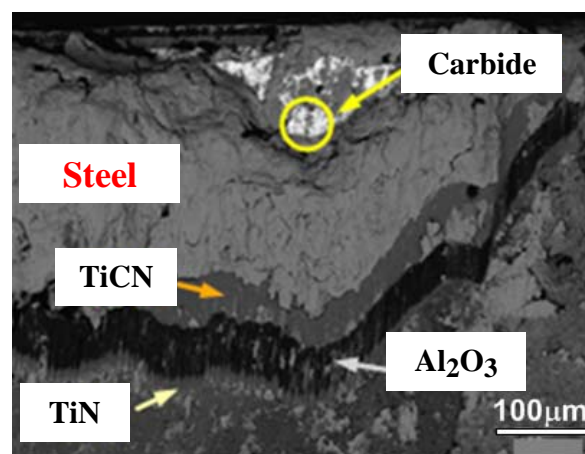


(a) At 20 min
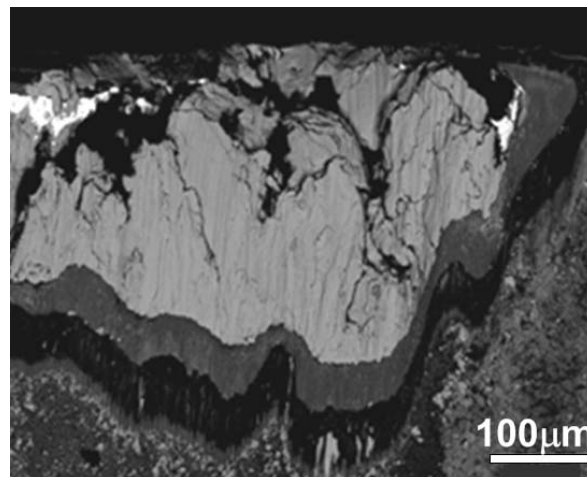


(b) At 23 min

**Figure 18 Notch wear on the tools after 20 and 23 min of cutting**
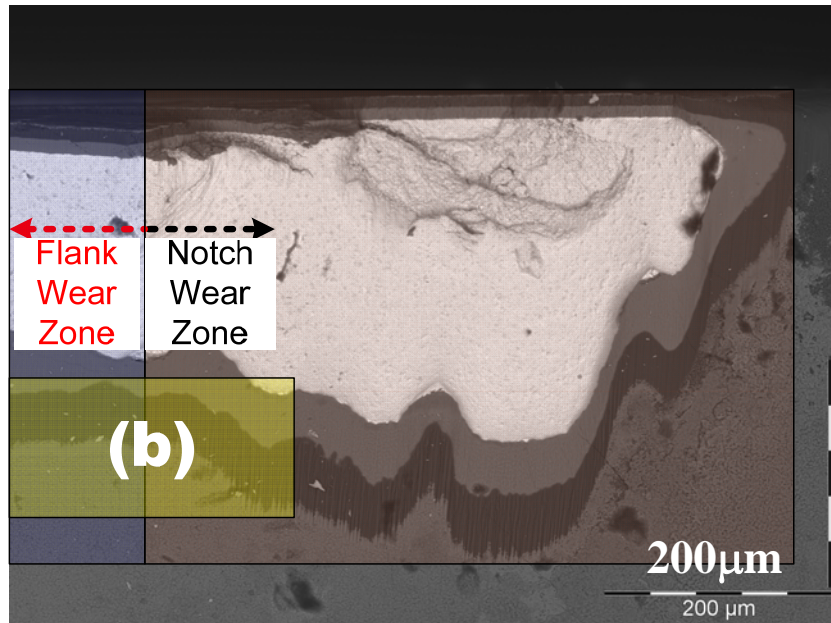
(a) After etching of Figure 18 (b)
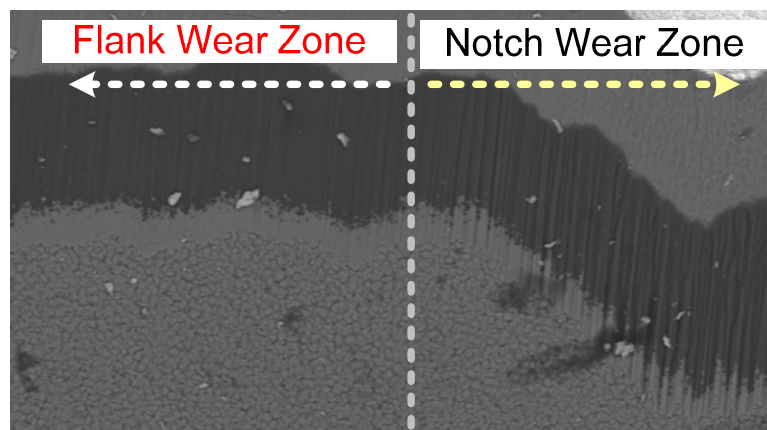


(b) Scoring marks on alumina coating at 23 min in (a)

**Figure 19 Notch wear after etching (a) and scoring marks and notch wear zone (b)**

The temperature distributions from FEM simulations at the flank surface were obtained as a function of the flank wear land as shown in Figure 20. The temperature change due to the flank wear shows the continuously decreasing trend with the flank wear land up to 70μm. However, the temperature profiles start to have parabolic shapes after the flank wear land ($V_B$)

reaches 120μm. At that point, the maximum temperature occurs at the trailing edge of the flank wear land. Until then, the temperature decreases along the flank surface. However, as the flank wear land increases further, the temperature increases again near the trailing edge and reaches the local maximum. At the same time, the result of the FEM simulation shows that the cutting temperature also slightly decreases as the flank wear land ($V_B$) increases as seen in Figure 20.

This can be explained by the 2-body abrasion model in which the wear rate increases with temperature. In addition, the phase transformation of the work material due to the high interface temperature and pressure, may be affecting the wear evolution [Kwon, 2000]. However, the volume wear rate increases once the carbide is exposed after 12min in Figure 16 (a). This is possibly because adhesive wear might be gaining its momentum over abrasive wear.
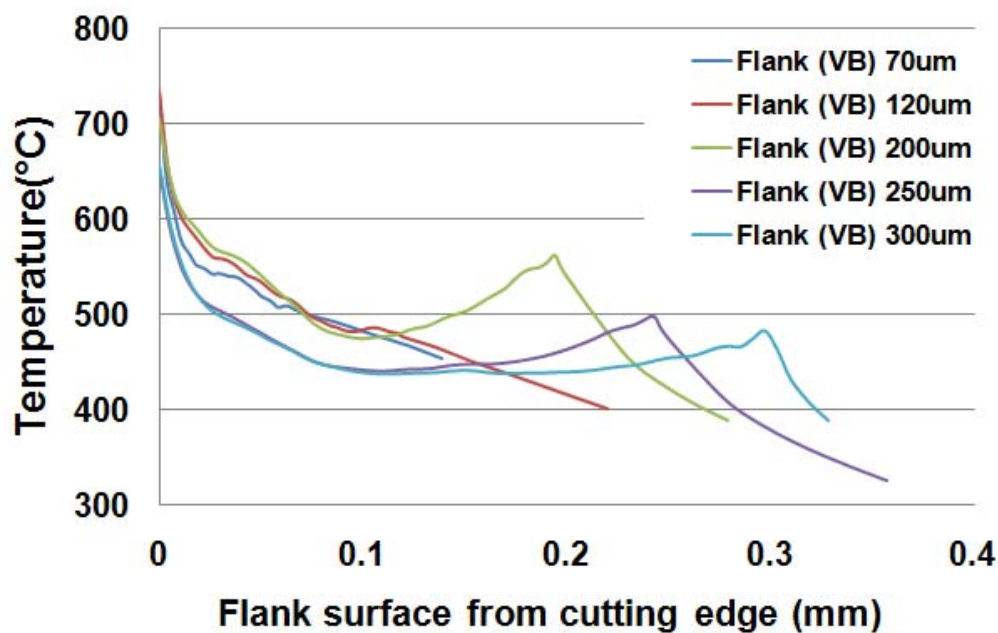


**Figure 20 Temperature profiles on cutting tools from FEM simulations**

From the experiment measurements and FEM simulation results, the wear calibration

constants were determined and temperature profiles on the cutting surface were obtained

respectively. The temperature profiles and the wear constants were used for the 2-body abrasive

prediction model presented in Eq. (1) programmed by MATLAB software. The predicted flank

wear profiles are shown in Figure 21. Comparing to Figure 16 (a), the 2-body abrasive model

with hot hardness data of the coating materials predicted quite well, as the assumption that 2-

body abrasion wear takes place when the pearlitic steel is used because of the constrained

microstructure of cementite phase in the form of peralite [Wong et al., 2004]. Again, based on

the predicted results, the wear progress on TiCN coating, that is between 7 and 12 min, was so

small due to its high hot hardness, which agrees well with the experiment results.
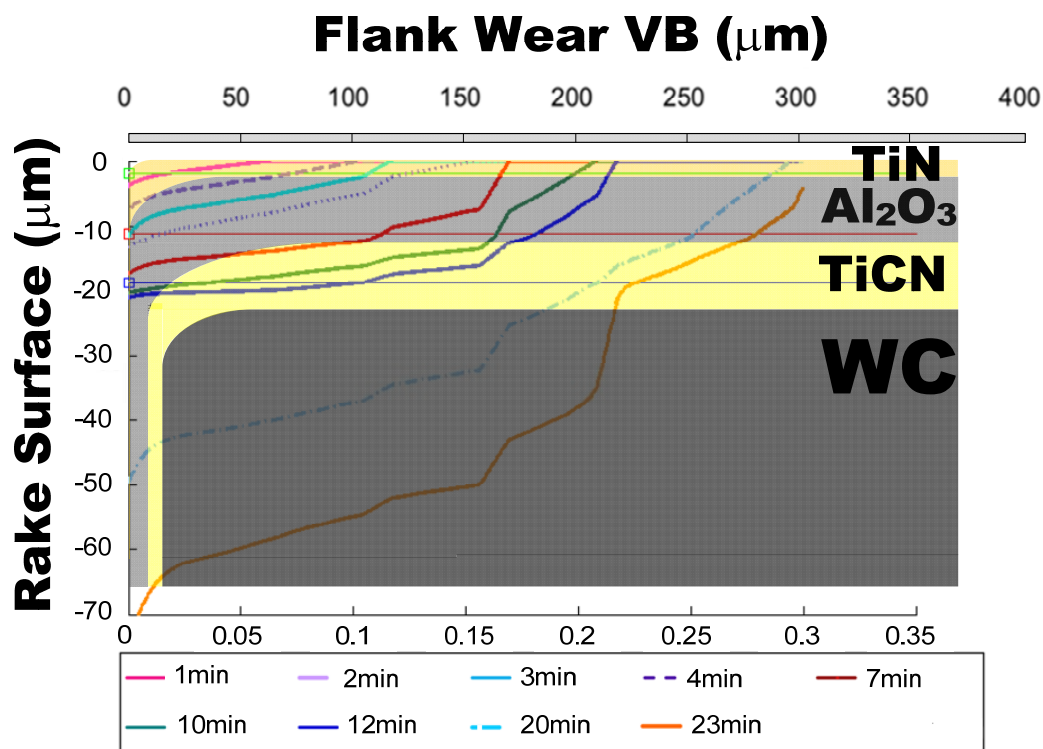


**Figure 21 Predicted flank wear based on 2-body wear model**

**2.4 CONCLUSION**

The following conclusions can be drawn:

● The combination of CLSM and 2D wavelet transformation techniques is useful in obtaining the flank wear profiles and the surface features such as groove size and roughness on the tool, which can be used to study the cause and evolution of flank wear.

● Finite element simulation is able to provide the interfacial cutting temperature, which are needed to predict the flank wear profiles. The interfacial pressure was assumed constant as the FE simulation cannot maintain the intimate contact.

● TiCN coating shows high wear resistance against the abrasion while the carbide has the least resistance in wear. After carbide was exposed, the work material adhered to the carbide substrate and the cutting tools were fractured due to the crater degradation on the carbide surface. Because of the larger grains in carbide, the wear mechanism can be quite different as the carbide grains can pull out.

● Notch wear becomes significant at 20 and 23 min by the intermittent repeated process of adhesion/abrasion. This may come from the stick-slip interfacial condition. The size of the scoring mark on the $Al_2O_3$ coating at notch wear zone is much bigger than that at uniform flank wear zone.

● The groove size was measured and showed that the softer coating is damaged much more. As soon as the hard TiCN coating is exposed, the abrasive cementite cannot affectively abrade the hard surface.

- The correlation between groove size and pearlite grain size was investigated. Only a small segment of the pearlite colony and/or fractured pearlite may abrade the tool surface producing the scoring marks.

- Unlikely for the crater wear in which the complex wear mechanism is involved, for the flank wear the multilayer coating did not show much beneficial effect and only hard coating that has high hot hardness is required.

- 2-body abrasive model in conjunction with FEM simulation results shows very good prediction of flank wear.

Chapter 3

**TOOL WEAR ANALYSIS ON MULTI-LAYERED COATED CARBIDE TOOLS IN FACE MILLING**

Recent coating technology has advanced to extend the life of carbide tools effectively in metal cutting process. In general, the coating can be deposited onto the carbide tools in a single-layer or multi-layer scheme processed by CVD and/or PVD methods. The coating materials along with the coating process must be determined depending on the machining process and the work material. Each coating process has its advantages and disadvantages. For example, CVD-$Al_2O_3$ coating provides a thermal barrier and good bonding with other coatings. However, the brittle eta phase can be formed at the coating interface at high deposition temperature, which reduces the transverse rupture strength (TRS) of the substrate and weakens the cutting edge [Stephenson and Agapiou, 2006]. On the other hand, the PVD coating process produces the sharp cutting edge and free thermal cracks on the cutting surface [Sodergberg et al., 2001]. The performances of PVD and CVD coated carbide tools were investigated in many recent works [Jawaid et al., 2000 and Dobrzanski et al., 2006]. Jawaid et al., [2000] found that the CVD coating tool was superior to the PVD coating tool due to high adhesion strength of the CVD coating tool despite of inherent disadvantage from the CVD coating process. Dobranski et al., [2006] compared CVD and PVD in nitride tool ceramics on a 'pin-on-disk' method and concluded that the multilayer coating, processed by CVD, was better due to the adhesion strength.

Several tool wear mechanisms have been reported in metal cutting processes [Stephenson and Agapiou, 2006, Melo et al., 2006, Olortegui-Yume and Kwon, 2007(1) and Gu et al., 1999]. Abrasive wear dominates the wear process when the hard inclusions in work material abrade the

tool surface. Thus, the abrasive wear strongly depends on the hardness of tool materials. In addition, adhesive wear can occur when a high affinity of work material to a particular tool material exists. At low cutting speeds, build up edge (BUE) can be formed and detached. During the detachment of BUE, small volumes of tool material can be separated away. When the cutting temperature is high as in continuous turning, diffusion or dissolution wear is dominant at the rake surface [Olortegui-Yume and Kwon, 2007(1)]. In milling, in addition to abrasive wear, thermo-mechanical fatigue wear and crack can take place mainly due to the nature of the interrupted process, which generates the thermo-mechanical cycles.

In general, the multi-layer coated tools are known to deter tool wear of carbide tools [Olortegui-Yume and Kwon, 2007(2), Olortegui-Yume et al., 2008, Cselle and Barimani, 1995]. However the reason for the wear deterrence is not well established. In the case of turning AISI 1045 steel with multilayer (TiN/Al$_2$O$_3$/TiCN) coated carbide tools, the reason for extending tool life becomes clear recently [Olortegui-Yume and Kwon, 2007(2), Olortegui-Yume et al., 2008]. At the rake, crater wear occurs in combination of abrasive and dissolution wear mechanisms. At high cutting speed, the continuous turning process increases the interfacial temperature high enough to activate dissolution wear. At the flank, abrasive wear is the main dominant wear mechanism. The success of the multilayer coated tools comes from the fact that the Al$_2$O$_3$ coating shows outstanding resistant to dissolution wear which is the important wear mechanism for crater wear especially at high cutting temperature. On the other hand, hard coating, TiCN, exhibits excellent performance against the abrasive wear while TiN coating provides low friction at the cutting interface. Therefore, the multilayer scheme works because the tribological condition at the interface changes as each coating exposes during machining. With the change in the tribological condition, the location of maximum cutting temperature changes, which in turn

51

changes the location of maximum crater depth. Thus, the multilayer scheme extends the tool life by changing the maximum wear locations as each layer is exposed [Olortegui-Yume et al., 2008].

On the contrary, it is commonly believed that the effectiveness of multilayer coating comes from the delay in the crack propagation [Sadik and Myrtveit, 2009] because the crack can propagate along the coating interfaces instead of right through the coatings into the substrate. Under the cyclic loading in milling process, enhanced toughness and wear resistance against thermal and mechanical impact are required; and, again, multilayer coating has been cited to improve the life of cutting tools [Cselle and Barimani, 1995].

This chapter reexamined these issues by analyzing the tool wear evolution of multi-layer coated inserts. Wear surface profiles was obtained using the combined technique of confocal laser scanning microscopy (CLSM) and wavelet transform as presented in [Olortegui-Yume and Kwon, 2010]. The 3D surface profiles as a function of cutting times were obtained to observe the flank wear evolution of the multi-layer coated inserts after face milling. Two multi-layered coated inserts processed by CVD and PVD respectively were evaluated in terms of flank wear ($V_B$) and edge chipping as well as adhesion test.

## 3.1 EXPERIMENTAL SETUP

Face milling tests were performed without any lubrication on an AISI 1045 steel block (8"X5"X6") with the coated carbide inserts (SEEW 42 A7A) provided by Valenite Inc. (Madison Heights, Michigan). The square type inserts were coated by two different types of coating processes, CVD for triple layer (TiN/ $Al_2O_3$/TiCN) and PVD for double layer (TiN/TiAlN). Only one insert was used in a three-flute tool holder for the experiment to reduce variables in tool wear. Figure 22 shows the face milling setup. The face milling started at one corner of the steel and completed one path. After cutting 5 paths, one layer was completely removed. The cutting was performed up to the 8$^{th}$ layer unless edge chipping occurred. The flank wear was observed with CLSM after each layer has been removed. The cutting conditions are summarized in Table 5.

An indentation test was also performed using a Wilson Rockwell Hardness Tester in order to evaluate the adhesion quality of the double and triple layer coatings deposited on to the carbide. Maximum applied force and maximum radius of indentation were set at 1472N and 0.2mm respectively.
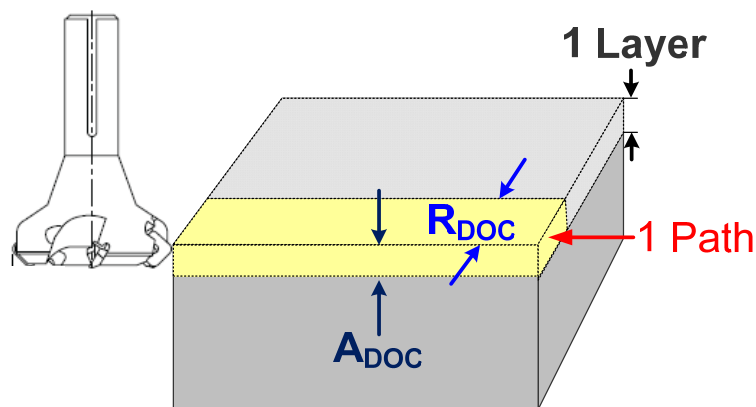


**Figure 22 Schematic of the face milling**

**Table 5 Cutting conditions**

|  | Cutting Conditions |
| --- | --- |
| Work material | AISI 1045 |
| Cutting speed (m/min) | 200, 300 & 400 |
| Feed rate (mm/min) | 0.15 |
| Axial DOC, $A_{DOC}$, (mm) | 0.5, 1 & 2 |
| Radial DOC, $R_{DOC}$, (mm) | 26.1 |

## 3.2 TOOL WEAR MEASUREMENT

For CLSM, a Zeiss LSM210 was used for flank wear width ($V_B$) measurement and 3D

flank wear profiles. Additionally, a scanning electron microscope (SEM) (JEOL JSM-6400) for

backscattered electron image (BSE) and an energy dispersive X-ray Spectroscopy image (EDS)

was also utilized for the observation of the extent of the adhesion. Figure 23 illustrates the

CLSM images of flank wear land ($V_B$) with an objective of 20X for measurement. In addition, to

characterize the flank wear evolution on the insert after removing each layer, height encoded

(HE) images were obtained from the CLSM with an objective of 50X as shown in Figure 24.

Ultimately, these HE images were converted into 3D surface profiles using an image processing

technique including wavelet transform, which are represented in Figure 25. For example, once

the HE image in Figure 24 (a) is obtained by the CLSM, wavelet de-noising with the mother

wavelet, Daubechies20 ('db20'), is performed using Matlab software to eliminate the noise and

spikes in a HE raw image. And then the 2D wavelet transform is applied in order to obtain the

tool wear profiles by decoupling the small features on the surface such as roughness. The 2D-

wavelet analysis decouples the raw 3D data to 4 sets of wavelets coefficients, called

approximation, horizontal details, diagonal details and vertical details at levels. The 3D data can

be transformed up to the level where the surface profiles maintain the original shape without distortion. Then inverse wavelet transform for these coefficients are required to obtain an approximation, horizontal, diagonal and vertical details. The approximation can be used as the tool wear profile while the details can be considered as surface roughness. The decomposition level has to be determined to obtain more accurate data for surface analysis. Thus, by comparing the approximations at various levels, the maximum decomposition level can be selected. In this study, the approximations at zero level are used to obtain the tool wear profiles at cutting distances (layers). The detailed information for the image processing technique and wavelet transform can be found in [Olortegui-Yume and Kwon, 2010 and Park and Kwon, 2009]. On the other hand, EDS images of the worn tool were obtained to map the elements on the tool and observe the wear progress of coating, as shown in Figure 26.



(a) After 5th layer cutting      (b) After 8th layer cutting
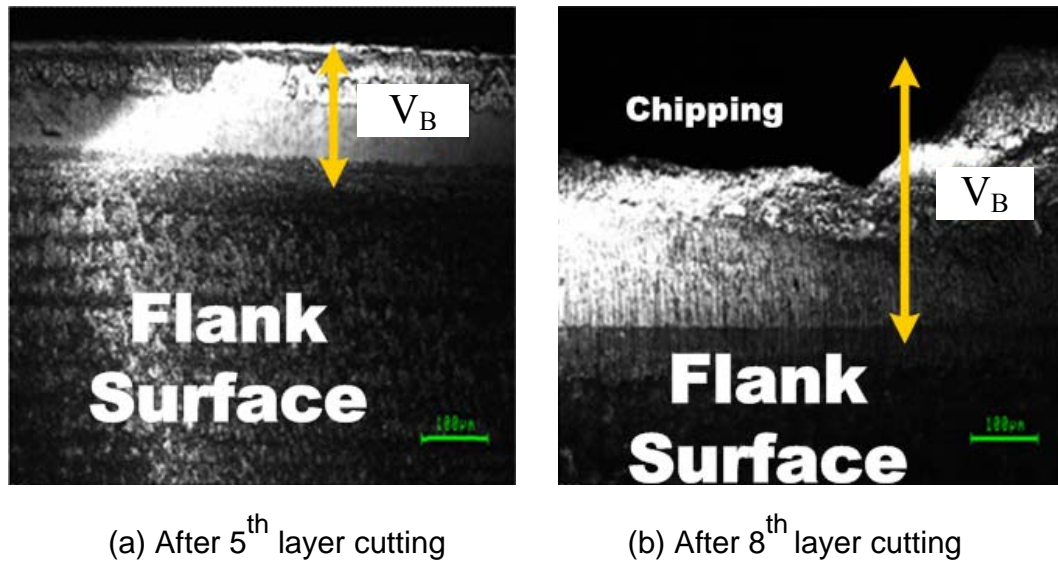
**Figure 23 CLSM images for flank wear land ($V_B$)**
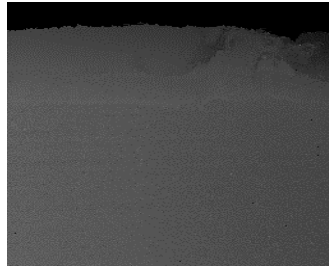
**Figure 24 HE image of flank wear after 5<sup>th</sup> layer cutting**
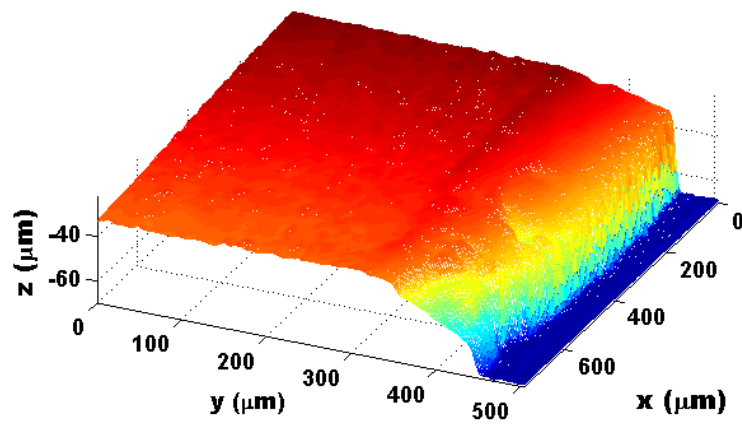


**Figure 25 3D surface profile from HE image after 5<sup>th</sup> layer cutting**
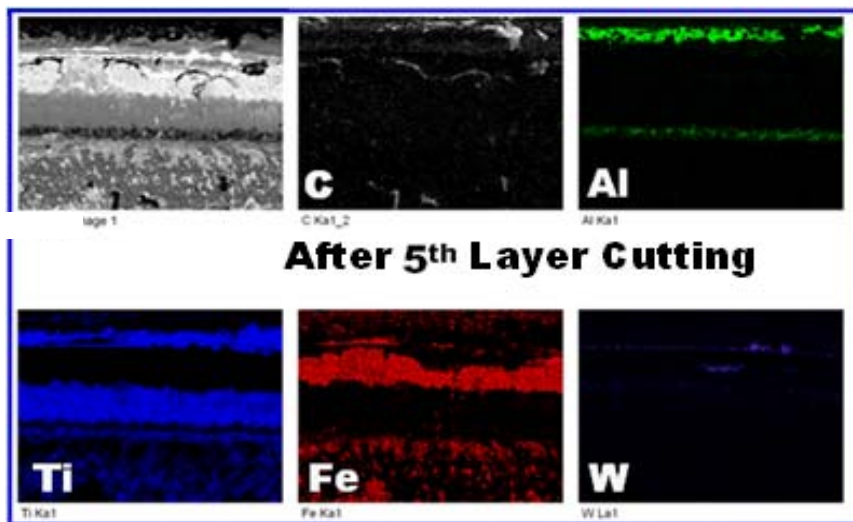


(a) After 5<sup>th</sup> layer cutting

**Figure 26 EDS images of flank wear**

56

**Figure 26 (cont'd)**
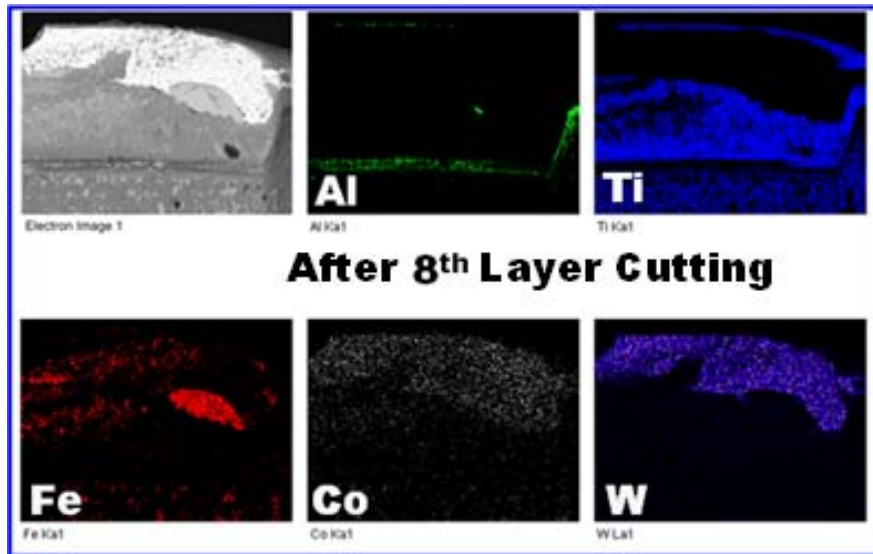


(b) After 8<sup>th</sup> layer cutting

## 3.3 FLANK WEAR ANALYSIS

The flank wear land ($V_B$) was uniformly distributed throughout the cutting edge until the chipping occurs at the cutting edge. And no significant crater wear was observed regardless of the cutting conditions. As shown in Figure 26, steel adhesion was observed on carbide substrate. Figure 27 represents the flank wear land ($V_B$) for triple layer coating at various cutting conditions. It was observed that the higher cutting speed caused the more flank wear coating carbide, as expected.

The effect of depth of cut (DOC) was minimal for the cutting speeds of 200m/min and 300m/min. The considerable difference of the flank wear land ($V_B$) for the 3<sup>rd</sup> layer cutting at 300m/min was observed but that is mainly because catastrophic edge chipping occurred. It was also found that at high cutting speed, the edge chipping was the main tool failure mode.

Especially, at the cutting speed of 400m/min, the tool was fractured only after the 1$^{st}$ layer cutting. While the abrasive wear was a dominant tool wear mechanism, the adhesion was also observed after the carbide layer was exposed. Once the carbide substrate has been exposed, the wear rate became significant due to the relatively low hardness of the carbide and the edge chipping during the removal of the adhesion layer. For comparison the flank wear of double layer coating was also measured at DOC of 0.5mm at various cutting speeds as seen in Figure 28. Similar to the case of the triple layer coating, the higher cutting speed reduced the tool life of the double layered tools.
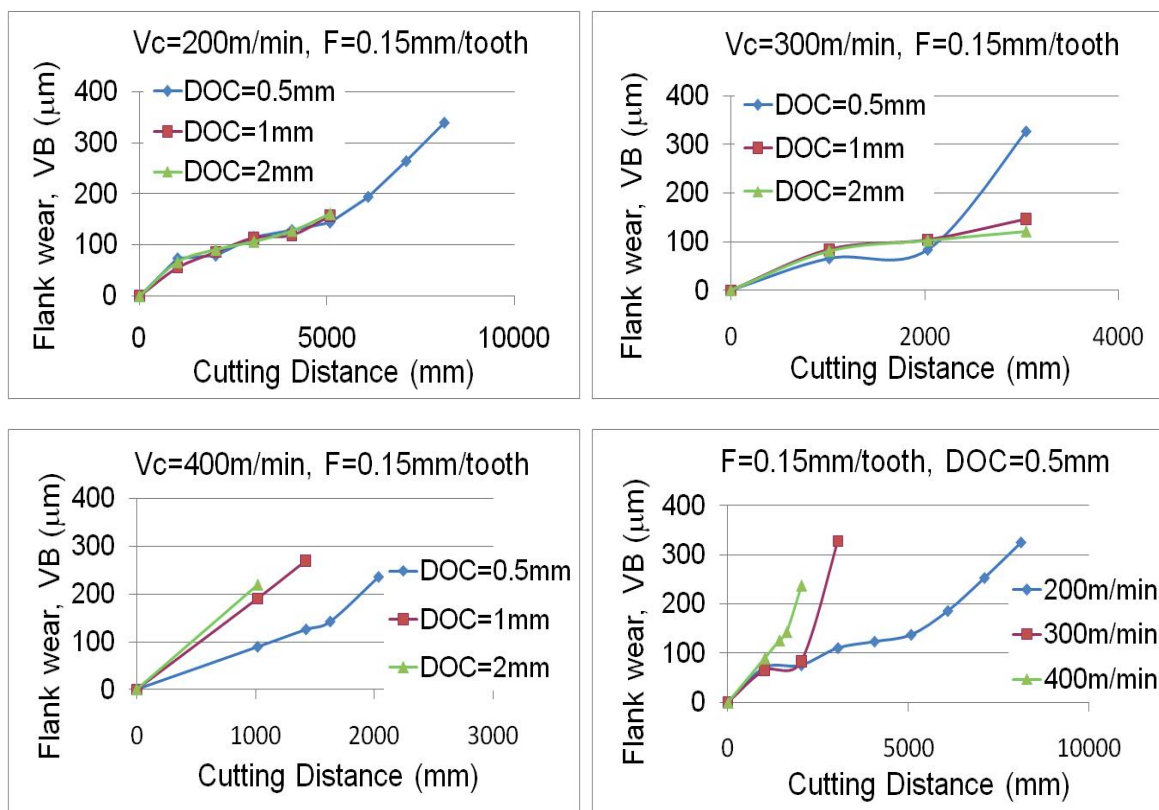


**Figure 27 Flank wear (V$_B$) for triple layer coating at various cutting conditions**

**Figure 27 (cont'd)**
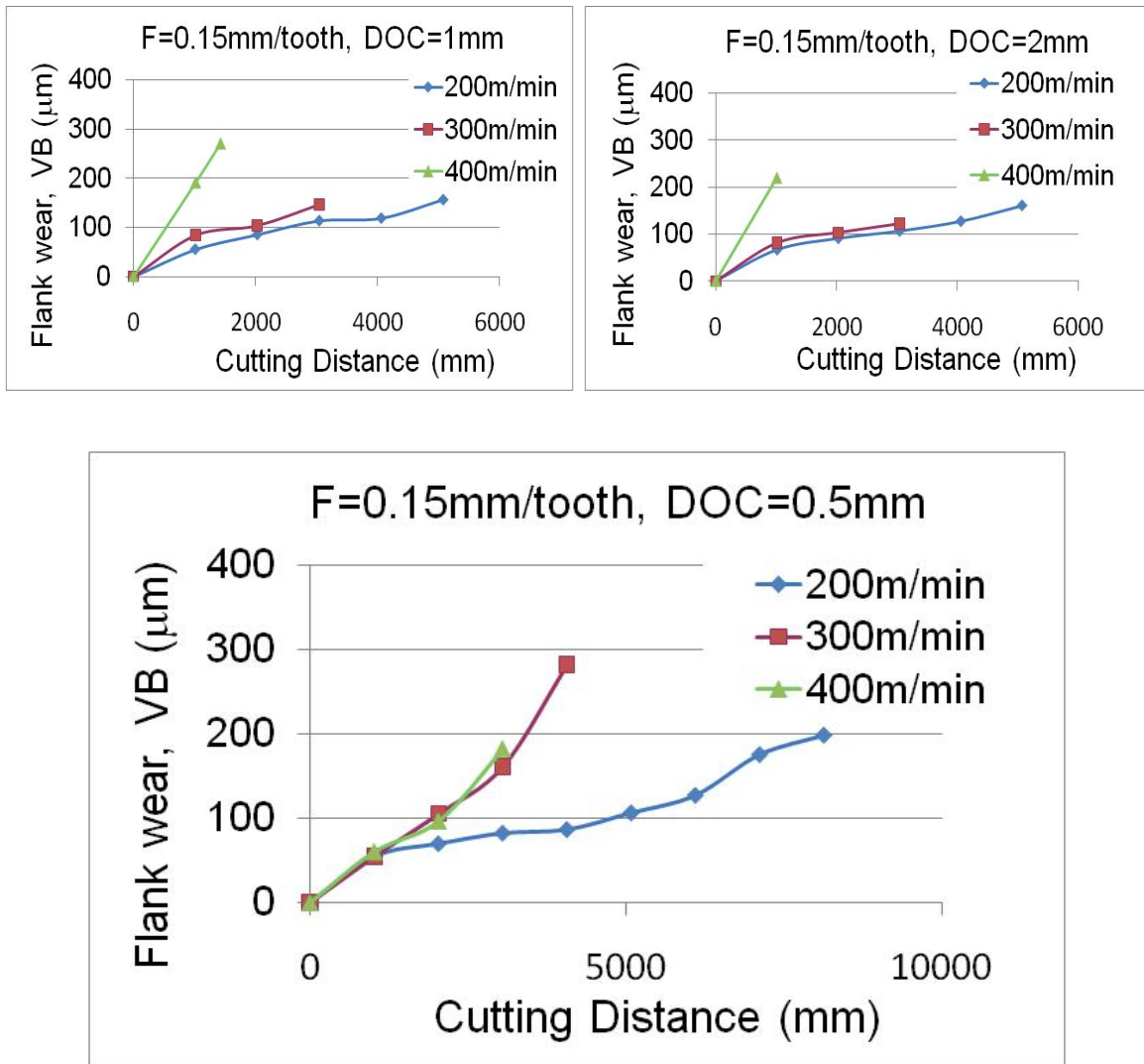


**Figure 28 Flank wear (V$_B$) for double layer coating at various cutting speeds**

Figure 29 represents the flank wear land (V$_B$) for both double and triple layer coating at

cutting speeds where the solid lines and dot lines indicate the double and triple coatings

respectively. It shows that the double layer coating outperformed the triple layer coating

regardless of the cutting speeds. Especially at 200m/min, the flank wear rate for the double layer

is much smaller than that for the triple layer. The chipping occurred at the entire cutting edge at

the triple layer coating while no significant edge chipping was observed for the double layer coating. To explain the reason for the double layer tool outperforming the triple layer tool observed in the experiment, the hardness of the coatings has to be taken into account first due to the fact that the dominant wear mechanism at flank is the abrasion. In this work, the hot hardness of the CVD and PVD coatings could not be directly measured. However, it was reported that TiCN coating is slightly harder than TiAlN coating below 800ºC [Cung-Chen and Hong, 2002] and the hardness of PVD TiCN coatings was greater than that of the CVD TiCN coatings [15]. In this regard, it can be inferred that the hardness of the double layer (TiN/TiAlN-PVD) coating could be similar or slightly higher than the triple layer (TiN/Al$_2$O$_3$/TiCN-CVD) coating.

Another factor to be considered is the quality of the coating adhesion to the carbide. From the indentation test, it turned out that both coatings (Figure 30 (a) and (b)) showed acceptable adhesion strength quality between HF3 and HF4 as defined in Figure 30 (c) where HF1-HF2 and HF3-HF4 were defined as "preferred" and "acceptable" adhesion quality respectively; whereas HF5-HF6 were classified as "not acceptable" or "insufficient" adhesion [Heinke et al., 1995]. From the analysis of the hardness and adhesion, it cannot be explained conclusively that double (PVD) coating was superior to the triple (CVD) coating.
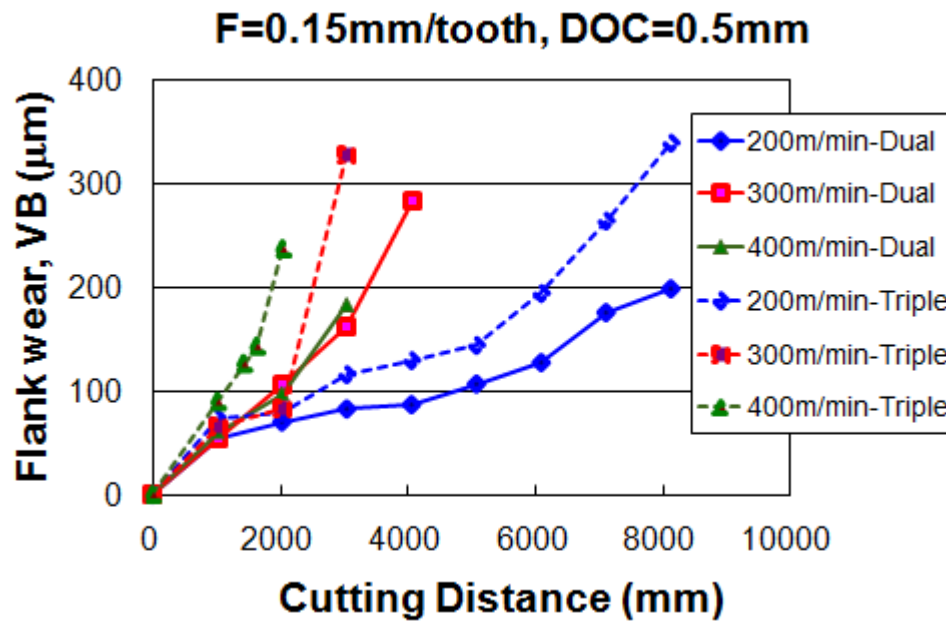
**Figure 29 Flank wear comparison of double (PVD) and triple (CVD) layer coating**
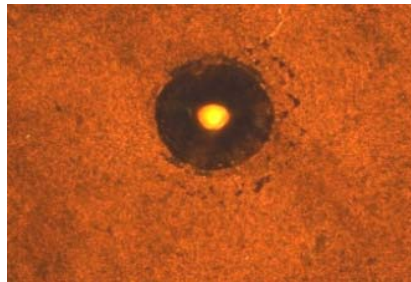


(a) Indentation test for the double CVD coating
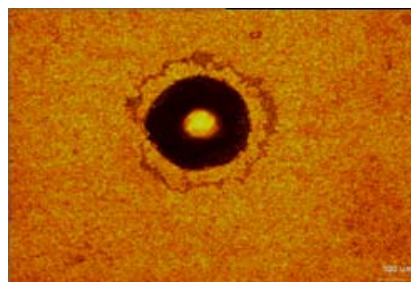


(b) Indentation test for the triple PVD coating

**Figure 30 Indentation tests of PVD and CVD coatings**

**Figure 30 (cont'd)**
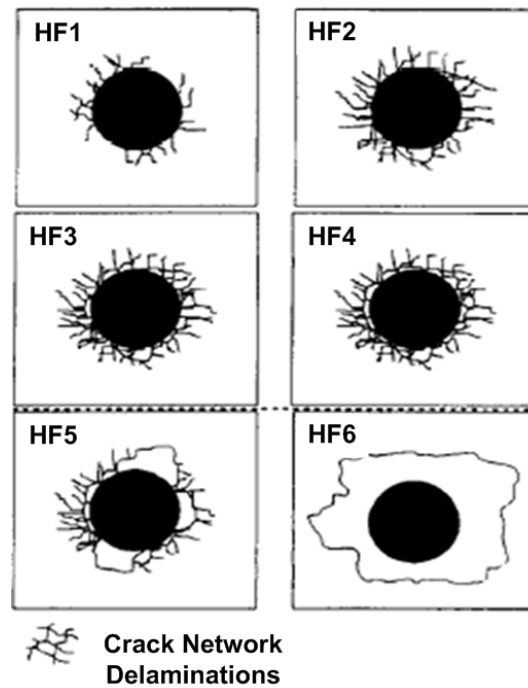


(c) Adhesion quality of coating [Heinke et al., 1995]

However, the inferior performance of the triple layer (CVD) coating can be explained by the reduction of the TRS by formation of the brittle eta phase at the cutting edge by the CVD coating process [Stephenson and Agapiou, 2006 and Jawaid et al., 2000]. In addition, the CVD coating process causes the tensile residual stresses at the cutting surface generated by high deposition temperature in the coating process. As in Table 6, the coefficients of thermal expansion (CTE) of the coating materials are higher than that of the carbide so the CTE mismatch causes the tensile stress at the cutting surface when the tool cools down from a high deposition temperature around 1000ºC. Even the deposition temperature of a medium temperature (MT) CVD method is around 800ºC. Thus, the tensile stress is inherently higher with the CVD process. In addition to the additional tensile stresses associated with the CVD process, the thermo-mechanical loading cycle from the interrupted process can generate and

accelerate the micro-cracks on the cutting tool, which results in the edge chipping and tool failure. On the other hand, the deposition temperature of the PVD process is around 500ºC, which is substantially low compared to that of CVD. Consequently, the PVD coating generally provides free of the thermal crack. In this regard, the PVD coating can be superior to the CVD coating in milling process.

**Table 6 CTE of the tool materials [Wang et al., 1999 and Zhao et al., 2003]**

| Coating Materials | CTE ($10^{-6}$/K) |
|---|---|
| TiN | 9.4 |
| $Al_2O_3$ | 7.8-8.4 |
| TiCN | 8.4 |
| TiAlN | 7.5 |
| WC/Co | 5.0 |

To investigate the wear pattern of the cutting tool, 2D cross-sectional profiles were obtained at cutting distances. Figure 31 shows the flank wear evolutions of the double layer coating at the cutting speed of 200m/min, 300m/min and 400m/min. As seen in Figure 31 (a), the slopes of the profiles on the TiAlN coating are lower than that on the carbide. This means that the high hardness of TiAlN coating reduced tool wear. Again, in Figure 31 (a) the cross sectional profiles up to $3^{rd}$ layer cutting, green line, still stayed on the TiAlN coating but once the carbide was exposed, the wear rate was substantially increased. In addition, the adhesion on the carbide was also observed which might accelerate the edge chipping due to the thermo-mechanical impact during the cutting. This trend becomes more obvious at 300m/min and 400m/min as shown in Figure 31 (b) and (c) respectively. The tool was fractured after the $4^{th}$ layer cutting at 400m/min.
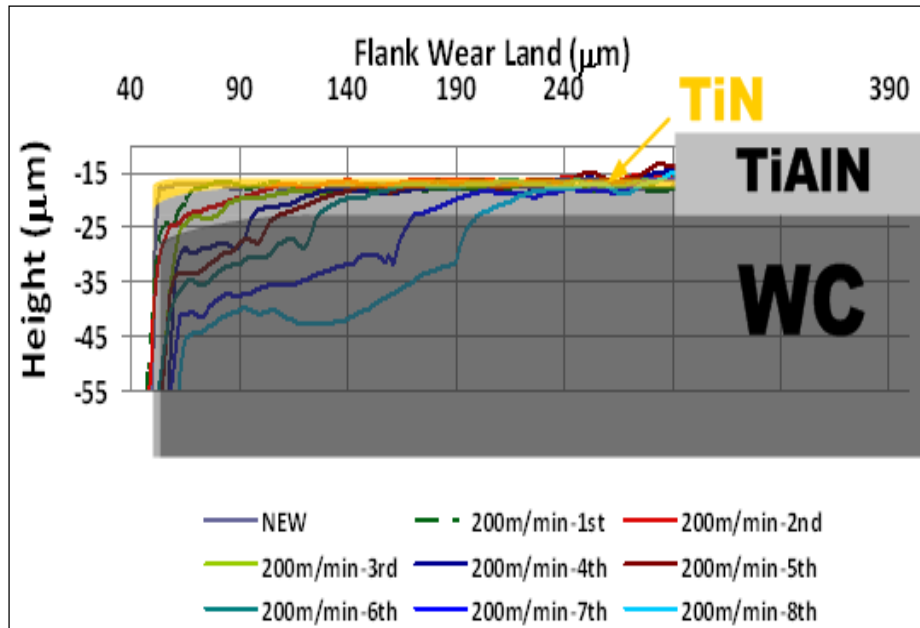
(a) 200m/min
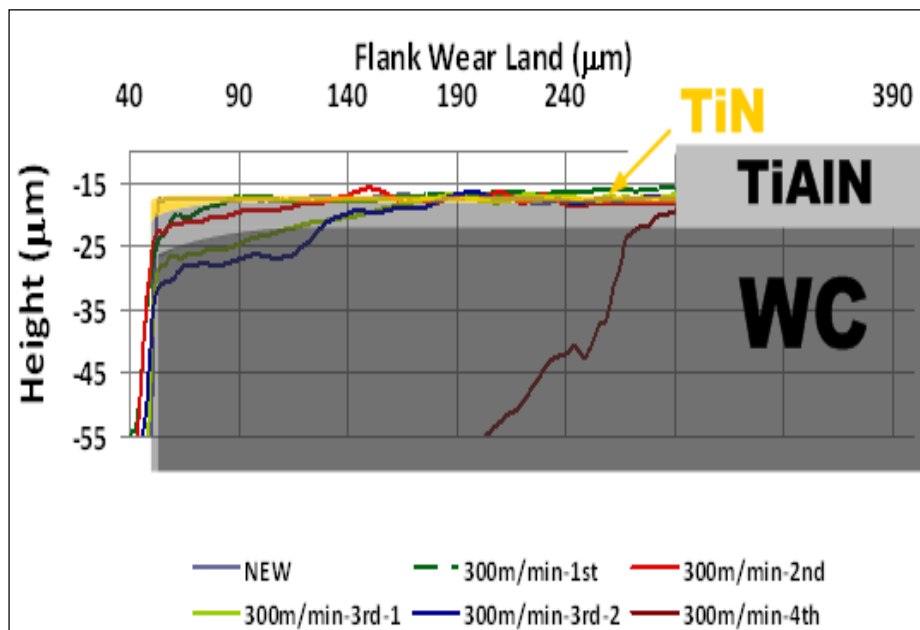


(b) 300m/min

**Figure 31 Flank wear evolutions of double layer coating**

**Figure 31 (cont'd)**
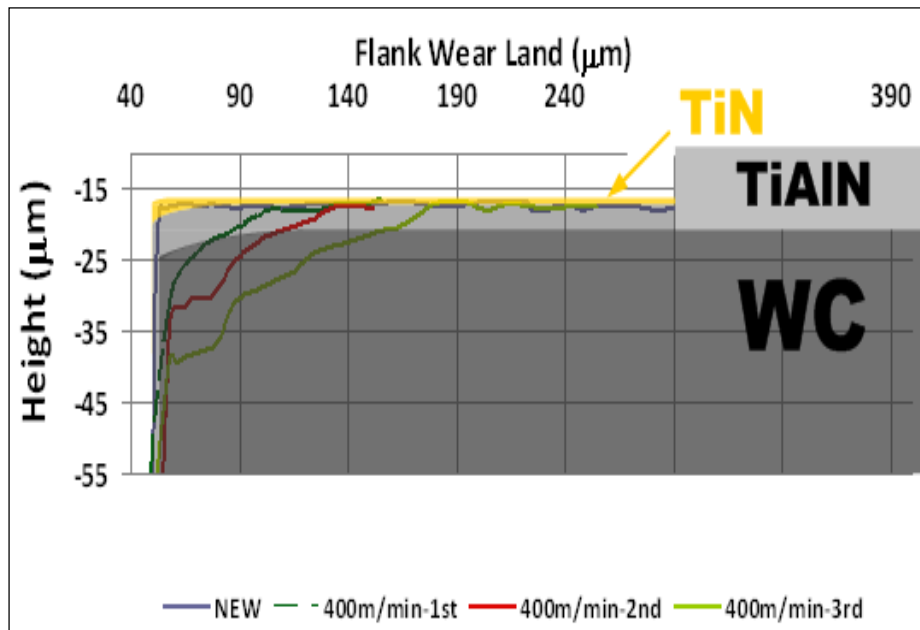


(c) 400m/min

Figure 32 shows flank wear evolution of the triple layer at cutting distances at 300m/min for comparison with the double layer coating. The triple layer coated tools showed the same trend as the double layer coating that flank wear slightly increased up to the first 2 layers cutting due to the hard TiCN coating. However, after the $3^{rd}$ layer cutting, the flank wear substantially increased and the edge chipping was observed. However, the flank wear was much more severe for the triple layer, not only the flank wear land ($V_B$) but also the wear volume. Even the tool was fractured only after the $3^{rd}$ layer cutting for the triple layer coating (See Figure 31 (b) and Figure 32).
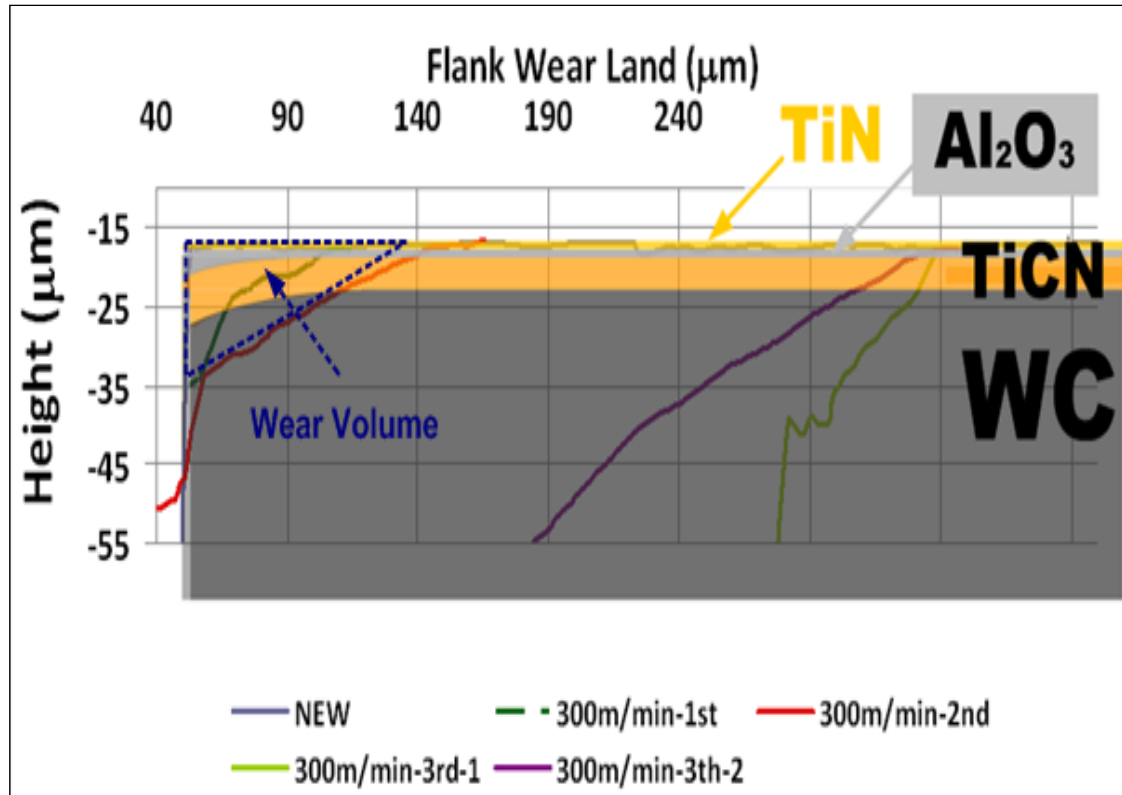
**Figure 32 Flank wear evolution of triple layer coating at 300m/min**

From the observation of the results, the abrasive wear is the dominant wear mechanism at the flank. Thus, the hardness of the coating is of primary importance for flank wear. In fact, the $Al_2O_3$ coating layer with the high dissolution resistance is not needed. In this regard, the harder coating is more preferred to improve the wear resistance of the tool regardless of a coating layer scheme, a single-layer or multi-layer. This argument agrees with other work that the multi-layer coating did not provide better performance in [Sadik and Myrtveit, 2009]. However, in some work, the multilayer can improve the hardness and adhesion strength of coating so that it can perform better than a single-layer coating [Chen et al., 2008]. On top of that, a multi-layer coating can also provide increased thickness of coating, which can reduce the propensity for crack propagation [Cselle and Barimani, 1995]. On the other hand, it is commonly believed that

the superior performance of the multilayer coating comes from the crack advancement

deteriorated by propagating along the coating interface. However, as shown in Figs. 10 and 11,

no cross-sectional profiles show that the crack propagates along the coating interface. Thus, it

can be concluded that a multilayer can improve the coating strength and hardness [Paldey and

Deevi, 2003] so that the wear rate can be reduced when the abrasive wear takes place. However,

it was observed that the benefit of multilayered cutting tools did not come from the wear

resistance enhanced by promoting the interfacial cracks between the coatings. The only benefit

may come from the improvement in the coating strength and hardness [Paldey and Deevi, 2003].

**3.4 CONCLUSION**

The following conclusions can be drawn from the present chapter:

- Double layer (PVD) coating outperformed triple layer coating (CVD) in face milling of AISI 1045 steel due to inherent advantages of the PVD coating deposition process.

- The 2D cross-sectional profiles of flank surface at cutting distances were obtained using the combination technique of CLSM and 2D wavelet transform in order to investigate the flank wear patterns and evolution under various cutting conditions.

- Both TiCN and TiAlN coatings show high wear resistance against the abrasion while the carbide has the least resistance in wear. After the carbide was exposed, the work material adhered to the carbide layer, which could cause edge chipping.

- Only the abrasive wear is dominant until the carbide was exposed. Mainly, the flank wear rate was dependent upon the hardness of the coating materials. Thus, to resist flank wear, a harder coating, not necessary in a multi-layer scheme, is essential.

- A multilayer scheme did not provide a benefit by propagating the crack along the interfaces since the hardness of coating is more of importance to resist flank wear. However, the multilayer scheme may improve the coating strength and hardness in some applications and enhance the wear resistance.

Chapter 4

## TOOL WEAR IN DRILLING OF COMPOSITE/TITANIUM STACKS WITH CARBIDE AND POLYCRYSTALLINE DIAMOND TOOLS

Hybrid structures provide structural advantages to components made from different materials. In hybrid structure, various materials may work together or independently, but are always better than a single material. In aerospace structural applications, the hybrid structure of carbon fiber reinforced plastics (CFRP) composite and titanium (Ti) stack has been widely utilized due to its corrosion resistance and unique ability to withstand high stress in service [Zitoune et al., 2010, Brinksmeier and Janssen, 2002, Lantrip, 2008, Kim and Ramulu, 2007 and Ramulu et al., 2001]. Drilling is essential to the stacked structures when conducting riveted assemblies and structural repairs.

In the present work, tool wear mechanisms when drilling of CFRP-Ti stacks are investigated. The drilling experiments were conducted with the tungsten carbide (WC) and PCD tools with two different drilling speeds. The tool wear mechanism on the drills was characterized through the microscope techniques such as scanning electron microscopy (SEM) and confocal laser scanning microscopy (CLSM). The flank wear progression was also obtained by height encoded (HE) image by CLSM and image processing program in Matlab Software. The relations between drilling forces and tool wear measured will be discussed and the tool wear mechanisms for WC and PCD tools in drilling CFRP-Ti stacks will be summarized.

## 4.1 TOOL WEAR IN DRILLING

### 4.1.1 CFRP drilling

A large part of research in the area of drilling CFRPs has been concerned with the hole quality issues during the process. Since König and Grass [Konig, et al., 1985] studied the hole quality parameters in drilling CFRPs and proposed the concept of the 'critical thrust force' causing exit-ply delamination [Konig, et al., 1985]; composite damage or delamination, in particular, during the drilling process has been extensively studied. Hocheng and Dharan, [1990] proposed a mathematical model of exit hole delamination with respect to the critical thrust force. Other researchers [Jain and Yang, 1993, Hocheng and Tsao, 2003, Lachuad et al., 2001, Upadhyay and Lyons, 1999, Zhang et al., 2001 and Gururaja and Ramulu, 2009] developed analytical models to predict the critical thrust force for delamination free drilling. Several research works have also been performed on tool material and wear mechanism in the drilling of CFRPs. CFRP is a highly abrasive material, depending on direction of the fiber in the matrix, which produces severe tool wear. Unlike metals, CFRP cutting involves not only tool edge chipping but also excessive abrasive wear due to the hard carbon fibers [Faraz et al., 2009, Rawat and Attia, 2009, Lin and Chen, 1996 and Chen, 1997]. It has been commonly found that the wear on the WC tools is generally smooth and uniform along the entire cutting edge of a tool. The dominant wear mechanism on the WC tool in high speed drilling was edge micro-chipping and abrasive wear by the hard fractured graphite fibers and carbide grains. Furthermore, the carbon fibers can attack Co binder, which is relatively soft, causing to lower the binding force of the carbide grains, which can accelerate tool wear and crack propagation [Rawat and Attia, 2009]. The flank wear on the WC tool, when drilling CFRP, was significantly affected by cutting

speed. The highest cutting speed occurs at the outer corner of the cutting edge, the round area of the outer corner of the cutting edge grows as the drill penetrated further into the work material. At higher drilling speeds, the rounded area at the outer corner of cutting edge grows faster than at lower drilling speed [Lin and Chen, 1996]. Several empirical models were proposed by the researchers [Tsao, 2008, Lin and Ting, 1995 and Iliescu et al., 2010] to relate the tool wear and the drilling process parameters such as the feed rate and the cutting speed. The PCD tool is commonly used for cutting composites because PCD tools have high wear resistance against abrasion due to its high hardness [Klocke and Wurtz, 1999, Davim and Antonio, 2001, Nabhani, 2001, Ramulu et al., 1999 and Teti, 2002]. PCD tools reduced wear rate and improved hole quality when compared to HSS and WC tools in drilling of a CFRP composite. It was found that a small amount of micro-chipping was observed when drilling CFRP composites using a PCD drill [Ramulu et al., 1999]. Due to its superior wear resistance, PCD has been the preferred tool for drilling CFRP [Garrick, 2007].

## 4.1.2 Ti drilling

Tool wear mechanisms in drilling Ti are totally different from those in drilling CFRP. In the case of Ti drilling, the distinctive material characteristic, such as low thermal conductivity and strong chemical affinity to tool materials, leads to the reduction in tool life and might cause catastrophic tool failure [Zhang et al., 2008 and Sharif and Rahim, 2007]. In addition, in Ti machining, the contact area between chip and tool is shorter than that in steel machining. Smaller contact area results in stress concentration at tool edge where the maximum cutting temperature is reached. This can cause edge chipping or tool fracture [Hughes et al., 2004 and Stephenson and Agapiou, 2006]. Coated drills suffered less damage, which suggested that the hard coating

material protected the tool and substantially reduced the wear rate of the substrate [Sharif and Rahim, 2007]. When drilling Ti, Ti chips can be easily welded to the cutting edges of the drill and formed built-up-edge (BUE), which leads to chipping and premature failure of the tool. A PCD drill is one of the hardest materials, showing high wear resistance, and also has low friction characteristic and thermal conductivity. However, due to the brittleness nature, the PCD tool can fracture in drilling Ti mainly at high cutting speeds [Sharif and Rahim, 2007 and Garrick, 2007]. Therefore, it is recommended that PCD drill needs to be operated at relatively lower cutting speed than that of WC tools. The machining conditions in drilling play an important role on tool wear, tool life and hole quality.

Tool wear in Ti drilling is very sensitive to the drilling process parameters such as feed rate, cutting speed, and coolant as well as the drill geometry and material [Zhang et al., 2008]. Increasing feed rate and/or cutting speed increased tool wear. In particular, a small change in cutting speed could cause a very large change in tool wear rate [Yang and Liu, 1999]. A list of optimal drill geometry (such as drill point angle, chisel angle, lip relief angle, splitting angle, and the angle of notch) for drilling Ti was proposed by Barish, [1988]. Zhu and Wang, [2006] listed the order of these factors affecting tool wear (from greater to smaller) as: relief angle, rake angle, eccentricity of drill point, and side cutting edge angle. It was also reported that a drill material with higher hardness and higher density was more wear-resistant [Zhu and Wang, 2006].

### 4.1.3 Hybrid structure drilling

Drilling of hybrid composite structures including CFRP and metal stacks has been studied for about a decade [Zitoune et al., 2010, Brinksmeier and Janssen, 2002, Kim and Ramulu, 2007, Ramulu et al., 2001, Kim and Ramulu, 2004 and Park et al., 2010]. Drilling of CFRP-metal stacks at once poses several challenges due to different machinability of two or more distinct materials. Different machining properties of the materials often lead to severe tool wear, which often causes increased drilling forces, poor hole quality and large metallic burrs in CFRP-metal stack drilling [Zitoune et al., 2010, Brinksmeier and Janssen, 2002, Kim and Ramulu, 2007, Ramulu et al., 2001, Kim and Ramulu, 2004 and Park et al., 2010]. Stack drilling, also, requires different optimal machining conditions for each material [Kim and Ramulu, 2004]. It means that the ideal tooling solution for metal is not the most cost effective for CFRP and the ideal tooling solution for CFRP cannot cut metal effectively [Kim and Ramulu, 2004]. For example, PCD has long been the preferred method of drilling CFRP, while WC drill bits have been the preferred tool for drilling Ti. It was reported that the tool selection in drilling CFRP-Ti stacks should match well with the Ti drilling condition rather than the CFRP drilling condition. Excessive heating caused by Ti machining induced a number of hole quality problems in CFRP [Ramulu et al., 2001, Kim and Ramulu, 2004].

## 4.2 EXPERIMENTAL PROCEDURES

### 4.2.1 Workpiece materials

The CFRP laminates acquired from The Boeing Company were multidirectional graphite epoxy composites consisting of graphite fibers and an epoxy matrix with a quasi-isotropic ply orientation of $[(90^o/-45^o/0^o/45^o)_4/0^o/90^o/0^o/90^o]_s$. The CFRP laminate had a thickness of 7.54mm with an average ply thickness of 0.1141mm. The titanium plate material used is Ti-6Al-4V with a thickness of 6.73mm. To obtain the grain size, a sample of the Ti was etched using Krolls etchant. Using ASTM E112 Section 11 standard, the ASTM grain size number was calculated to be 10.95. This number corresponds with an average $\alpha$-grain size of 8µm.

### 4.2.2 Drilling experiments

Two types of twist drill materials were selected for this investigation based on their availability and widespread usage in industry: WC and PCD. Both drills have a diameter of 9.525 mm and point angle of 135 $^o$. The PCD drill has slightly larger dimension for the flute length and the web thickness. The larger web thickness gives the drill a more ridged body, but also can translate into a slightly higher thrust force. Table 7 summarizes the geometry dimensions of the drills used in the experiment.

Drilling experiments were performed on a commercially available 3-axis CNC vertical mill (MiniMill, HAAS, USA). The stack sequence of CFRP on top of Ti is typical stacking sequence in aircraft structure assembly. The dynamometer (TRS-1K-OPT-THR, Transducer Techniques, USA) had a fixture mounted on it to hold the stacks and ensure accurate force data.

The stacked materials were clamped to the fixture to enable any movement while drilling, this way the force experienced by the materials will directly translate to the dynamometer. While drilling, the thrust and torque forces were transmitted from the dynamometer to signal amplifiers, A/D board (NI USB-6251, NI, USA) and recorded on a personal computer (PC) with data acquisition software (LabView 7.1, NI, USA). The entire experimental step is shown below in Figure 33.

Drilling experiment conditions were summarized and shown in Table 8. In order to investigate how drilling speed effects WC tool wear, two different speeds (high speed and low speed) were selected. CFRP and Ti are two materials that have very different optimal machining settings. It is because of their dissimilar properties that the CNC mill was programmed to change speed and feed depending on the material type. For each high speed or low speed drill, two speeds are given depending on the material type. For example, the high speed for CFRP is set at 6000rpm while the high speed for Ti is set at 800rpm. The low speed WC tool drilled CFRP and Ti at 2000rpm and 300rpm, respectfully. The drilling feed rate (mm/rev) also changes with the material type and is shown in Table 8. CFRP is best machined at a higher speed and higher feed. Titanium's thermal properties limit the speed and feed. That is the reason that the speed and feed of titanium is lower than that of the CFRP. By changing the speed and feed like this, each material can be drilled at its optimum machining settings which will translate into a longer tool life and a lower cycle time. A water-soluble cutting fluid was used as a mist coolant throughout the operation with a constant flow rate of 16mL/min.

**Table 7 Drill geometries**

|  | WC (9% Co ultra-fine grain) | PCD (Bimodal grade) |
|---|---|---|
| Drill diameter (mm) | 9.525 | 9.525 |
| Flute length (mm) | 49.15 | 50.04 |
| Overall length (mm) | 100.3 | 100.6 |
| Web thickness (mm) | 0.853 | 0.953 |
| Cutting lip length (mm) | 5.115 | 5.115 |
| Point angle (deg.) | 135 | 135 |
| Helix angle (deg.) | 28 | 28 |
| Lip relief angle (deg.) | 72 | 72 |
| Chisel edge angle (deg.) | 45 | 45 |
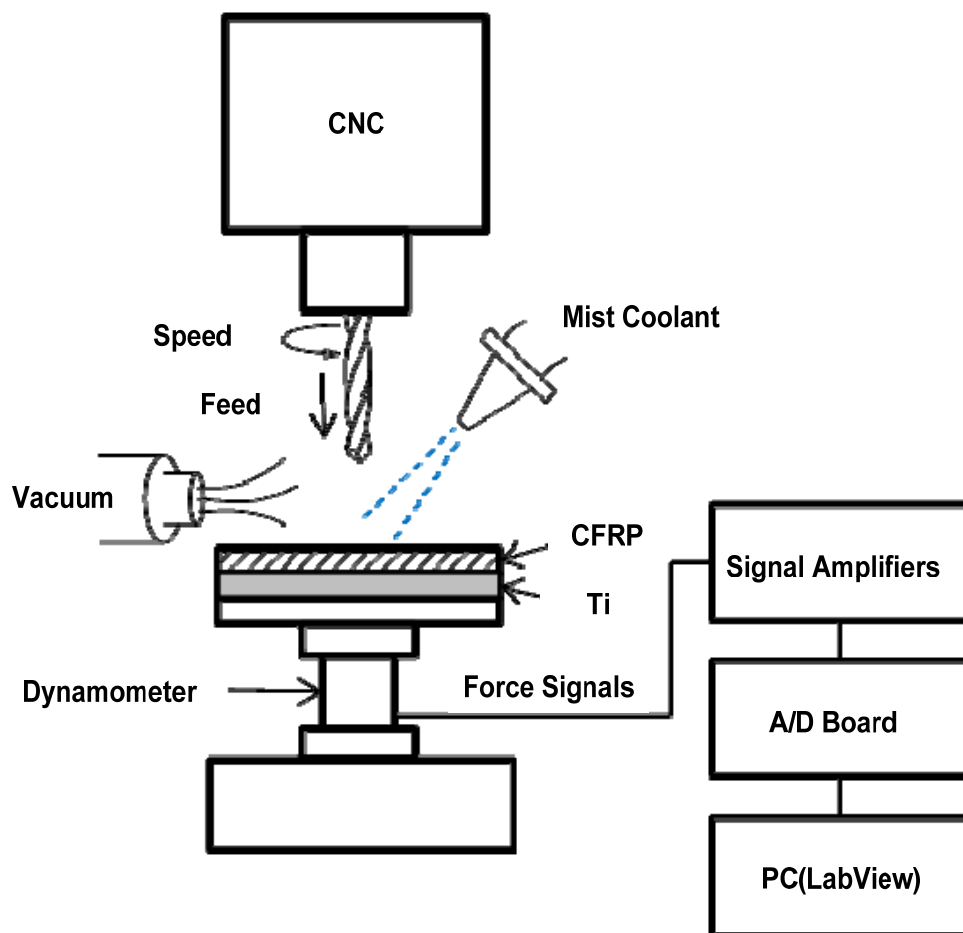
**Figure 33 Schematics of drilling experimental set up and drilling force data acquisition system**

**Table 8 Drilling experiment conditions**

|  | Tool | RPM in CFRP | RPM in Ti |
|---|---|---|---|
| High speed | WC | 6000 | 800 |
| Low speed | WC | 2000 | 400 |
|  | PCD | 2000 | 300 |
| Feed: 0.0762mm/rev (CFRP), 0.0508mm/rev (Ti) <br> Coolant: Water-soluble cutting fluid, Mist coolant flow rate at 16 mL/min. | | | |

## 4.2.3 Wear evolution analysis

Tool wear was has been measured typically using a number of instruments and techniques that include a tool-maker's microscope, profilometer, white-light interferometry and SEM. Most of these techniques cannot measure full 3 dimensional (3D) images required for detailed analyses of tool wear. We have developed a new method of measuring tool wear in 3D using CLSM [Park and Kwon, 2009 and Olortegui-Yume and Kwon, 2010]. The image processing program, manly using wavelet filtering from CLSM, has been developed to eliminate the noises and artifacts inherent to the height encoded (HE) image obtained by the CLSM. The techniques introduced in [Park and Kwon, 2009 and Olortegui-Yume and Kwon, 2010] have enable us to determine where the smooth contour due to dissolution or the scoring marks due to abrasion has occurred and what inclusion has caused the abrasive wear. The wear evolution of each drill was constructed by interrupting the drilling process after drilling a specified number of holes (20 holes) on CFRP/Ti stacked materials. This enables us to examine and analyze the tool wear mechanisms as the wear progresses into the drill. In this paper, because of the pronounced adhesion layer of Ti on the cutting edge, we were able to use the same technique to estimate the amount of the adhesion layers on various drills.

## 4.3 RESULTS AND DISCUSSION

### 4.3.1 Drilling forces

Figure 34 shows the drilling force change over the number of holes drilled. Given that the stack structure is two different materials (CFRP on the top and Ti on the bottom), maximum thrust and torque values were indicated separately for CFRP and Ti. When the drills were new, both the drilling thrust and torque of the WC drill were 40% to 60% lower than those of the PCD drill mainly due to the difference in tool geometries. As shown in Table 7, the web thickness of the PCD drill was approximately 40% larger than that of the WC drill. The results agree well with the previous experimental study results, which showed the drilling forces increase with increasing web thickness [Chen, 1997]. As the number of holes drilled increase, the drilling forces of both WC and PCD drills gradually increase in both CFRP and Ti. This increase is mainly due to tool wear. Note that the drilling forces produced by WC drill at high speed increased much faster than those at low speed. For the PCD drill, the thrust force did not increase much over the number of holes drilled. In addition, the torque produced by PCD did not show any significant overall increase over the number of holes drilled.
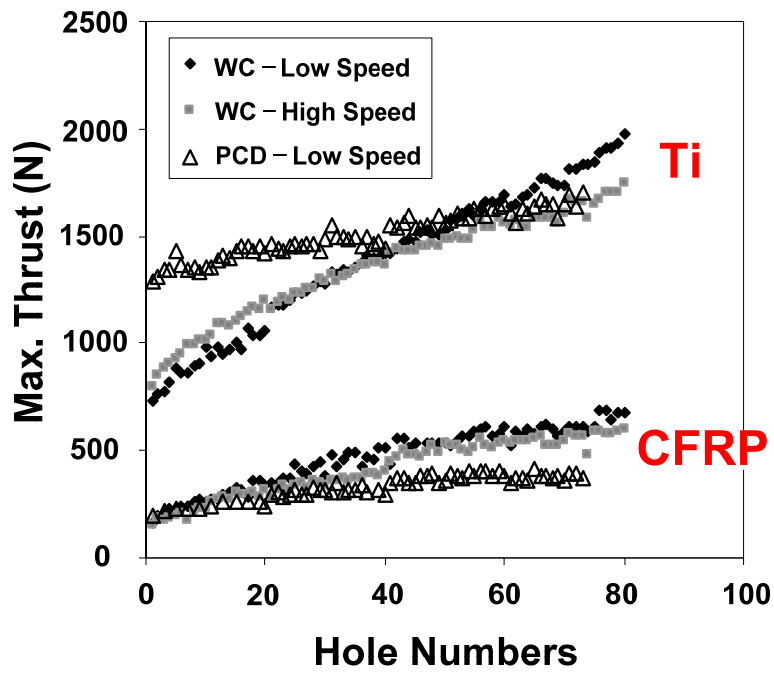
(a) Thrust force
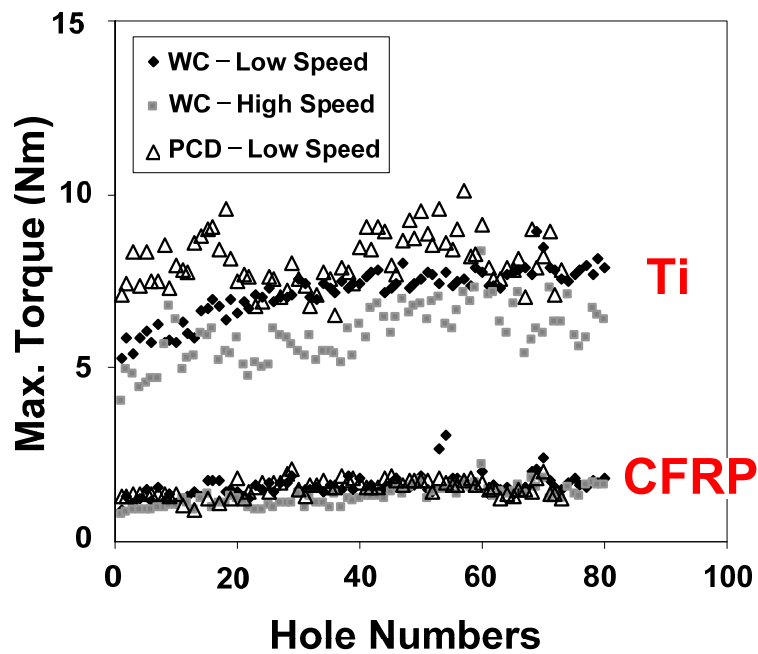


(b) Torque

**Figure 34 Cutting forces vs number of holes drilled by the different tool types and conditions**
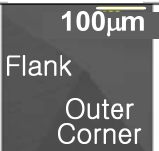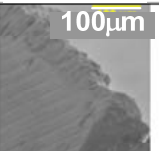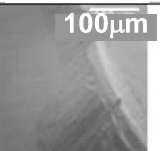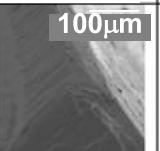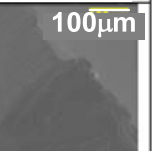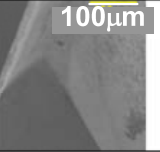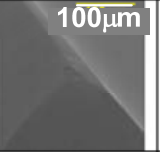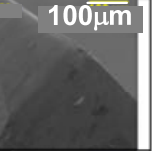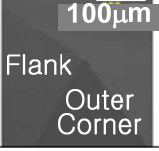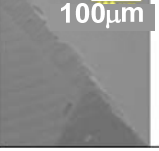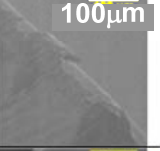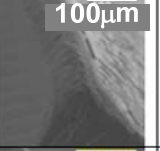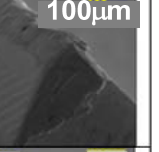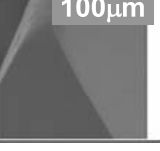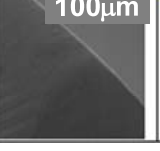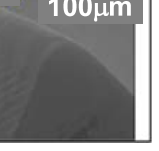
**4.3.2 WC drill wear**

Table 9 shows the SEM images of WC drills up to hole 80. The images mostly cover flank face, cutting lip or cutting edge, and outer corner. Given that the stacking sequences of the stacks are CFRP on top of the Ti, Ti adhesion is observed on all the drills after drilling a set of 20 holes. Adhesion is a well-known characteristic in Ti drilling due to the high chemical affinity to typical tool materials [Park et al., 2010]. The adhesion leads to build-up edge (BUE) formation, which is an accumulation of work material on the cutting edge best shown Table 9 for the WC drill after drilling 20 holes. The BUE deteriorates the hole quality and leads to the tool chipping or fracture when the BUE breaks off from the cutting edge. The adhesion was formed as soon as Ti drilling started, and covered a large part of the flank surface especially at the high cutting speed as shown in the CLSM images (Figure 36). More Ti adhesion was observed for the high cutting speed rather than with the low cutting speed. The amount of Ti adhesion is directly related to the chemical reactivity of Ti, which becomes higher at high temperatures.

In order to verify the tool wear geometries and wear progression without Ti adhesion, the WC drills were etched using a Ti wet etchant (20 parts of $H_2O$, 1 part of 30% $H_2O_2$, and 1 part of 49% HF by volume). Micro-fracture or micro-chipping, with the approximate size of 30 microns, was observed at the outer edge on WC drills drilling at high speed after 60 holes. In addition, as shown in Figure 35, the micro-chipping was observed at outer corner edge at hole 40 due to the combination of hard inclusion in Ti and adhesion. The hard inclusion and adhesion of Ti attacked the sharp edge in the direction of scoring marks when Ti adhesion was detached. The micro-chipping was only observed on the WC drills at high speed (large adhesion) while no such chipping was observed on the WC drills at low speed and PCD tools (small adhesion).

**Table 9 SEM images for carbide drills at high and low speeds with various holes**

| Drilling Condition | Tool Condition | Hole Number | | | | |
|---|---|---|---|---|---|---|
| | | Hole 0 | Hole 20 | Hole 40 | Hole 60 | Hole 80 |
| High speed | As-drilled (Before Etching) | 100μm Flank Outer Corner | 100μm | 100μm | 100μm | 100μm |
| | After etching | | Not available | 100μm | 100μm | 100μm |
| Low speed | As-drilled (Before Etching) | 100μm Flank Outer Corner | 100μm | 100μm | 100μm | 100μm |
| | After etching | | Not available | 100μm | 100μm | 100μm |
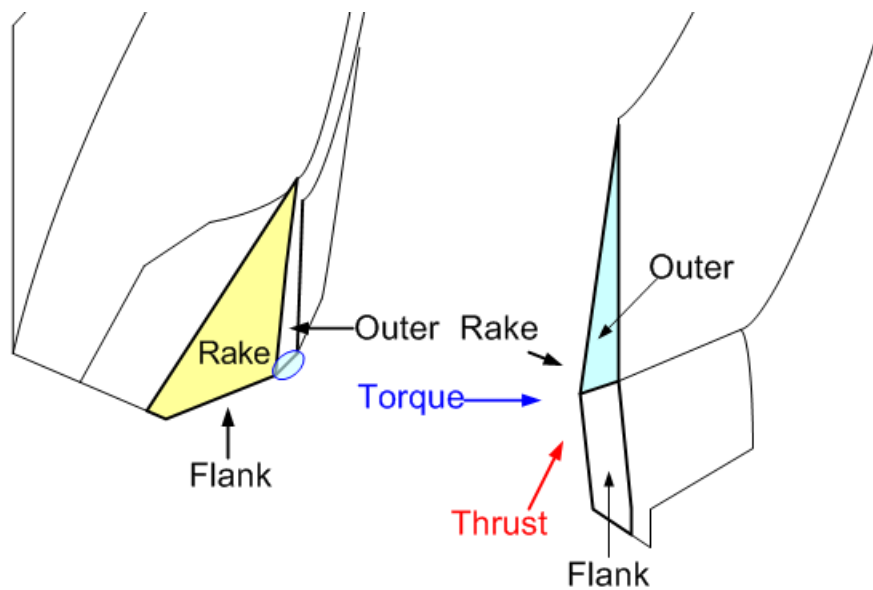


(a) Schematics of drill geometry

**Figure 35 Drill geometry schematics and CLSM images of the WC drill outer corner at high speed after 40 hole**

**Figure 35 (cont'd)**
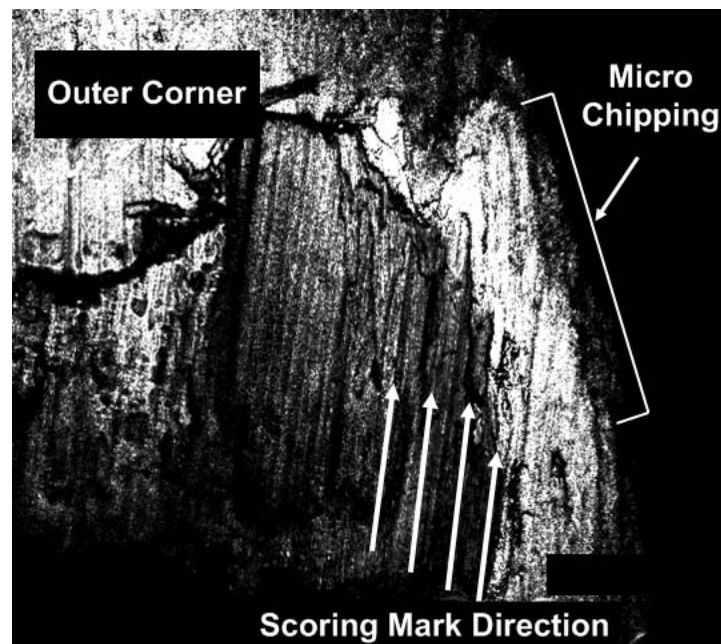


(b) Before etching (10X)
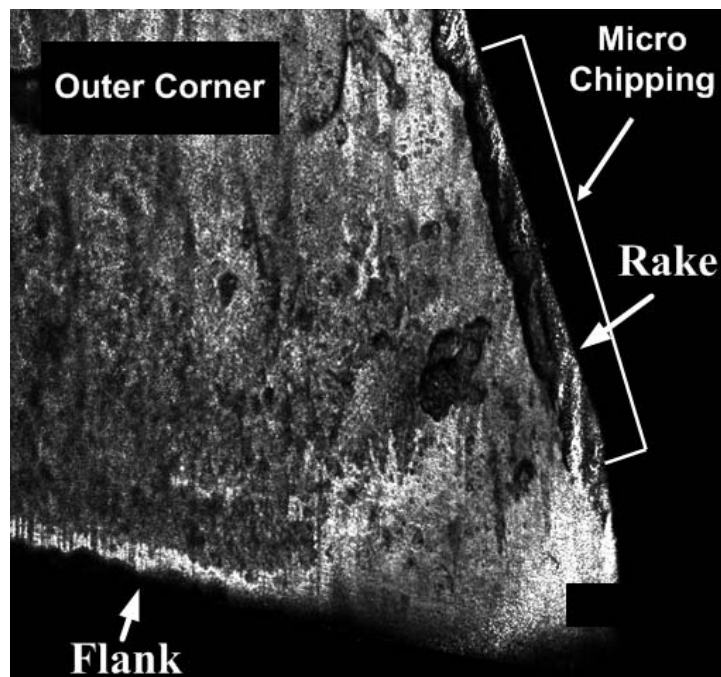


(c) After etching (10X)

To characterize the flank wear and quantity of adhesion for the WC tools, the CLSM was used to take the HE images at every 20 holes with the objective of 50X before and after etching as seen in the Figure 36 (a) and (c). Using the image processing program with wavelets, the noise filtered 3D topographic profiles were obtained as shown in Figure 36 (b) and (d). Figure 36 (a) and (b) illustrates the HE image of titanium adhesion on the cutting edge and corresponding 3D topography image, respectively. On the other hand, Figure 36 (c) and (d) shows HE images and 3D topographic profile of the same tool after the Ti adhesion layer was etched away.
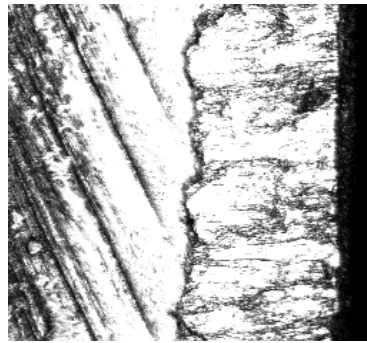


(a) HE image before etching (50X)
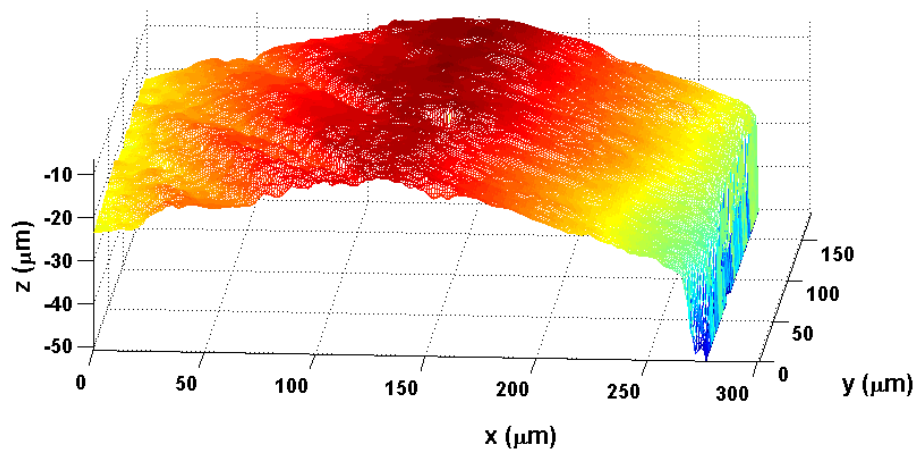


(b) 3D topographic profile before etching

**Figure 36 CLSM images at flank face of WC drill after high speed drilling at 60th hole**

**Figure 36 (cont'd)**
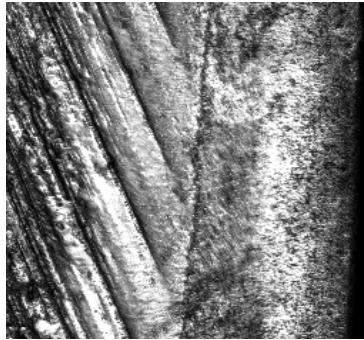


(c) HE image after etching (50X)
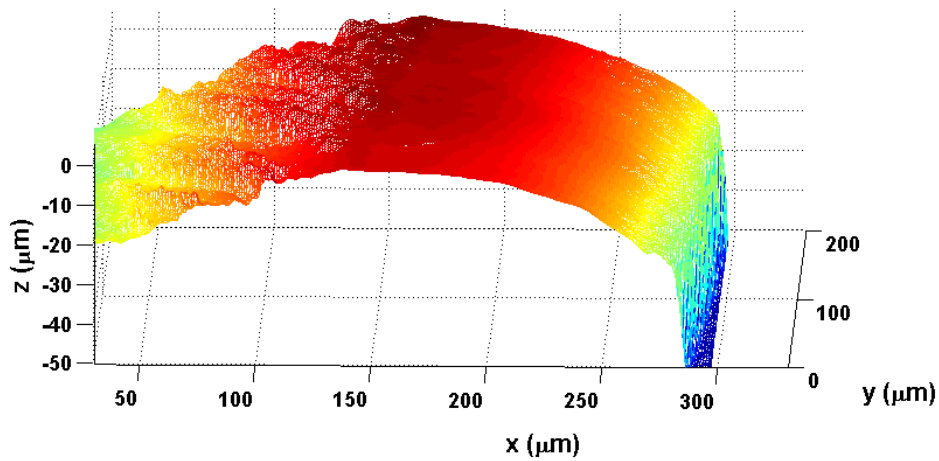


(d) 3D topographic profile after etching

Figure 37 shows the cross-sectional profiles of carbide tool at various hole numbers obtained from 3D topography profiles (Figure 36). The drilled tools have Ti adhesion covering the WC tool surface regardless of drilling speeds (Figure 37 (a)). After Ti removal through etching, the WC tool surfaces can be observed (Figure 37 (b)). From the observation, it was found that wear first progressed on the cutting edge and flank surface at a simalar rate. In this study, therefore, the two major wear types were observed to be flank wear ($V_B$) and edge wear. Edge wear has been identified as a major wear type in machining composite material, where the

cutting edge becomes rounded [Faraz et al., 2009]. Both types of wear were measured after drilling sets of 20 holes as shown in Figure 38. The two wear types were caused by different wear mechanisms due to dissimilar characteristics of the materials in the stacked structure. Flank wear is the main mechanism from abrasion. The complex hard phase within titanium abrades the flank surface after shearing the 3D microstructure. Edge wear is dominant as the fibers are being cut by the cutting edge and the broken side of the fibers are scraping both flank and crater surfaces of the drills.

At high speed drilling, surface profiles evolved as the flank wear land grew, especially after drilling 40 holes, as in Figure 37 (a). At low speed, flank wear and edge wear occurred almost equally as seen in Figure 37 (b). These figures shows the effect of drilling speed on tool wear; much less flank wear was observed at low cutting speed than at high cutting speed while the difference on edge wear was not significant and edge wear rate became steady regardless of drilling speeds. Due to fast evolving flank wear at high speed, thrust force increase more rapidly at high speed over low speed, as shown in Figure 35 (a). On the other hand, the difference in drilling speed did not affect much on edge wear in CFRP cutting but when drilling Ti, especially at high cutting speed, due to low thermal conductivity the cutting temperature became high enough to activate high affinity of adhesion and to soften the WC drill. Softening of the WC tool translates into the softening of the cobalt (Co) binder that holds the carbide grains together. The flank wear is therefore extended by the mechanisms of carbide grains pulled out of the Co binder as the Ti adhesion is removed by the next holes CFRP drilling, in addition to the abrasion by the hard phase in the Ti alloy. In metal drilling, the cutting edge can be partially protected due to the stagnant zone of the cutting edge maintaining the edge more consistently. This is why Ti drilling had greater effect on flank wear rather than edge wear. On the other hand, when drilling CFRP

no stagnant zone is present. Without a stagnant zone the cutting edge becomes rounded and

dulled due to the abrasiveness of the fibers. Therefore, it can be said that flank wear land is

elongated by the Ti drilling and the edge wear is predominately due to the abrasiveness of the

hard carbon fibers when drilling CFRP.
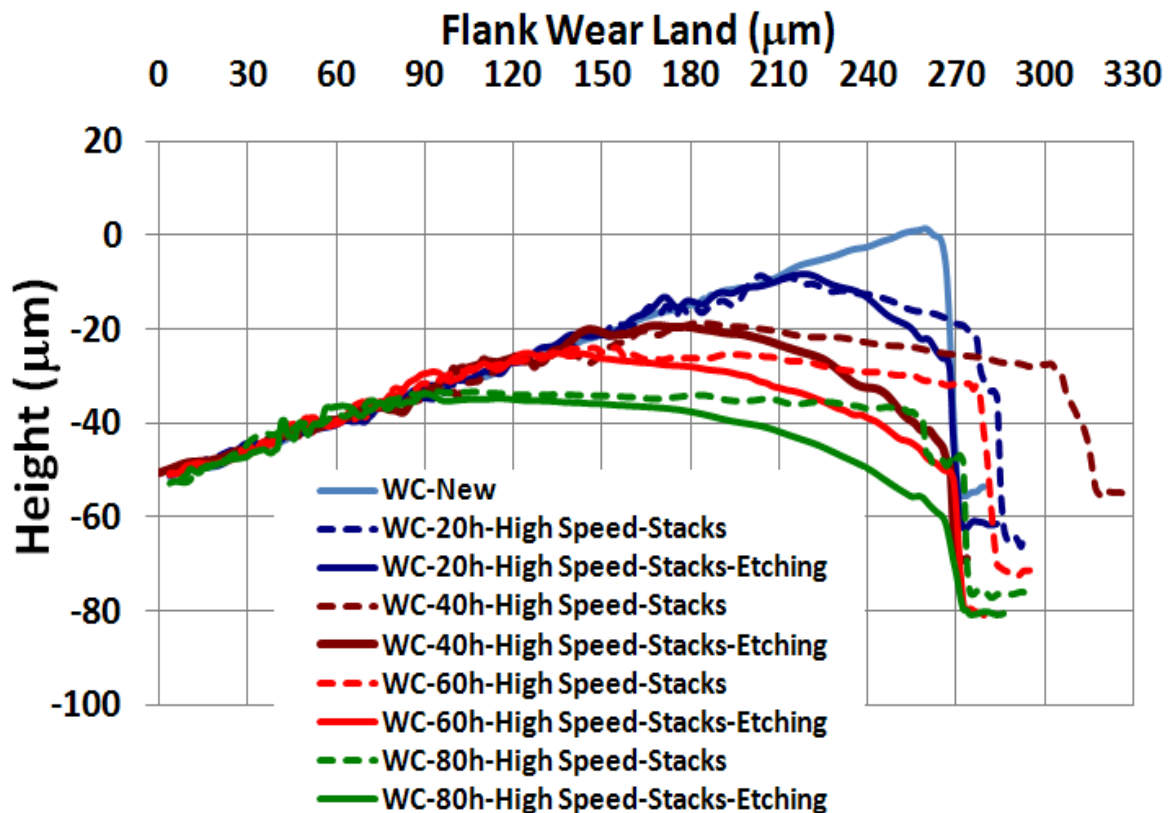


(a) 2D cross-sectional profiles at high cutting speed

**Figure 37 Tool flank wear profiles of carbide drills before and after etching at various speeds**

**Figure 37 (cont'd)**
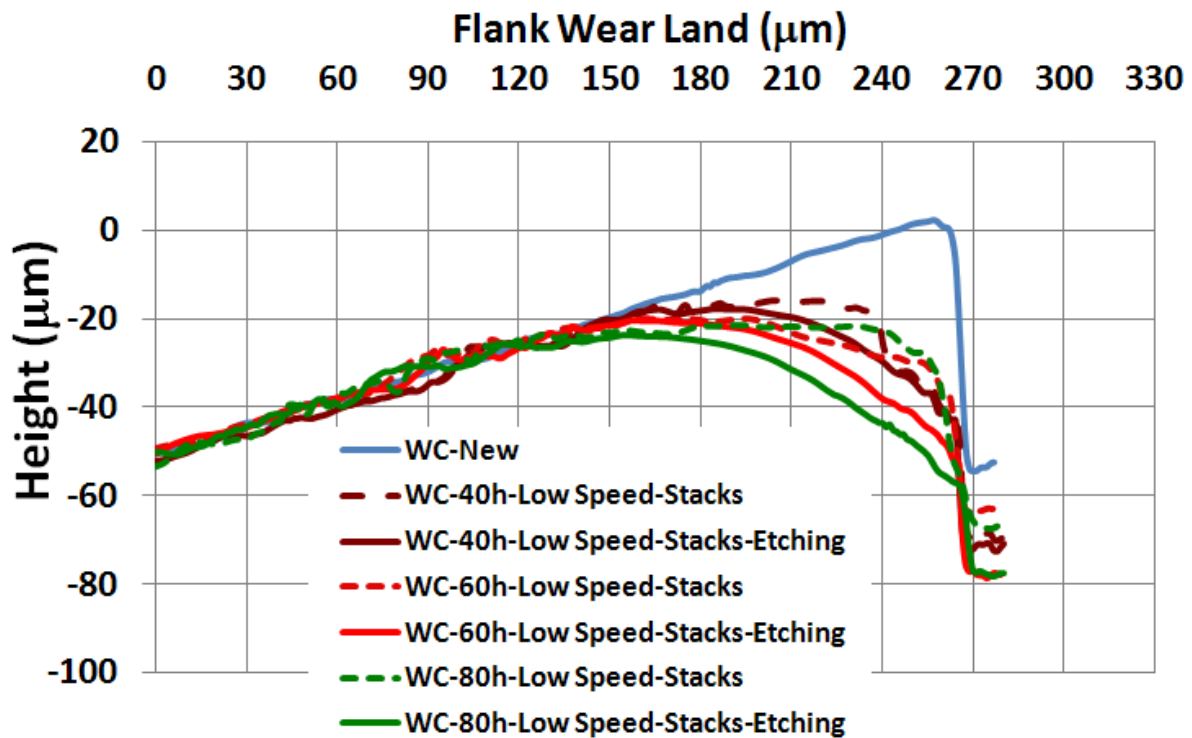


(b) 2D cross-sectional profiles at low cutting speed

When drilling Ti at the low speed, the temperatures of the drills do not increase as much as that of the drills at the high speed. Therefore, low speed conditions do not produce as much flank wear. It was found that this amount of wear is small and similar to the amount of edge wear done by the CFRP producing an evenly rounded tool edge (Figure 37 (d)). It is clearly identified in Figure 6 (c) that the rate of flank wear and edge wear is pretty close for low speed drilling. In relating Figure 38 (b) to (c) you can see how the edge wear has stayed relatively the same, while the flank wear increase exponentially for high speed drilling after around 40 holes drilled due to the cutting temperature. As the cutting forces go up, the cutting temperature increases [Weinert and Kempmann, 2004]. The increase in cutting forces over the hole number as evident in Figure 34.
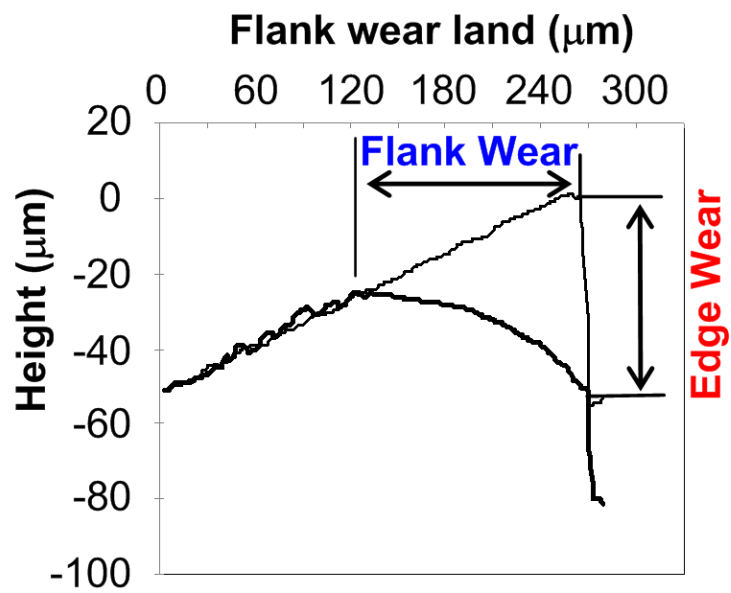
(a) Flank and edge wear measurement
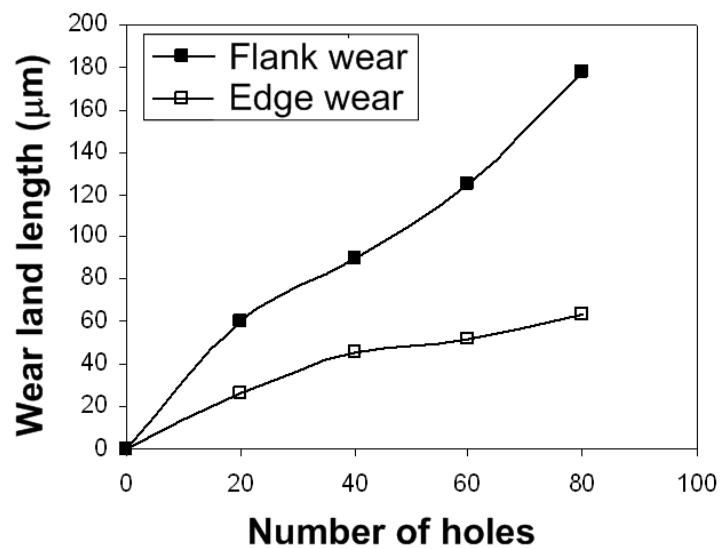


(b) High speed drilling

**Figure 38 Flank and edge wear progression of WC drills for various drilling speeds**

**Figure 38 (cont'd)**
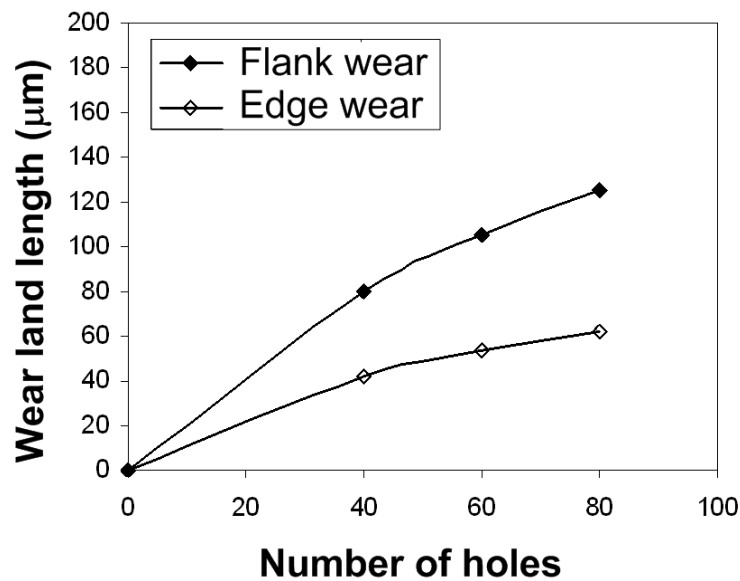


(c) Low speed drilling

Figure 39 shows the effect of wear land size at flank and edge on the drilling forces. Maximum thrust force increases with increasing flank wear length regardless of drilling speed. The flank wear length is proportional to the flank surface area, which is the area normal to the cutting direction. It is for these reasons that as the flank wear length increase, the parallel area of contact between the tool and the work piece increases which translates into increased thrust force. On the other hand, the maximum torque is well related to the edge wear length. As the tool edge rounds and becomes blunter, the area of contact increases resulting in an increase in torque need to cut the materials.
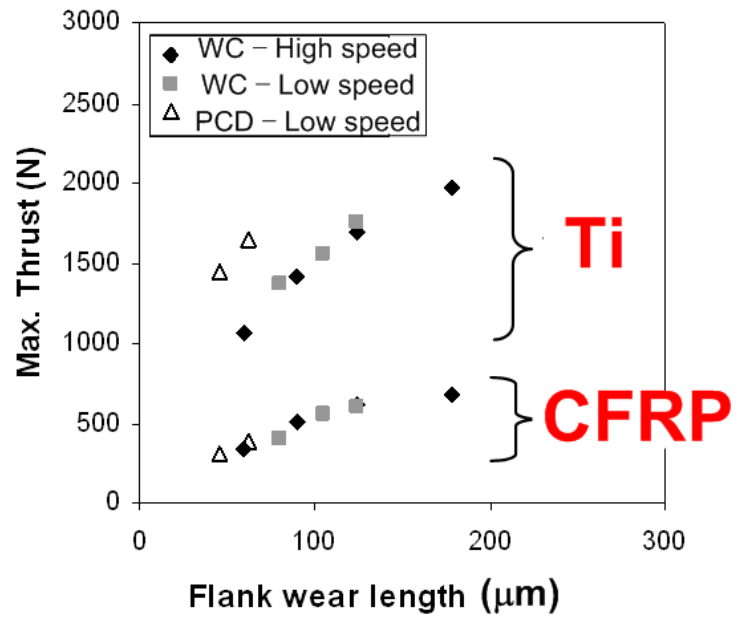
(a) Flank wear length vs maximum thrust
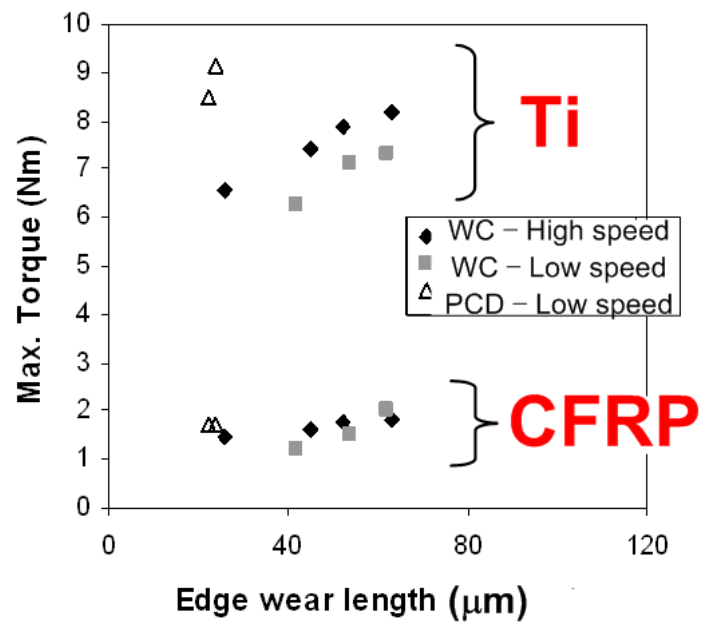


(b) Edge wear length vs maximum torque

**Figure 39 Effect of wear progression on drilling forces**
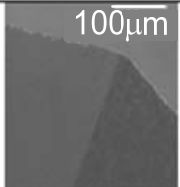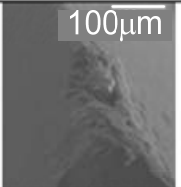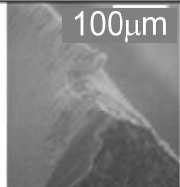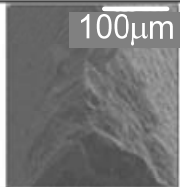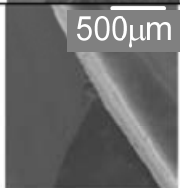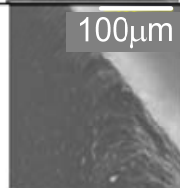
In summary, as the WC drill goes through the top CFRP plate abrasive wear occurs predominately on cutting edge of the drill due to the hard carbon fibers. As, the chisel edge of the drill begins to penetrate the top of the Ti plate and the speed substantially reduces, severe Ti adhesion takes place. In Ti drilling, two different wear mechanisms are involved that mainly wear on the flank face. First, abrasive wear occurs from the hard phase in the Ti alloy and, second, carbide grains can be pulled out of the Co binder as Ti adhesion is removed. After making the first hole, the Ti adhesion on WC cutting edge is brushed away by the carbon fibers when CFRP drilling the next hole. Even after the Ti adhesion is removed, Ti adhesion will be rebuilt on the WC drill cutting edges when drilling the bottom Ti plate.

### 4.3.3 PCD Drill Wear

The PCD drill shows a very small amount of adhesion compared to the WC drill. In general the PCD drill has properties of high thermal conductivity and low friction at the cutting surface [Stephenson and Agapiou, 2006]. Based on these characteristics, we expect that the cutting temperature of the PCD drill be relatively lower than that of the WC drill and, thus result in a reduced amount of Ti adhesion. In general, PCD tools provide lower propensity to adhesion with titanium. However, the major problem with PCD tools is the brittleness. The brittleness of PCD and harsh drilling conditions of the CFRP/Ti stacked material often lead to micro-fractures and catastrophic failure as seen in Table 10. Table 10 shows the progression of the micro-fracture (or chipping) at the cutting edge of the tool for low speed drilling. Moreover, the PCD tool at the higher cutting speed failed catastrophically after making a few holes. The PCD drill failed catastrophically after making the 73$^{rd}$ hole at low speed setting.

91

Figure 40 shows CLSM images displaying micro-fracture on the cutting lip. This micro-fracture might occur as the PCD drill penetrates the Ti plate. The transition between to two materials allows for a slight impact and the beginning of the Ti metal chip. This small chip thickness generates high stress concentration at cutting edge. When you combine that with high cutting temperature due to low thermal conductivity of the Ti plate, edge chipping or fracture can occur in the brittle PCD tool [Stephenson and Agapiou, 2006]. The chipping size on the cutting edge was measured as shown in Figure 40 (d) and (e). The chipping size at hole 60 was approximately 200μm in length and 60μm in depth.

**Table 10 SEM images of the PCD tool at low cutting speed**
**(Tool experienced catastrophic failure at hole 73)**

| Drilling Condition | Tool Condition | Hole Number | | | |
|---|---|---|---|---|---|
| | | Hole 0 | Hole 20 | Hole 40 | Hole 60 |
| Low speed | As-drilled (Before Etching) | 100μm | 100μm | 100μm | 100μm |
| | After etching | | Not available | 500μm | 100μm |
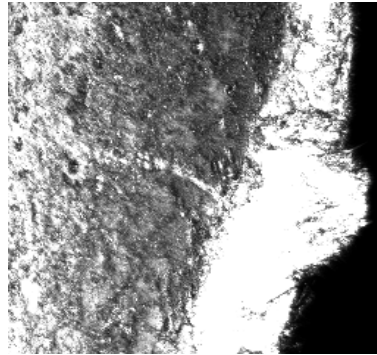
(a) HE image before etching (50X)
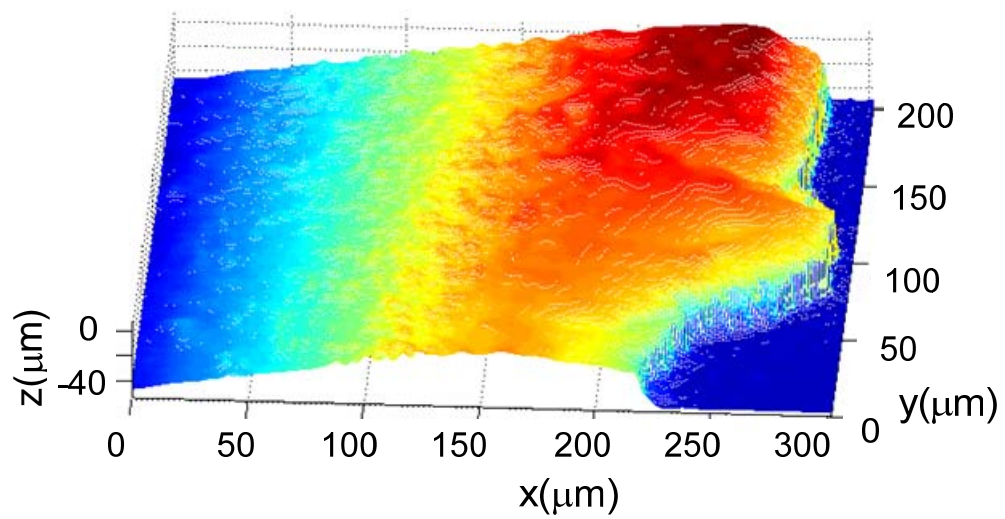


(b) 3Dimensional profile before etching
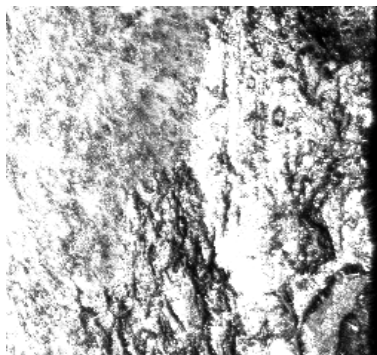


(c) HE image after etching (50X)

**Figure 40 Micro-fractures observed on flank side of PCD at low speed drilling and at hole 60**

**Figure 40 (cont'd)**
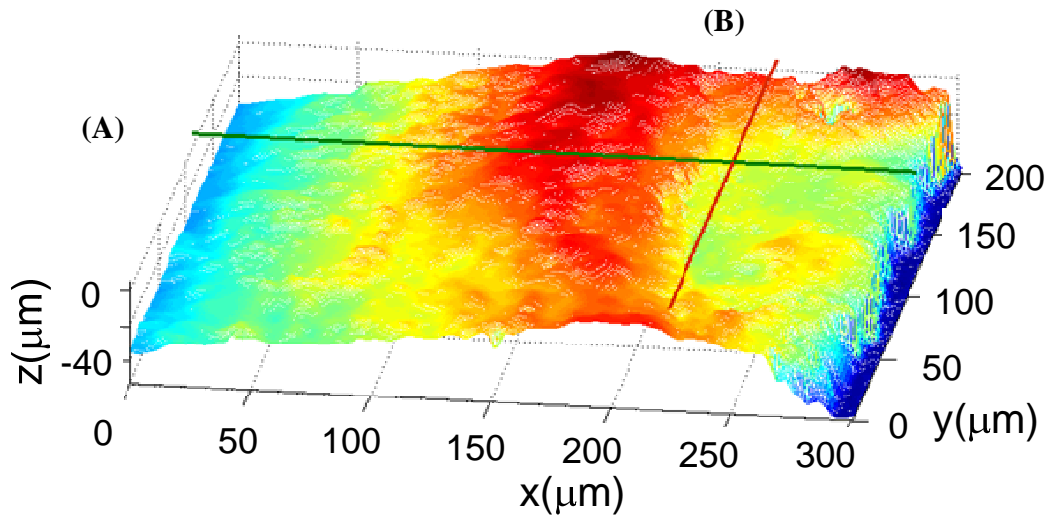


(d) 3D profile after etching
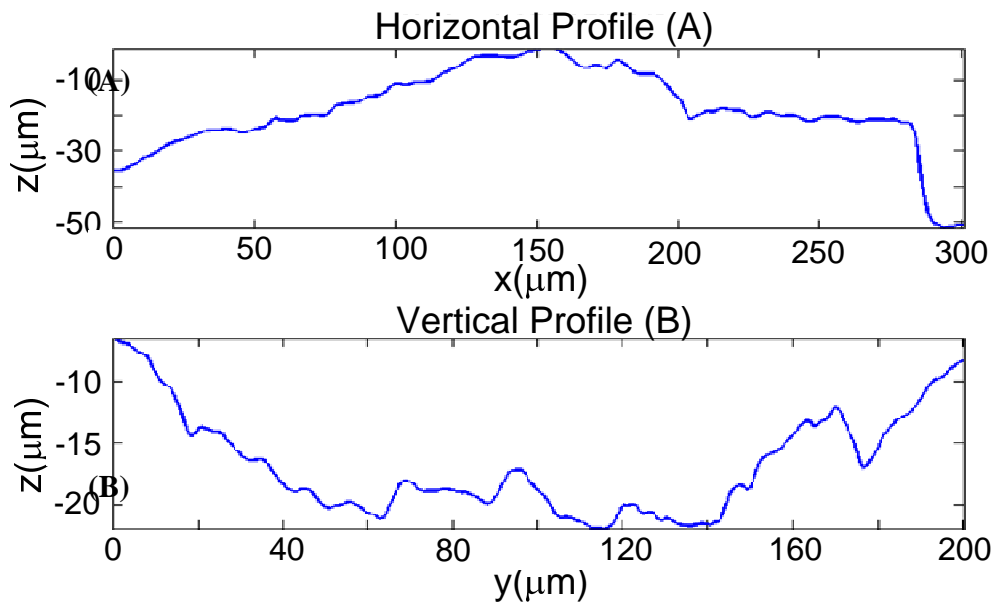


(e) Cross-sections of the 3D profiles

Figure 41 shows the CLSM images and tool wear profiles of the cutting edge where micro-fracture was not observed. Less Ti adhesion was observed on the PCD drill compared to the WC drill. As shown in Figure 41 (d), both flank wear and edge wear were observed on the

PCD tool, similar to the WC tools. When comparing the two tools materials at low speed, the PCD tool exhibits better resistance to flank wear (Figure 41). Due to the superior hardness of PCD compared with carbon fibers, tool wear should be much smaller during drilling of CFRP. Figure 42 presents that the edge wear of PCD is only one third of that of the WC but flank wear length for PCD is a half of that for WC. This supports an advantage that PCD drill shows superior performance in cutting CFRP.
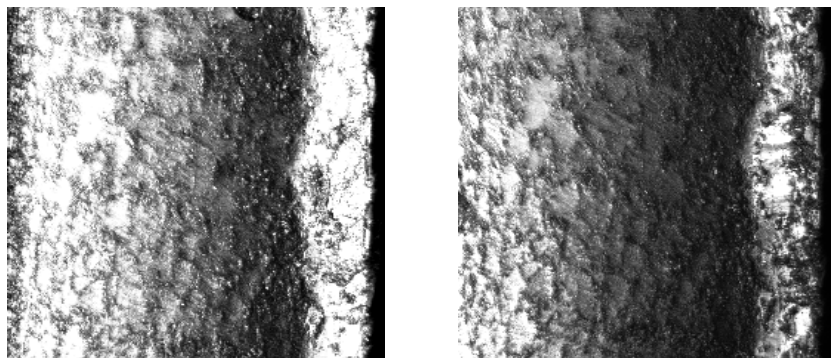


(a) HE Image before etching (50X)        (b) HE Image after etching (50X)
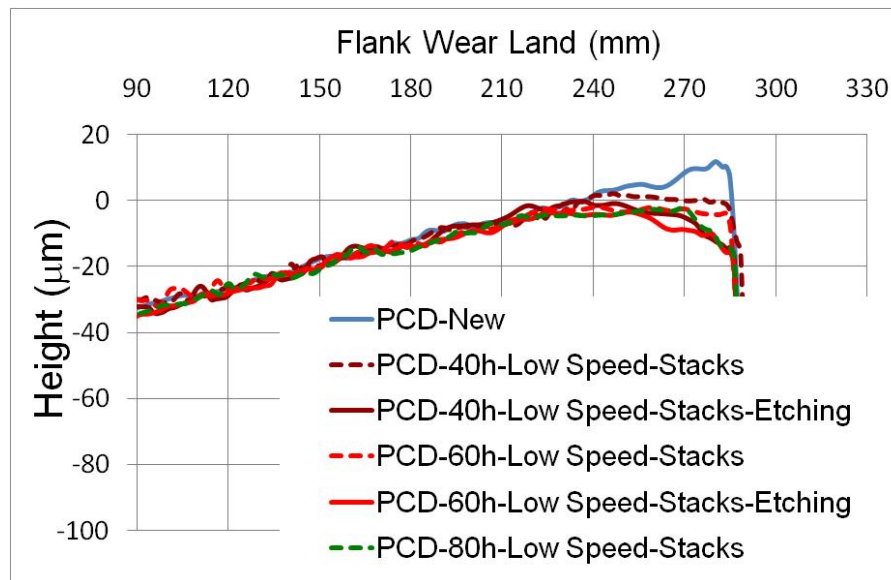


(c) 2D cross-sectional profiles

**Figure 41 CLSM images and flank wear profiles of PCD drill before and after etching at low cutting speed**
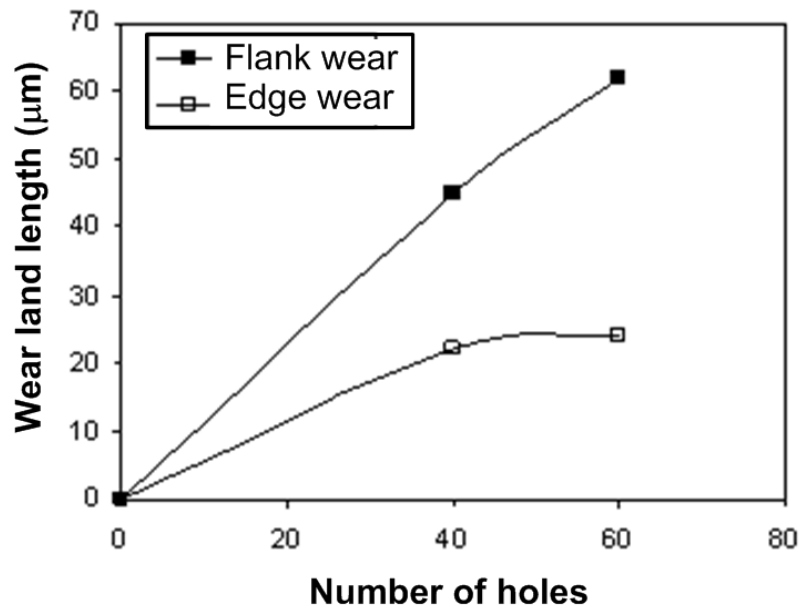
**Figure 42 Flank and edge wear progression of the PCD drill in low speed**

In summary, the PCD drill may have minimal tool wear when cutting the top CFRP plate due to its high hardness. As the drill penetrates the bottom Ti plate, micro-fracture occurs at the outer edges due to brittleness of PCD. In addition, mild Ti adhesion will take place on the cutting edges. When the PCD drill penetrates the CFRP plate again, carbon fibers abrade Ti adhesion away. However, Ti adhered at the cutting lips again and micro-fracture may be enlarged when penetrating the bottom Ti plate.

**4.4 CONCLUSIONS**

Tool wear analysis on uncoated WC and PCD drills was conducted in drilling of CFRP/Ti stacks using various microscopic instruments. The conclusion can be drawn as follows:

- As the number of holes drilled increase, the drilling forces of both WC and PCD drills gradually increase in both CFRP and Ti due to tool wear. The drilling forces produced by WC drill at high speed increased much faster than those at low speed. For the PCD drill, the drilling forces did not increase as significantly over the hole number.

- More adhesion of Ti was observed on WC drills than PCD drill. This adhesion was removed by carbon fibers in drilling of CFRP. No significant micro-chipping occurred on WC cutting edge tool but micro-chipping occurred on outer corner edge. For the WC drills, the wear pattern is generally smooth and uniform along the cutting edges. The flank wear was dominant at high cutting speed due to high cutting temperature in Ti drilling while the edge wear and flank wear showed similar amount of wear length at low cutting speed.

- Micro-chipping or micro-fracture was observed on PCD tool, in particular at the outer corner edge. The PCD drill showed small Ti adhesion in Ti drilling and exhibited high wear resistance in drilling of CFRP. Overall, the PCD was superior to WC tool in stack drilling. However, major chipping was observed at the cutting edge when drilling Ti due to the brittleness nature of PCD drills.

- In CFRP/Ti stack drilling, different wear mechanisms for CFRP and Ti alloy took place. Hard carbide fibers abraded more on cutting edge, which caused edge wear while hard phase in Ti extended the flank wear land in addition to carbide grain pullout when Ti adhesion was removed.

Chapter 5

**A STUDY ON DROPLETS AND THEIR DISTRIBUTION FOR MINIMUM QUANTITY LUBRICATION (MQL)**

In modern metal cutting applications, the cutting temperatures and forces on a cutting tool are typically high, which drastically reduces tool life. For this reason, the cutting zone must be well lubricated and adequately cooled by applying coolants in most machining applications. For optimal machining operations, the coolants must be maintained throughout their usage and eventually disposed. Recently, minimum quantity lubrication (MQL) or near dry machining (NDM) has been applied to reduce the cost associated with the maintenance and disposal of the sheer volume of fluid being used and the conformation to environmental policies [Weinert et al., 2004, Ueda et al., 2006 and Rahman et al., 2002]. In MQL, the high pressurized air sprays micro-scale lubricant droplets onto the tool-work interface. Even though it is very promising for many machining applications [Rahman et al., 2002, Varadarajan et al., 2002 and Sharma et al., 2009], several fundamental issues associated with MQL such as optimal conditions for the operations and environmental concerns have not been fully addressed [Park et al., 2008].

Typical oil-based lubricants used in MQL do not have the heat capacity of water-based coolants. Accordingly, the most important function provided by the lubricants in MQL is to reduce the friction between tool and work material. Thus, the most important point in the MQL process is that the lubricant must adequately cover the contact areas, i.e., tool-chip and tool-work interfaces. Particularly, droplet size and distribution in terms of nozzle distance and air pressure have to be considered because the smaller droplet, which can provide better penetration into the cutting surface, are more preferable especially for micro machining applications where the cutting surface is relatively small [Jun et al., 2008]. In addition, droplet distribution, which associated with the wetting area by lubricant, can affect the cutting performance as well. Other

98

important variables are wettability on the tool surface [Park et al., 2008] and thermal-chemical stability of lubricant. For example, vegetable oil shows poor the stability against oxidation and thermal degradation while mineral oil has important health related issues as discuss later. In this regards, several works have been reported not only for improvement of the thermal-chemical stability by additives or chemical modification of the vegetable oil but for optimal lubricants in MQL application [Sharma et al., 2009, Fox and Stachowiak, 2007, Suda et al, 2002 and Itoigawa et al., 2006]. Thus far, the efforts for understanding of these MQL parameters have not been considerably made. Therefore, a better understanding of the MQL application conditions such as droplet size and distribution, air pressure, nozzle distance, and flow rate is needed prior to machining process in industrial applications.

The operator's health hazards have been a major concern whenever lubricants/coolants are used in machining operations. For instance, in flood cooling, the workers are exposed with a variety of respiratory disorders including occupational asthma, hypersensitive pneumonia and loss of lung function and skin disease such as irritation, oil acne and skin cancer [Raynor et al., 2005]. The major industrial concern for MQL is the use of very fine, airborne fluid droplets which potentially pose a potential health risk for machine operators. This can be circumvented by installing the vacuum system in tandem with the MQL sprayer. However, the extent of health hazards depends on the concentration and the type of lubrication fluid used (mineral, vegetable or animal, water soluble and semi- or synthetic) as well as the duration of exposure. The characteristics such as mist droplets diameter and mass concentration generated are varied depending on the type of oils [Thornburg and Lieth, 2000]. Mineral oil may cause more serious damage to human body than vegetable oil. Mineral (petroleum- based) oil is retained in the lung and caused lung fibroses while vegetable oil is eliminated from the lung within a few days

without any obvious damage to the lung [Pinkerton, 1928 and Shoskes et al.,1950]. With the droplet (mist) size less than 4μm, even MQL can cause various occupational diseases. In fact it was reported to deteriorate lung function even for short-term exposure [Thornburg and Lieth, 2000]. Therefore, the national institute for occupational safety and health (NIOSH) has recommended that the exposure to metal working fluid mist is limited to $0.5mg/m^3$ for total particulate mass as the recommended exposure limit (REL) [NIOSH]. Thus, a great interest exists in the machining community in the development of a convenient technique to measure the droplet sizes in terms of lubricant types and spray conditions.

In this chapter, we have developed a new technique to measure the droplet sizes in a typical MQL process and their distribution after the droplets have been sprayed onto the polished silicon wafer surface. CLSM has been utilized for three-dimensional (3D) surface characterization of the droplet surface for the droplet volume measurement. The raw data from

To address various issues mentioned above, confocal laser scanning microscopy (CLSM) is used for the first time for this purpose. CLSM is an established advanced microscopy technique used in a variety of fields to obtain accurate surface topography [Hanlon et al., 2001]. In particular, CLSM can be successfully applied to characterize the crater wear of cutting tools [Olortegui-Yume and Kwon, 2007]. Wavelet transform can be useful when the dynamic or localized properties of surfaces are needed as opposed to the fixed wavelength harmonics assumed by classical fourier transform (FT) or gabor transform [Maksumov et al., 2004 and Rioul and Vetterli, 1991]. When wavelets are applied in cascade to the surface data, a multi-resolution representation of the surface can be obtained, i.e. surface representations at multiple scales [Fu et al., 2003]. The availability of the wavelet representations facilitates the researcher to perform tasks such as data de-nosing and identification of roughness features.

CLSM contains noise and artifacts due to the inherent nature of data acquisition process. To circumvent these problems, wavelets analysis has been applied by the use of de-noising schemes and multi-resolution decomposition which helps to extract the droplet profile. In addition, edge detection algorithm has been used to estimate the droplet volume for the calculation of the diameter in an airborne droplet. These developments have been used to study the effects of air pressure on the droplet size and distribution.

## 5.1 EXPERIMENTAL SETUP

Sharnoa SVC-60 CNC milling machine was used to provide the movement for the silicon wafer mounted on the CNC table while the MQL dispensing unit (Unimax-Part No. 9570-7-5-12- UNIST) equipped with a flexible nozzle was used to spray vegetable oil-based lubricant (UNIST-Coolube 2210). The MQL droplets were sprayed onto a silicon wafer to minimize the surface roughness in order to accommodate the task of extracting the droplet shape in the wavelets analysis. The set up for MQL spray experiment is shown in Figure 43. The droplets discharged from the nozzle with the flow rate of 3.2ml/min, which was measured by detecting the loss in the oil height though a graduated thin glass cylinder, are passed through the screening plate with a hole in order to block most of the oil mist stream and thus avoid droplet overlap on the wafer. After trying various hole diameters, it was set at 0.8mm because the droplet size did not decrease any further below this value. The droplets were discharged as a function of air pressure, P, and nozzle distance, D, in order to investigate their influence over the droplet size and distribution. To evaluate the effect of air pressure, mass accumulation test was developed, where an absorbent sheet placed on a wax paper was placed on the polished silicon wafer. With the mass accumulation test, the oil droplets that are eventually attached to the silicon wafer can

be distinguished from the airborne droplets. This test was performed in terms of air pressure and nozzle distance. Similarly, the sprayed droplets from the nozzle were absorbed into the mass measuring paper at the pressure of 4 and 8psi at the flow rate of 3.2 ml/min.

- Air Pressure, P
- Nozzle Distance, D
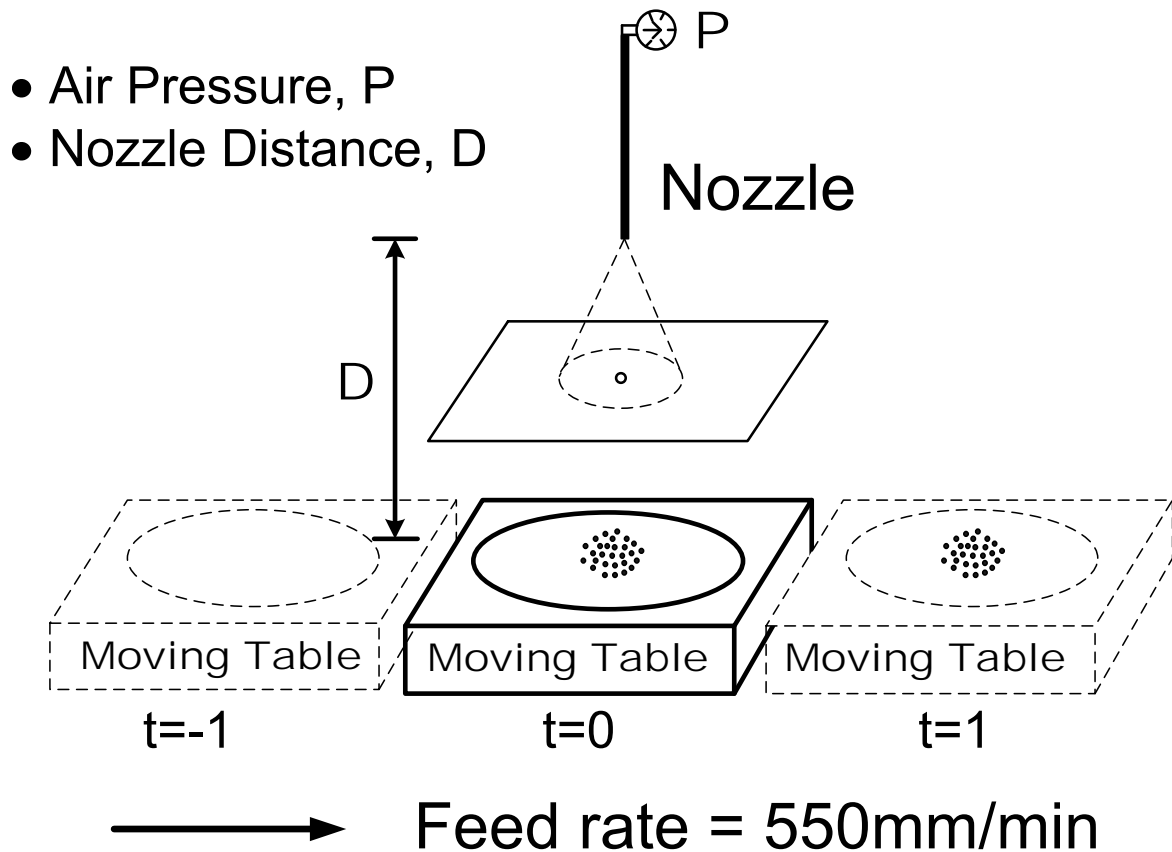
**Figure 43 MQL Experimental Set-up**

## 5.2 CLSM DATA ACQUISITION AND IMAGE PROCESSING

The important characteristic of CLSM is the confocal aperture which eliminates the reflected light from above and below the focal plane, thus obtaining surface information from a very thin "optical slice" of the surface is feasible. Surface reconstruction is achieved by storing and manipulating a stack of optical slices within a set of the vertical travel of the stage. The final output of the built-in software in CLSM is a z-matrix ($z(x,y)$) containing the height information of the surface. For a better handling of the image data, the z-matrix is encoded in a grayscale, called height encoded (HE) image. Along with HE images, maximum brightness (MB) images, which are extended depth of field views, can be also obtained. It is important to note that most confocal systems can work in both confocal and optical (conventional) modes. The detail information on CLSM can be found in [Hanlon et al., 2001 and Olortegui-Yume and Kwon, 2007]. In this work, A Zeiss LSM210 Confocal system was used to capture 2D images (confocal slices) and HE images (topography) of individual droplets using Plan Neofluar 5X/0.15 and 50X/0.80 objectives. Figure 44 (a and b) shows the 2D CLSM droplet images at 4psi and 8psi, respectively, obtained with the 5X/0.15 objective. These images are used for identifying the droplet size distribution and the droplet coverage area fraction deposited on the wafer. The boundaries of each droplet were detected using edge detection algorithm (EDA) called 'Canny' which looks for local maxima of the intensity gradient in an image. Then the areas enclosed by detected boundaries were filled and considered as the sprayed droplets as shown on Figure 44 (c and d). It was assumed that the areas smaller than 2 pixels (1 pixel=5.87265μm X 4.16792μm/5X objective) were rejected. On the other hand, for droplet size measurement, HE images were obtained for various sizes of individual droplets, as shown in Figure 45.

The main advantage of the wavelet transform for image processing is to extract the surface topography clearly from the raw image data without losing any surface details [Park and Kwon, 2009 and Olortegui-Yume and Kwon, 2010]. In this work, the two-Dimensional Discrete Wavelet Transform (2D-DWT) was used in a multi-resolution scheme with a two-channel filter bank, which consists of a pair of filters, low-pass and high pass filters based on a chosen mother wavelets, Daubechies7(db7) [Rioul and Vetterli, 1991]. For acquisition of the droplet topography (3D), the wavelet de-noising was required to eliminate the electronic noise and artifacts from individual droplet images (HE images). The de-noised surface topography data was then post-processed using multi-resolution wavelets analysis. Finally, the droplet size can be obtained by calculating the droplet volume (see Sec.5.3).
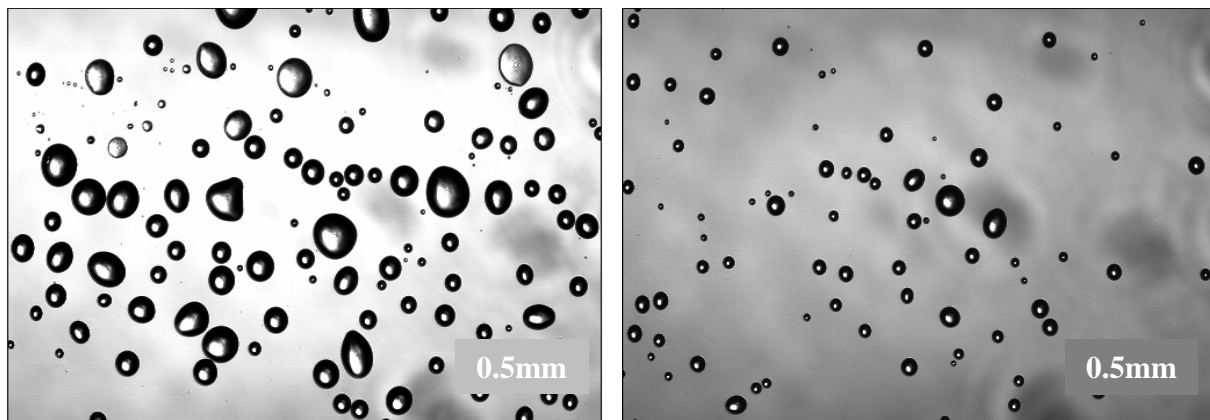


(a) Droplet distribution at 4psi          (b) Droplet distribution at 8psi

**Figure 44 Droplets distribution optical images from CLSM and bitmap images obtained by EDA at 4psi and 8psi**

**Figure 44 (cont'd)**
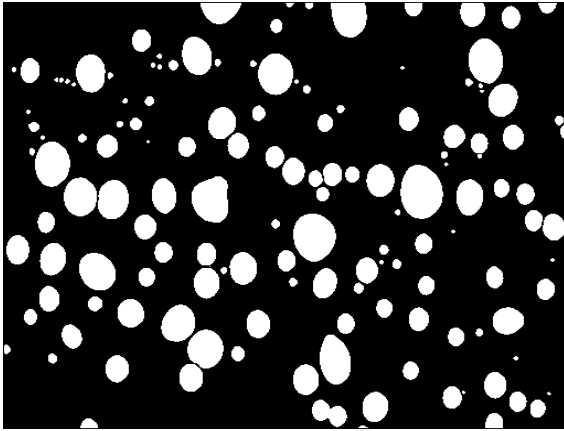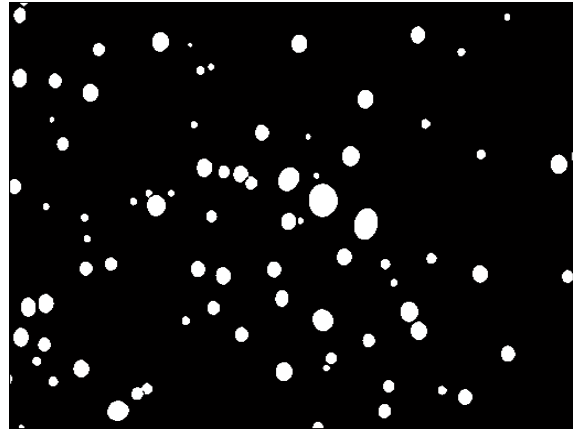


(c) Bitmap image for (a)                    (d) Bitmap image for (b)
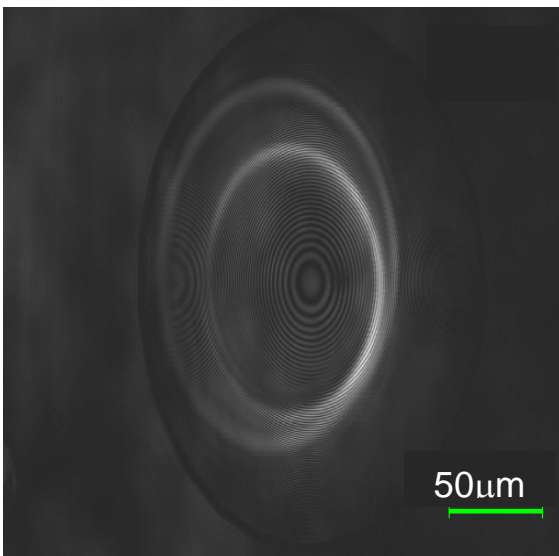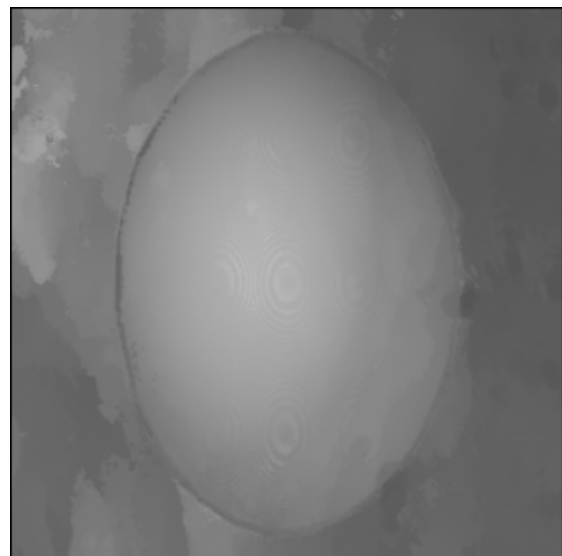


(a) 2D optical image                    (b) HE image of a droplet of (a)

**Figure 45 Droplet images for droplet size measurement**

## 5.3 DROPLET VOLUME CALCULATION

Once the droplets are deposited onto the flat silicon wafer surface, each droplet spreads and changes its morphology while preserving the volume of each droplet. Using the HE image information, the volume of droplet can be calculated as presented in Eq. (9).

$$V_{droplet} = \sum \Delta V_{i,j} = \sum_{i=1}^{M} \sum_{j=1}^{N} \Delta x \cdot \Delta y \cdot (h_{i,j} - h_{zero})$$

$$(9)$$

where $\Delta V_{i,j}$ is the discrete volume at a point $P_{i,j(x_i,y_j,z_{i,j})}$, $h_{i,j}$ is the surface height of droplet at a point $P_{i,j}$ and $h_{zero}$ is considered as the height of the droplet edge. The total volume of a droplet can be obtained by summing up the discrete volume, $\Delta V_{i,j}$. The height $z_{i,j}$ is obtained as a result of HE image decoding. $M$ and $N$ correspond to the size of the HE image. Once the droplet volume calculated, the diameter of a spherical airborne droplet, $D_{eq}$, can be defined as Eq. (10).

$$D_{eq} = 2 \times \left[ \frac{3 \cdot V_{droplet}}{4\pi} \right]^{1/3}$$

$$(10)$$

## 5.4 RESULTS AND DISCUSSION

### 5.4.1 Droplet size and distribution

Figure 46 (a) shows air pressure effect on the oil mass accumulation test. After the oil was sprayed in terms of the nozzle distance and air pressure, the oil mass accumulated on the absorbent paper was measured. The average mass accumulated decreased as the nozzle distance and the air pressure increased as shown in Figure 46 (a). Moreover, the oil mass could not be measured at a higher air pressure because the spray was too vigorous so that the oil mist cloud was generated in the air rather than accumulated on the absorbent paper. Thus, accurate data could not be obtained at higher air pressure. Based on mass accumulation test, the short nozzle distance is more preferable and too high air pressure might not wet the cutting surface effectively, especially with the increase in the nozzle distance if the small cutting zone is considered.

The 2D CLSM images of sprayed droplets obtained under various operating conditions (Figure 46 (b)) were converted into their bitmap versions (Figure 46 (c)), which were ultimately used to calculate the average dimensions of droplets as well as the area fraction covered by droplets. Table 11 summarizes the quantitative results of these calculations. It was observed that, as the nozzle distance increased, the surface covered by the droplets decreased. The spray conditions for the maximum surface coverage were observed at a nozzle distance of 30mm and 12psi nozzle pressure. This is because more droplets are released from the nozzle within a unit time and thus more of them can cross the screening plate at a higher air pressure. However, the area fraction decreased substantially at the nozzle pressure of 12psi as the nozzle distance increased. For example, as seen in Table 11, at the air pressure of 12psi, the covered area fraction dropped from 15.1% at the nozzle distance of 30mm to 1.7% at that of 70mm. The reduction of

the area fraction is more substantial at a higher air pressure. The droplet size at higher pressure is smaller than that of lower pressure.

Therefore, it can be concluded that the nozzle distance should be less than 50mm and if the high air pressure is required, the nozzle distance should be short enough to provide adequate lubricant at the cutting zone.
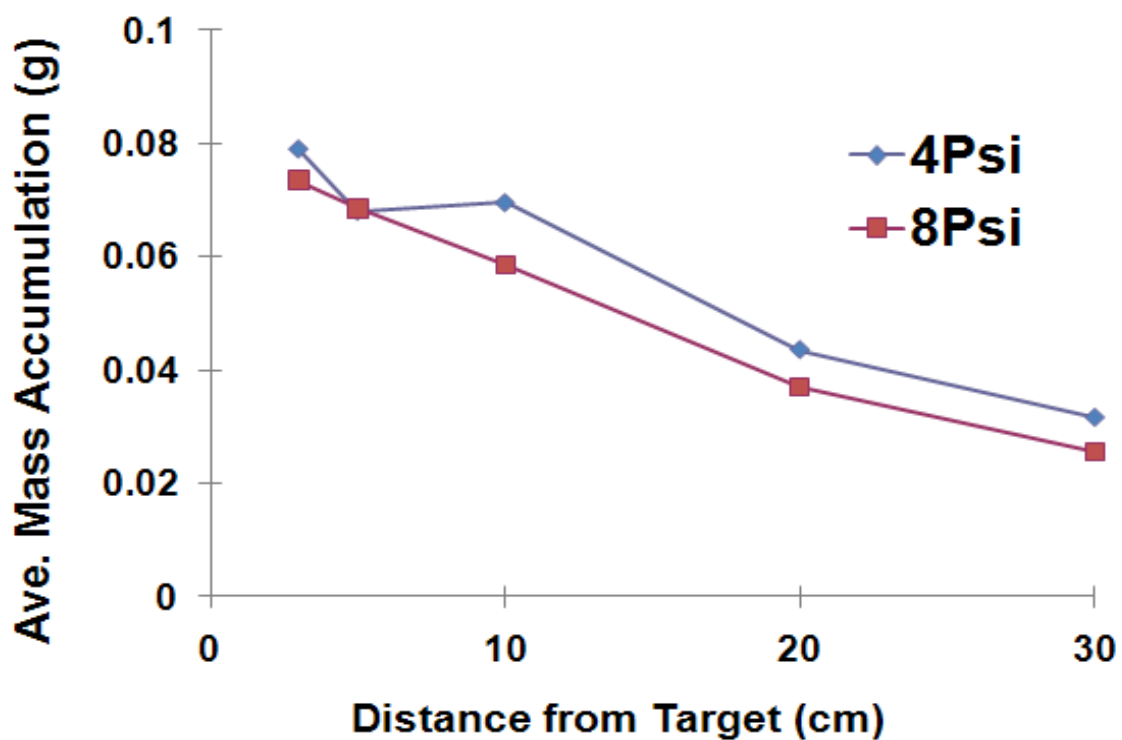


(a) Mass accumulation in terms of air pressure and nozzle distance
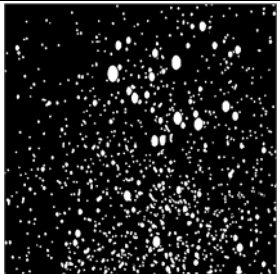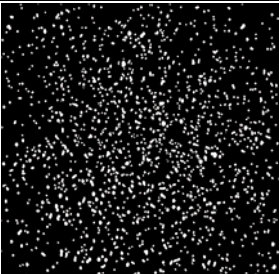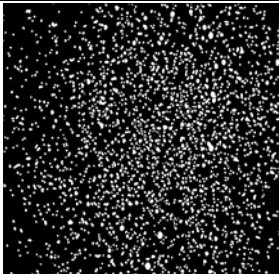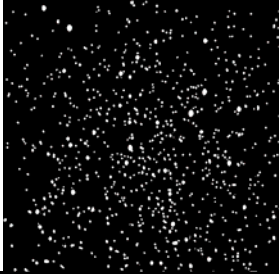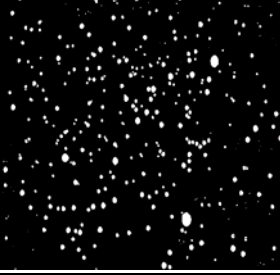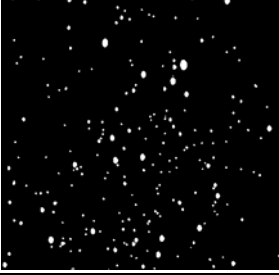
**Figure 46 Average mass accumulation, sprayed CLSM images, and corresponding bitmap images at nozzle distances and air pressures**

**Figure 46 (cont'd)**

| | 4 Psi | 8 Psi | 12 Psi |
|---|---|---|---|
| **30mm** | | | |
| **50mm** | | | |
| **70mm** | | | |
| **90mm** | | | |
| **110mm** | | | |
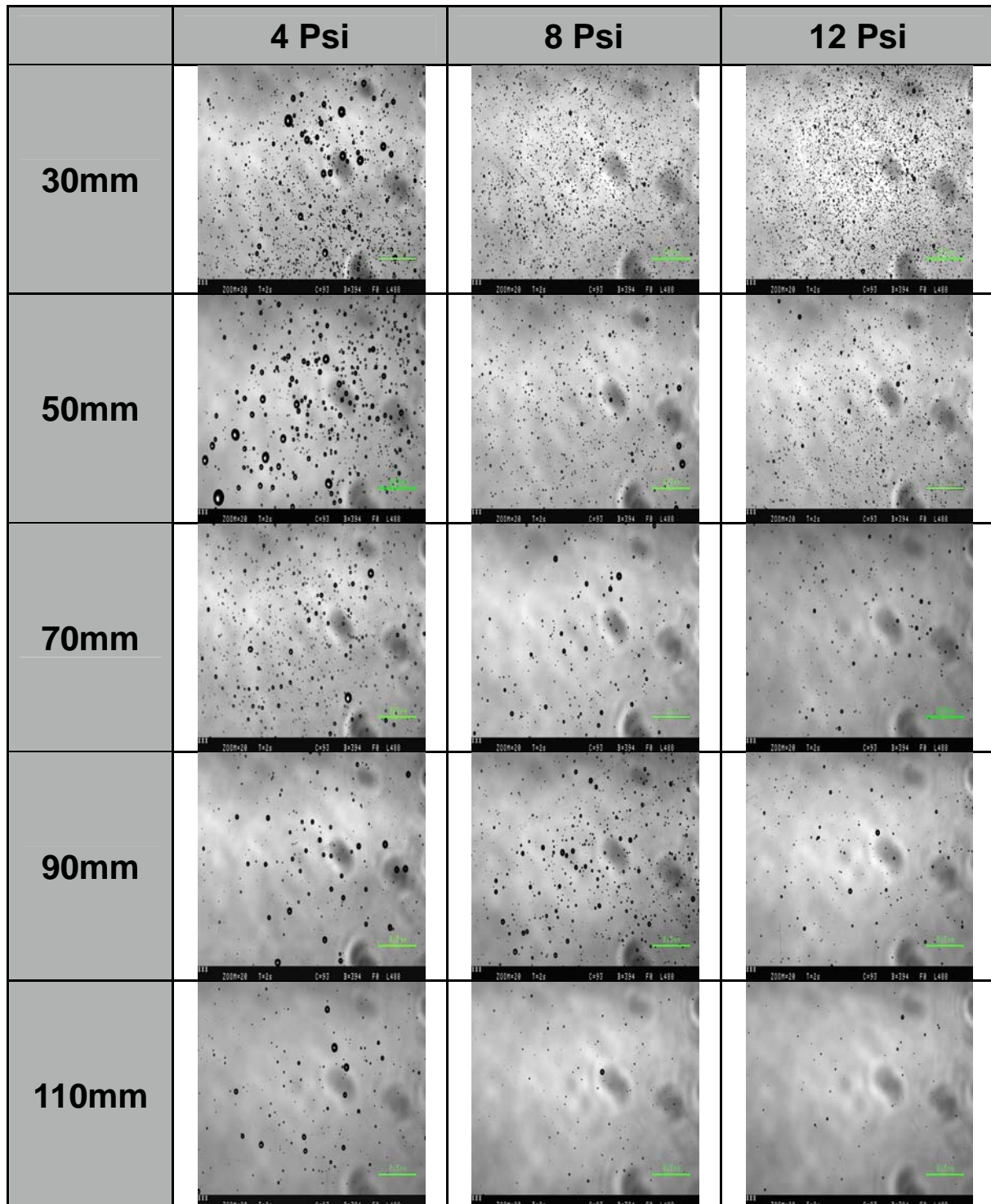
(b) The Tiff images from CLSM

**Figure 46 (cont'd)**

| | 4 Psi | 8 Psi | 12 Psi |
|---|---|---|---|
| **30mm** | | | |
| **50mm** | | | |
| **70mm** | | | |
| **90mm** | | | |
| **110mm** | | | |

(c) Bitmap images by EDA

**Table 11 Average sizes, droplet count, and area fractions**

| NOZZLE DISTANCE | NOZZLE AIR PRESSURE | | | | | | | | |
| | 4psi | | | 8psi | | | 12psi | | |
| | $D_{av}$ (μm) | $N_d$ | $A_f$ (%) | $D_{av}$ (μm) | $N_d$ | $A_f$ (%) | $D_{av}$ (μm) | $N_d$ | $A_f$ (%) |
|---|---|---|---|---|---|---|---|---|---|
| **30mm** | 12.93 | 888 | 9.3 | 11.28 | 1335 | 9.6 | 11.32 | 2066 | 15.1 |
| **50mm** | 15.18 | 595 | 8.9 | 12.66 | 471 | 4.5 | 10.54 | 797 | 5.0 |
| **70mm** | 13.94 | 362 | 4.5 | 12.29 | 217 | 2.0 | 11.85 | 217 | 1.7 |
| **90mm** | 15.47 | 151 | 2.4 | 11.05 | 485 | 3.4 | 11.70 | 160 | 1.2 |
| **110mm** | 13.32 | 144 | 1.6 | 11.04 | 71 | 0.5 | 10.15 | 58 | 0.3 |

$A_f$: Area fraction covered by droplets (%)

$N_d$: Droplet count

$D_{av}$: Average diameter (μm)

### 5.4.2 Droplet volume calculation by wavelet transform

The general procedure used to calculate the droplet size includes the CLSM data acquisition, the wavelets de-noising step, the wavelets multi-resolution analysis, and the droplet volume calculation as presented in Figure 47. In addition, an empirical model is developed to estimate the droplet diameters sprayed in the air based on the relationship between 2D CSLM images and 3D HE images (see Sec. 5.4.3).
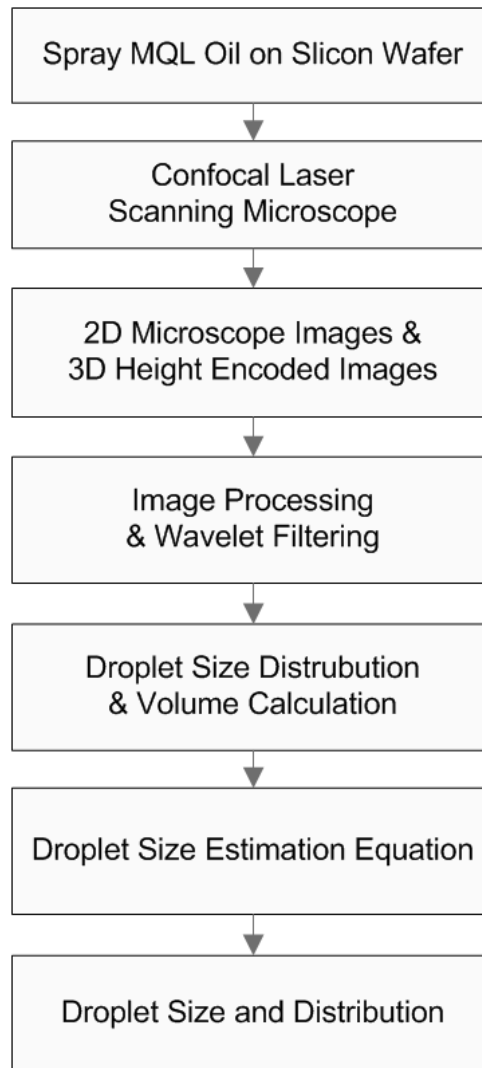
**Figure 47 Flow chart for the calculation of the droplet size and distribution**

Figure 48 (a) shows the raw HE image of an individual droplet obtained at the compress air pressure of 6 psi and the nozzle distance of 55mm using the 50X/0.80 objective in the CLSM. Each pixel size for the 50X objective is 0.14745μm×0.764706μm. In the HE image (Figure 48 (a)), the surface height at a position (x,y) is encoded such that the bright pixels indicate high positions relative to dark pixels. For more accurate calculation, only droplet surface area was cropped using image processing software as shown in Figure 48 (a). Figure 48 (b) shows the 3D

surface reconstruction of the droplet surface using the raw HE image in Figure 48 (a). The droplet HE image was post-processed using a wavelet-denoising algorithm (Daubechies) to filter out electronic noise and unusual pits/peaks (artifacts) present. This denoised HE image was used as an input for the multi-resolution analysis up to level 7 using Daubechies7 (db7) mother wavelet. After inspecting the decoupled approximation and detail surfaces, a threshold level was defined beyond which distortion impairs the useful extraction of the droplet shape. Raw HE images contain the topography of the surface mixed with noise and artifacts. However, even if all the noise and artifacts are eliminated, the remaining information in the HE images could contain the tilting of the silicon wafer stages and of the substrates (wafers in this case). Extracting the droplet shape from a tilted surface is considerably difficult; thus, tilting was compensated using mean slope obtained by the average of the slopes in both x and y directions both tilted shapes are shown in Figure 48 (b) and (c). The slope compensation is carried out after wavelet multi-resolution analysis and prior to the droplet volume calculation.
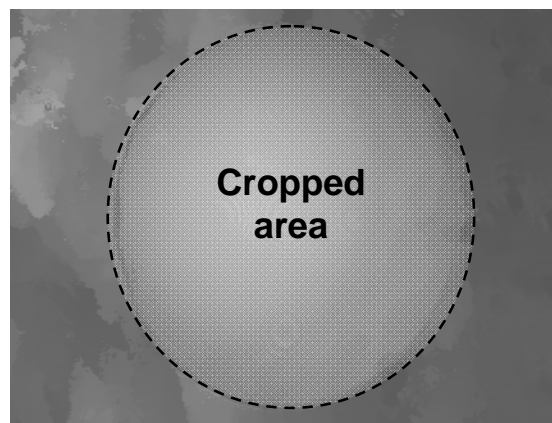


(a) HE image of a droplet

**Figure 48 HE image of the droplet (a), 3D surface profile (b) and 2D droplet profiles in x (c) and y section (d) at level 3**

**Figure 48 (cont'd)**
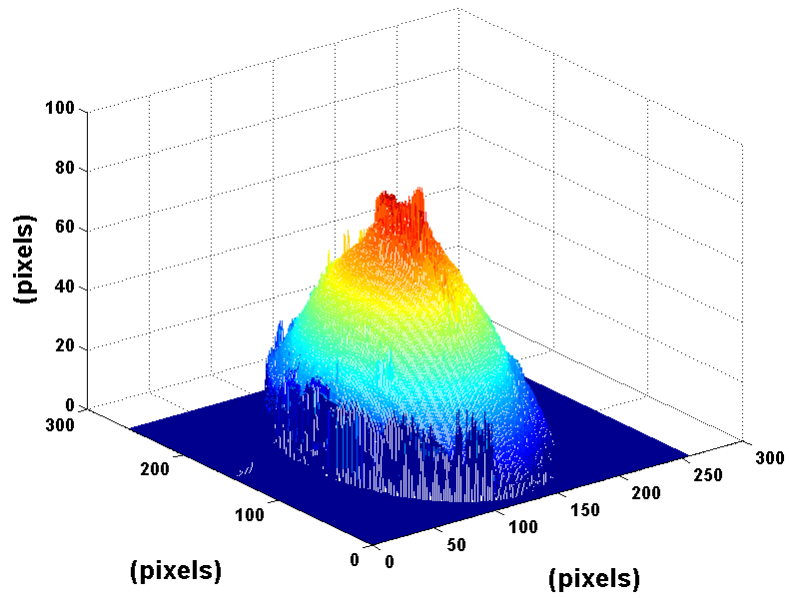


(b) Droplet surface topography from (a)
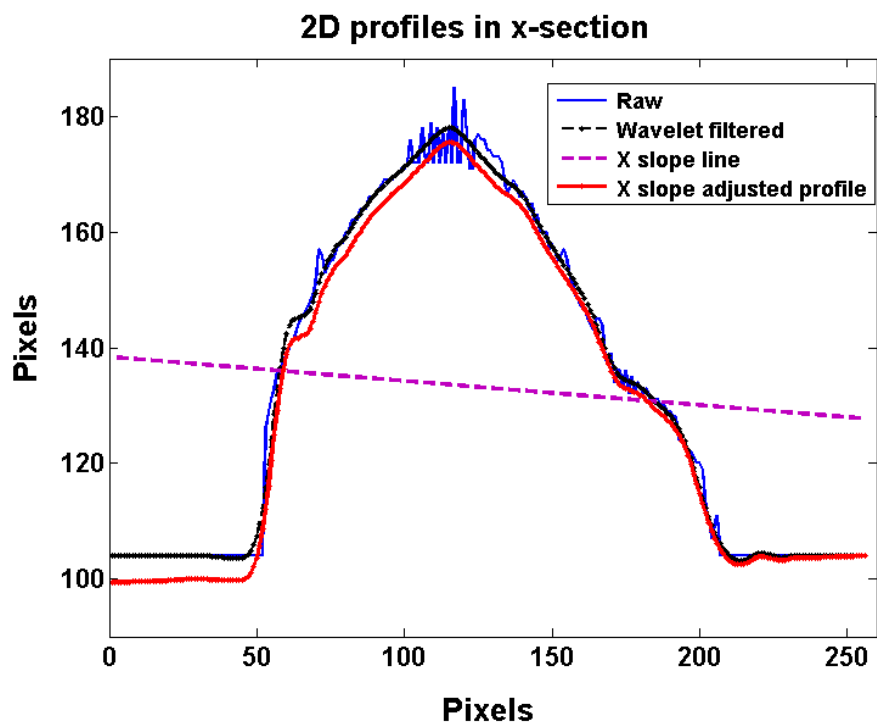


(c) Droplet surface profiles in x - section

**Figure 48 (cont'd)**
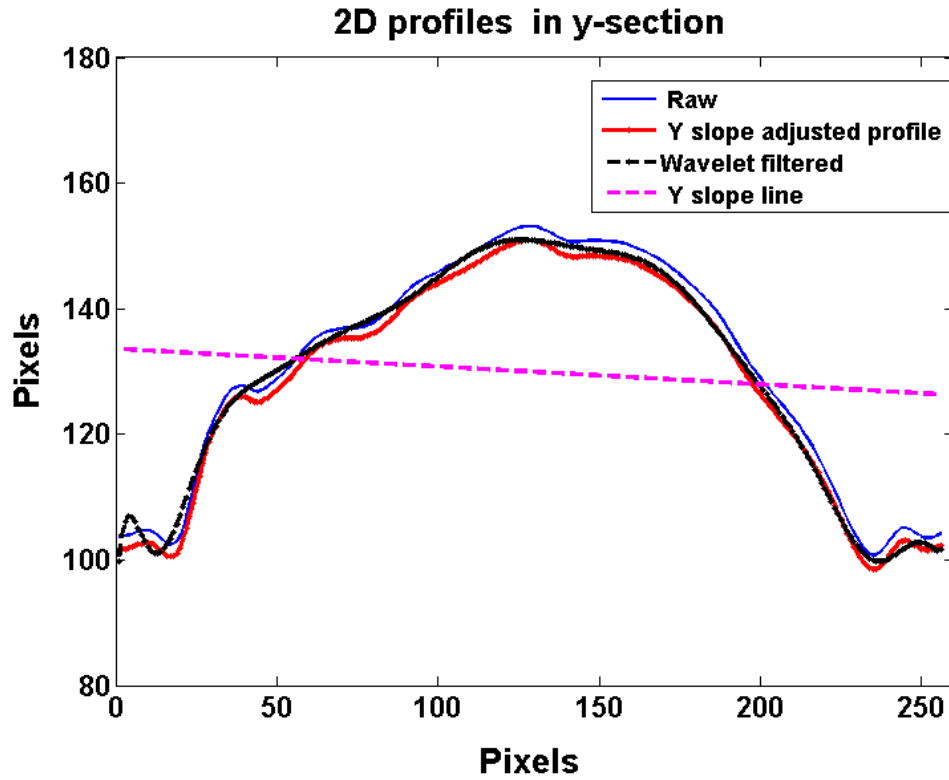


(d) Droplet surface profiles in y - section

Figure 49 presents the approximations and details surfaces (horizontal, vertical and

diagonal) obtained up to $7^{th}$ level after applying the wavelet transformation including the

reconstruction (inverse transformation) process. It can be clearly observed that between levels 1

through 4 (Figure 49 (b)) the decoupling of the droplet (large features) from the details (small

features) is consistent with our purpose. In other words, the approximation surface contains

mainly the dominant shape (the droplet) while the detail surfaces contain much smaller features.

In this study, only the approximations were used for the droplet profiles and volume calculations

since the small features such as roughness and waviness were of no interest. After the $4^{th}$ level of

decomposition, this behavior is no longer observed and between levels $5^{th}$ and $7^{th}$ larger features are being extracted implying a major distortion in the droplet shape.

Figure 50 shows the approximation droplet surfaces for all levels up to the $6^{th}$ level of wavelet decomposition. It is clearly observed that the fourth level is the threshold limiting the feasible extraction of the droplet shape. Thus, the images between $1^{st}$ and $4^{th}$ levels with the droplet pattern clearly were used for the volume calculation.



(a) $1^{st}$ level
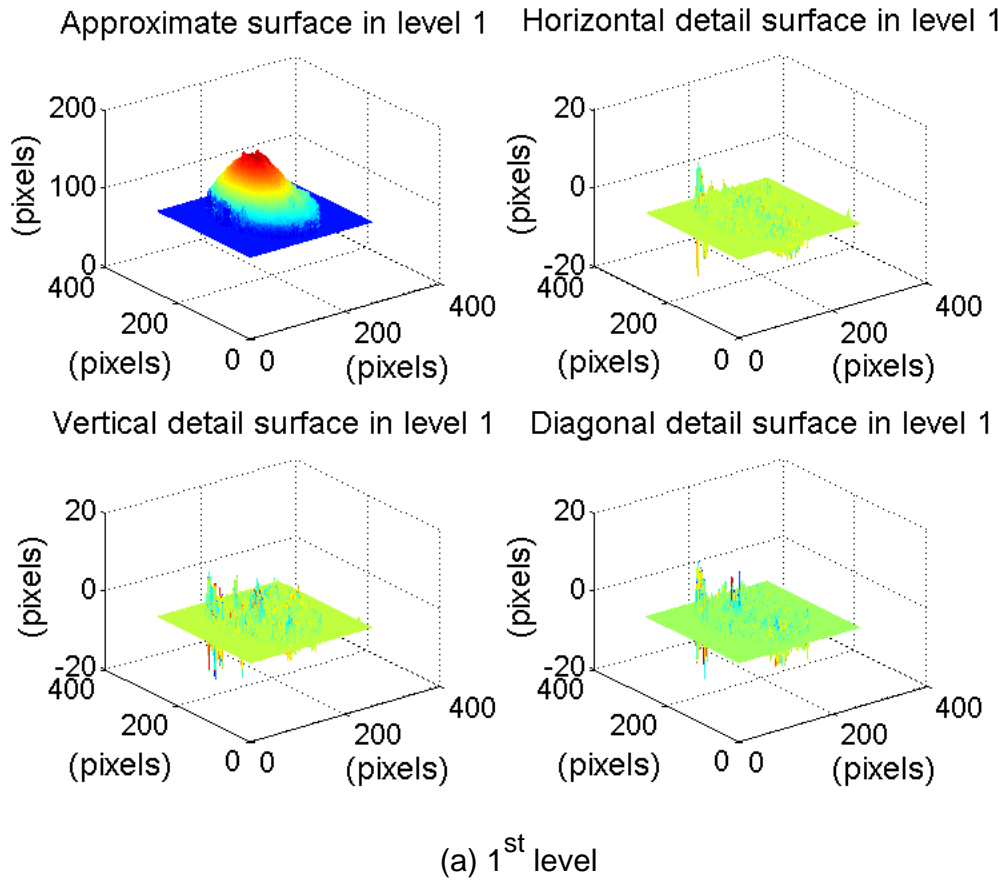
**Figure 49 The Droplet surfaces after wavelet filtering**

**Figure 49 (cont'd)**

Approximate surface in level 4    Horizontal detail surface in level 4
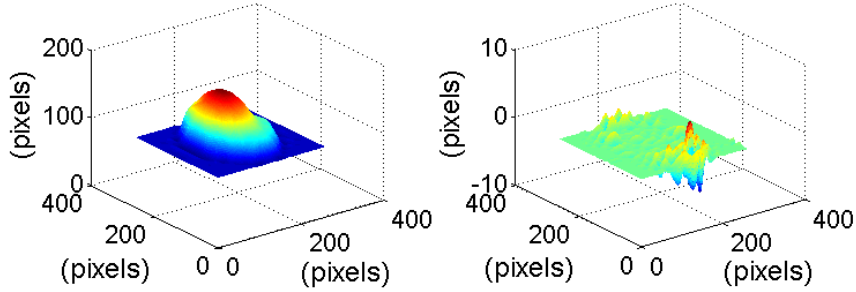
Vertical detail surface in level 4    Diagonal detail surface in level 4
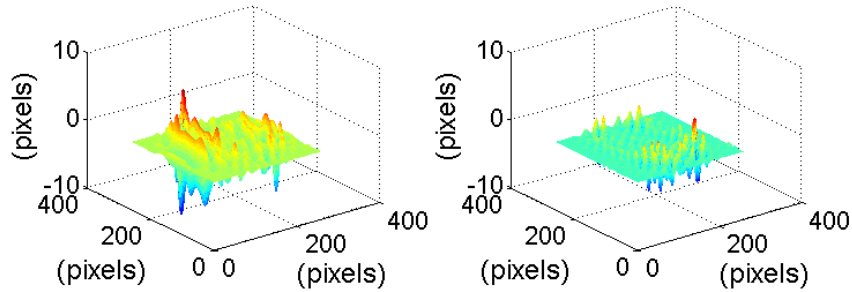
(b) 4<sup>th</sup> level

Approximate surface in level 5    Horizontal detail surface in level 5
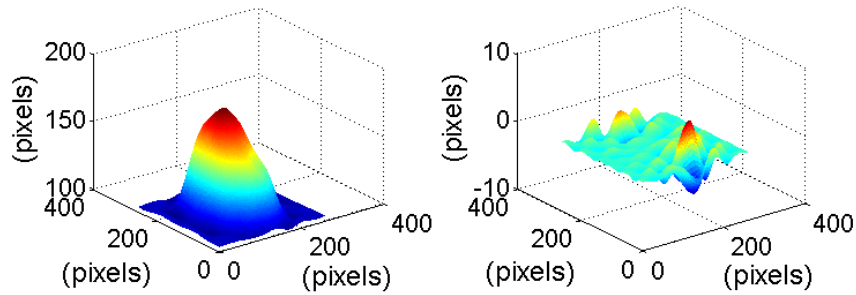
Vertical detail surface in level 5    Diagonal detail surface in level 5
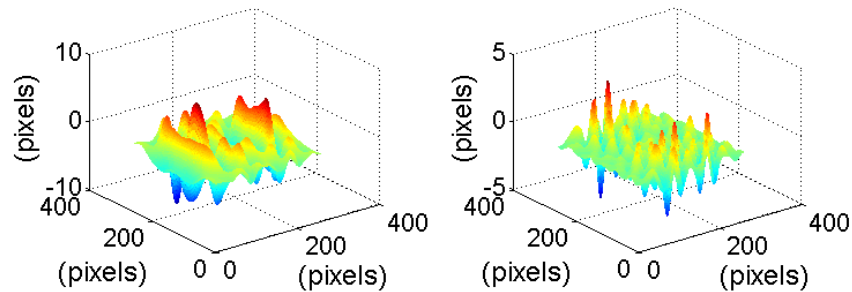
(c) 5<sup>th</sup> level

**Figure 49 (cont'd)**

Approximate surface in level 7    Horizontal detail surface in level 7

Vertical detail surface in level 7    Diagonal detail surface in level 7

(d) 7$^{th}$ level
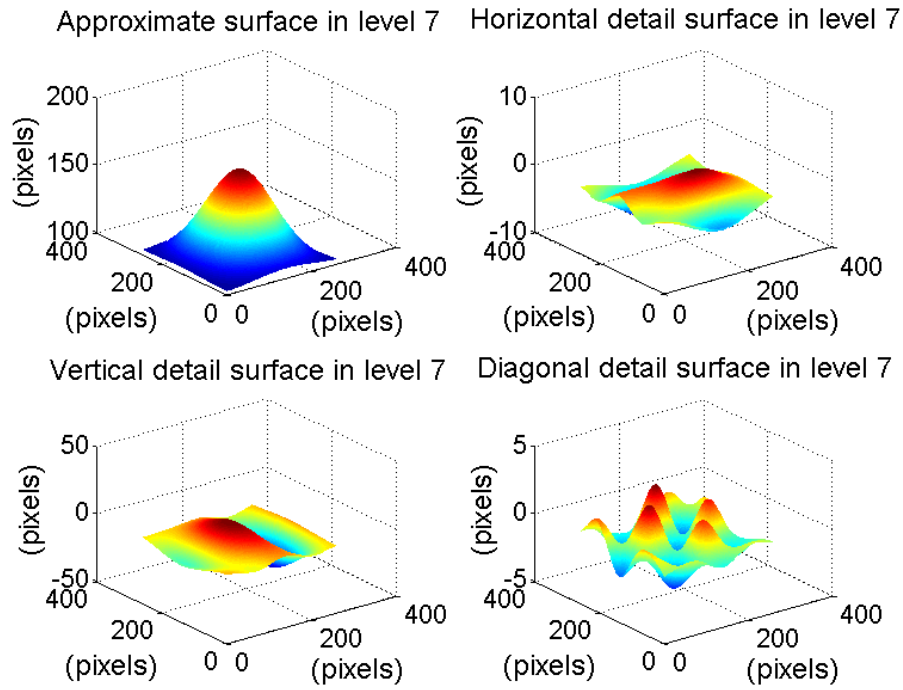
(a) 1$^{st}$ level                        (b) 2$^{nd}$ level
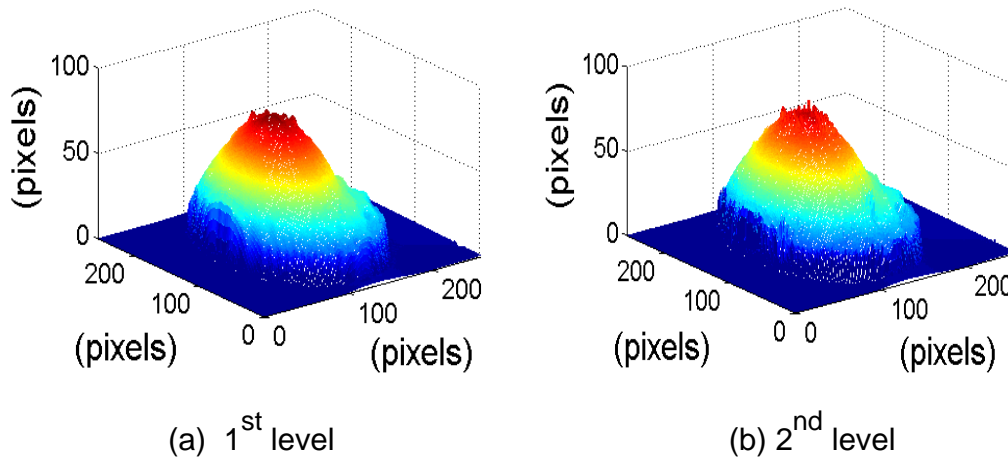
**Figure 50 Droplet surface after wavelet transform in 1$^{st}$ to 6$^{th}$ level**

**Figure 50 (cont'd)**



(c) 3$^{rd}$ level

(d) 4$^{th}$ level



(e) 5$^{th}$ level

(f) 6$^{th}$ level
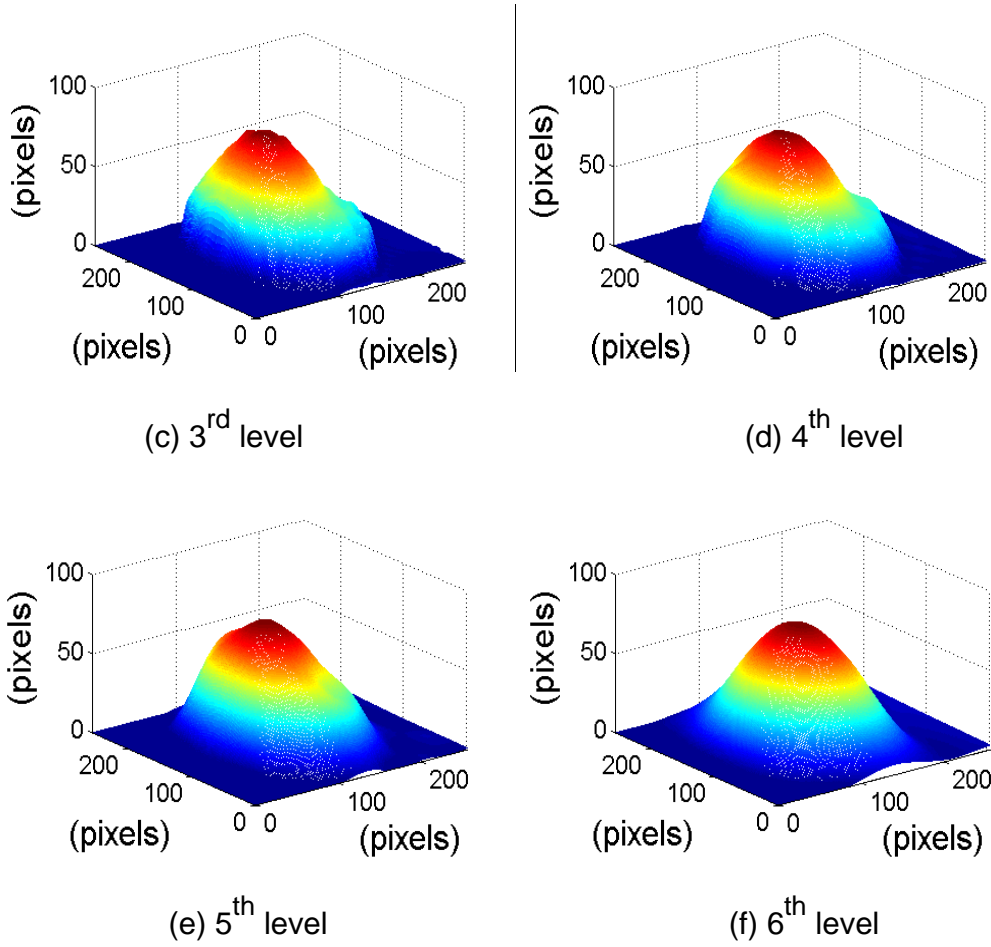
Using the droplet surface of Figure 50 (c), the estimation of droplet volume was conducted. The total calculated droplet volume using Eq. (1) at level 3 is 2.1084E-004mm$^3$. The droplet volume calculated in each level can be shown as in Figure 51 (b). The calculated droplet volumes from 1$^{st}$ to 7$^{th}$ level of wavelet decomposition are similar, but it shows a large deviation above 7$^{th}$ level. With this droplet volume calculation technique, further analysis with other droplet details such as wetting angle and average droplet size, can be conducted for various commercial lubricants. In this sense, the equivalent droplet radius is estimated at level 3 as 36.92

μm using Eq. (2) and the equivalent droplet radius in several levels can be shown as Figure 51

(c). It shows the similar trend with droplet volume at each level. As shown in Figs. 51 (b) and (c),

the droplet surface profiles were completely lost at $8^{th}$ level.
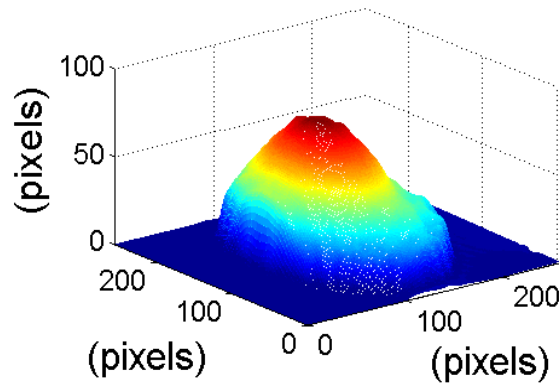


(a) Final droplet surface
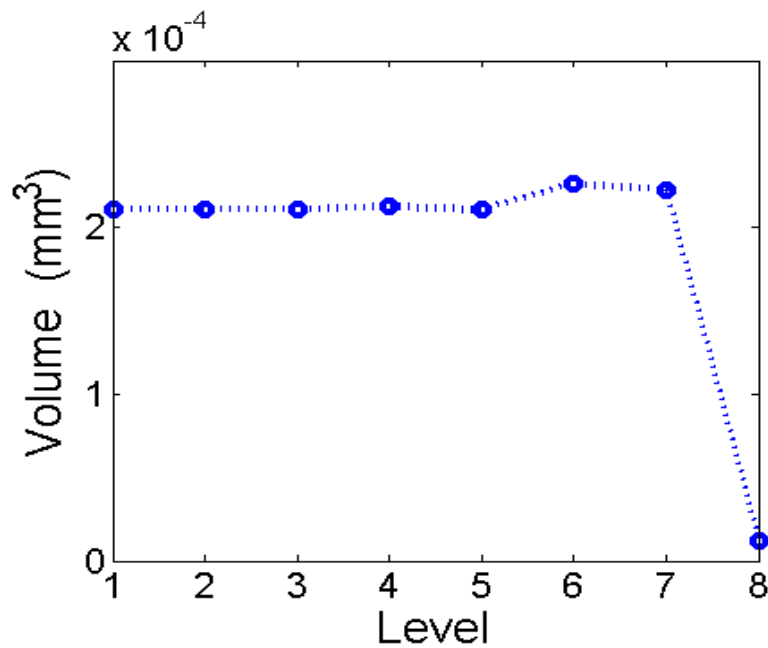


(b) Estimated volume

**Figure 51 Droplet surface at level 3 (a) and its corresponding estimated droplet volume (b) and equivalent radius (c)**

**Figure 51 (cont'd)**
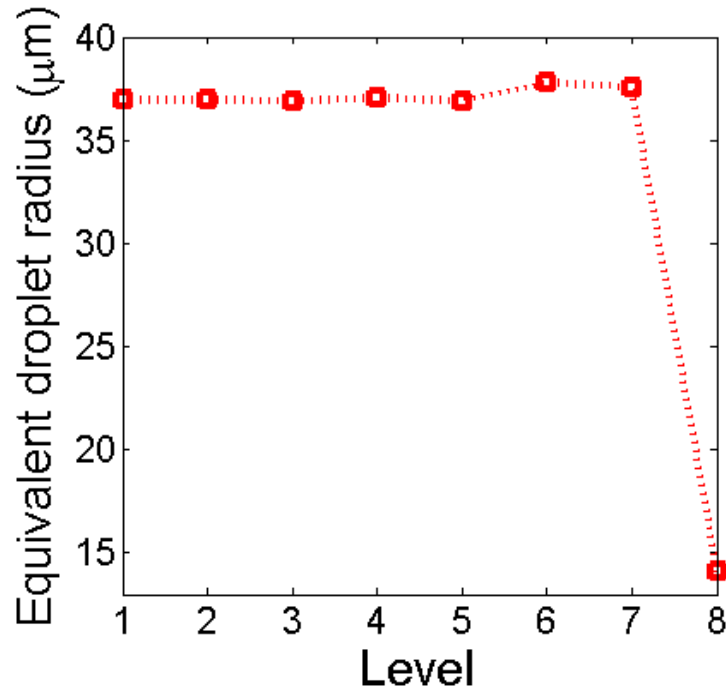


(c) Equivalent radius

### 5.4.3 Small droplet size estimation

The capturing of HE images (3D data) for very small droplets with the average diameter, $D_{av}<100\mu m$, can be challenging and time consuming. Thus, an estimation method was pursued. A diameter estimation equation for a spherical airborne droplet (3D) can be achieved by using the CLSM optical image (2D version) and the calculated volume of a droplet (3D). For example, both the optical and HE images for the droplets are taken by CLSM. Using volume calculation method in Sec. 5.3 and Eq. (2), 3D diameters of airborne droplets can be obtained. Figure 52 (b) and (d) represent the droplet volumes calculated by wavelet-filtering for different droplet sizes and Figure 52 (a) and (c) are their corresponding 2D droplet images, respectively. In addition, for

the small droplet estimation, relationship between 2D and 3D droplet diameters was determined by using interpolation method as in Eq. (11).

$$D_{3D} = 0.0012 D_{2D}^{2} + 0.1997 D_{2D} - 0.0987 \qquad (11)$$

where $D_{2D}$ is the 2D diameter of a droplet on the silicon wafer and $D_{3D}$ is the diameter of an airborne droplet. This empirical correlation between the diameters in the 2D images and the diameters in the 3D data (HE images) should be limited to the combination of the lubricant and the silicon wafer surface used in this study. To justify the use of this equation, other combination of lubricant and surface need to be studied. Finally, 2D and 3D droplet diameters for various sizes of the droplets for the vegetable oil can be obtained as summarized in Table 12. Finally, without measuring the extremely small droplets, the size of oil droplet sphere sprayed from the nozzle can be estimated. Using Eq. (3), the size distribution of droplets in Figure 45 (a), 2D images, was analyzed and the average 3D droplet size was around 10μm. Besides, the most of the droplet sizes in this test is less than 20μm, which might be small enough to be effective in practical MQL application, as shown in Table 13. The proposed method of measuring the droplet size is particularly useful to evaluate the very small droplet sizes if the inhaling of MQL droplets by operators is harmful.
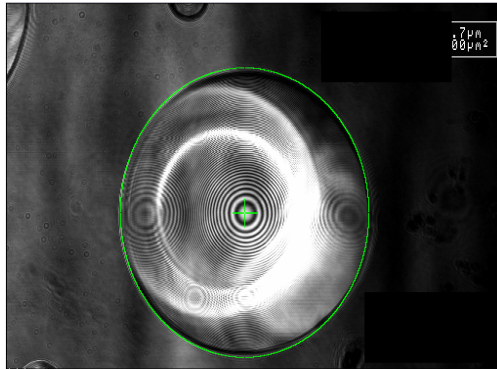
(a) 2D diameter (149.7μm)
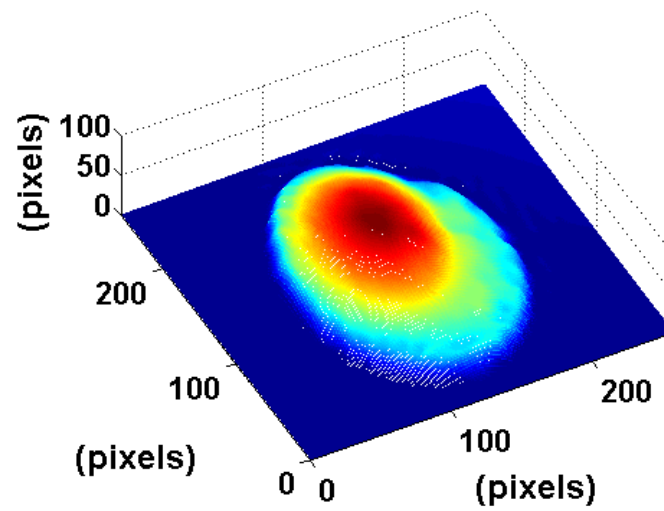


(b) Droplet volume (9.2337E-005mm$^3$)
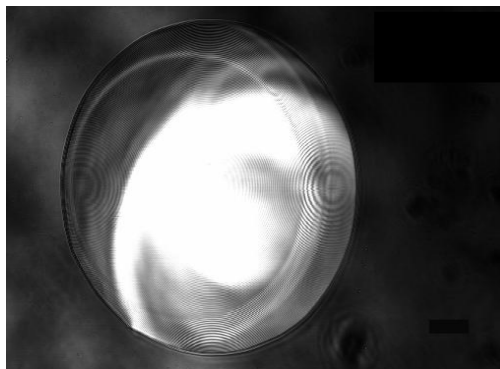


(c) 2D diameter (173.4μm)

**Figure 52 Droplet volumes corresponding 2D droplet sizes**

**Figure 52 (cont'd)**
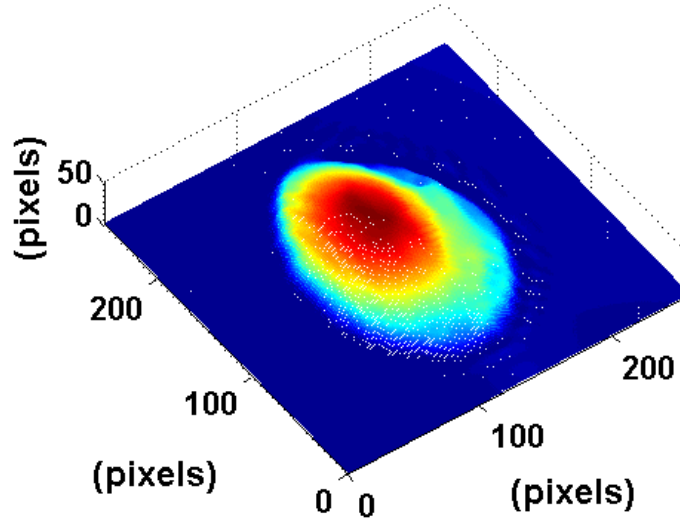


(d) Droplet volume (1.8273E-4mm$^3$)

**Table 12 Droplet size calculation**

|   | 2D droplet diameter (μm) | 3D droplet diameter (μm) |
|---|---|---|
| 0 | 0 | 0 |
| 1 | 96.1 | 29.2 |
| 2 | 149.7 | 56 |
| 3 | 173.4 | 70.4 |
| 4 | 183.2 | 73.8 |

**Table 13 Droplet size distribution**

| Diameter | Number of Droplets (2D) Ave size (43.78μm) | Number of Droplets (3D) Ave size (10.02μm) |
|---|---|---|
| $D < 20\mu m$ | 9 | 123 |
| $20\mu m <= D < 40\mu m$ | 30 | 17 |
| $40\mu m <= D < 60\mu m$ | 14 | 1 |
| $60\mu m <= D < 80\mu m$ | 12 | 0 |
| $80\mu m <= D < 100\mu m$ | 21 | 0 |
| $100\mu m <= D$ | 17 | 0 |

**5.5 CONCLUSION**

The following conclusions can be drawn from the present chapter:

- The important MQL parameters such as droplet size and distribution were studied in terms of the nozzle distance and air pressure.

- The experimental technique to measure the droplet sizes and distribution for MQL combining CSLM and wavelets analysis proposed and proved to be successful.

- Using the edge detection algorithm, the boundary of each droplet on the substrate was identified and the area fraction covered by the droplets based on the area and average size (diameter) of droplets can be determined for various nozzle-workpiece distance and nozzle air pressure.

- Based on the observation, it can be inferred that the higher nozzle pressure provided the more droplets but the smaller droplets were obtained while a smaller amount of droplets was deposited on the surface when the nozzle distance was increased. The maximum area fraction covered by droplets was obtained at the nozzle distance of 30mm and the air pressure of 12psi. However, high air pressure does not provide the condition to wet the cutting zone especially with the nozzle distance more than 50mm.

- The volume of a droplet was calculated using wavelet transform (Daubechies7 mother wavelet). The wavelet decomposition of the droplet surfaces was performed up to $7^{th}$ level and the $4^{th}$ level is the threshold limit for the feasible extraction of the droplet shape. Therefore, the images between $1^{st}$ and $4^{th}$ levels can be used for the volume calculation.

- The size of small droplets (less than 100μm) can be estimated by using the equation that represents an empirical correlation between diameter of 2D optical droplet images and 3D droplet images. The average diameter of 3D droplets was 10.02μm. This droplet size information in terms of lubricant type and spray condition can be useful not only to evaluate the penetration ability of lubricant into cutting zone but to determine the operator's health hazards, especially for very small droplets.

- The proposed approach of the MQL parameters in this work can be used to determine optimal MQL conditions prior to each machining application, which ultimately increases the efficiency of the machining process. The optimal MQL parameters will be depending on the particular MQL oil used and an operating condition of a particular MQL system. Thus, this paper introduces a new method to for such parametric study

Chapter 6

## MQL WITH NANOGRAPHENE-ENHANCED LUBRICATES: BALL MILLING EXPERIMENT

In a view of green manufacturing, dry machining has drawn much attention from industries recently. Remarkable improvement on tool coating technology has facilitated the complete elimination of cutting fluid in some machining processes. In most applications, however, the cutting fluids are still required due to the high friction and adhesion tendency between work and tool materials and the difficulty of chip and heat removal [Sreejith and Ngoi, 2000, Klocke and Eisenblatter, 1997 and Kelly and Cotterell, 2002]. Therefore, in some applications, an optimal solution for lubrication condition can be found between dry machining and flood cooling. In this regards, minimum quantity lubrication (MQL) is a viable solution to overcome the disadvantages of both dry and flood cooling in machining processes.

The effectiveness of MQL process has been identified in turning [Dhar et al., 2006 and Kamata and Obikawa, 2007], milling [Rahman et al., 2002 and Lacalle et al., 2006] and drilling [Tasdelen et al., 2008, Heinemann et al., 2006, Davim et al., 2006 and Filipovic and Sephenson, 2006]. In addition, MQL process parameters, such as nozzle distance and direction, discharge pressure, flow rates, etc., have been studied to optimize the machining conditions [Park et al., 2010]. By means of confocal laser scanning microscopy (CLSM) and edge detection algorism techniques, optimal nozzle distance and air pressure of vegetable based oil was determined [Park et al., 2010]. It was found that both nozzle position and oil flow rate had the important roles on machining performance [Lacalle et al., 2006 and Ueda et al., 2006].

Several works have been published to evaluate the characteristics of various lubricants for finding optimum lubricants in MQL machining. The mixture of water and oil-free synthetic

lubricant provided longer tool life compared to both synthetic ester with and without alcohol in deep-hole drilling due to the high cooling ability and low viscosity of water [Heinemann et al., 2006]. A new lubricant type, oil film on water droplets, was proposed to provide a better cooling ability on top of improved lubricity and showed less cutting forces in end milling [Itoigawa et al., 2006 and Yoshimura et al., 2005]. Cutting performance in the tapping test as well as secondary factors (biodegradability, oxidation, and storage stability) for synthetic polyor esters was superior to vegetable oil [Wakabayashi et al., 2006 and Suda et al., 2002].

Solid materials (nano-sized) have been developed as a lubricant itself, which can eliminate cutting fluids, or as an additive for lubricant. For the solid lubricant materials, molybdenum disulfide ($MoS_2$), graphite, boron nitride and polytetrafluoroethylene (PTFE) have been used as dry powders or coating materials [Jianxin et al., 2009, Krishna and Rao, 2008 and Xu et al., 2004]. In the machining test, these solid lubricants reduced the cutting forces and surface roughness [Krishna and Rao, 2008, Reddy and Rao, 2006]. On the other hand, the solid lubricants can be also mixed with the oil based lubricants. In the grinding processes, MQL lubricant with $MoS_2$ nano-sized particles was introduced in [Shen et al., 2008] and $MoS_2$ grinding lubricant showed excellent performance on cutting forces in spite of its low dissociation temperature at 350°C in oxidizing environments. The performance of diamond nano-particles in oil was evaluated in terms of friction and a wear test using ball on disc type equipment, which showed high loading capacity and less friction and wear [Tao et al., 1996]. The nano-graphene platelet enhanced lubricants were studied in various conditions [Park et al., 2010, Huang et al., 2006, Lee et al., 2009 and Alberts et al., 2009]. The nano-particle enhanced lubricants are expected to provide better performance because nano-graphene has not only a higher dissociation temperature but also the high aspect ratio, which naturally orients the graphene phase for better

lubricity when applied through MQL process. In addition, the type and concentration of solid lubricant in oil can be also important factors for an optimal use of the cutting fluids in machining applications [Krishna and Rao, 2008 and Alberts et al., 2009]. The machining performance is also affected by the additive in lubricant. Boric acid with 20% by weight mixed with SAE 40 oil was found to be optimal lubricant for tool wear and surface roughness in turning of EN8 steel [Krishna and Rao, 2008].

This paper studies the effect of the exfoliated nano-graphene enhanced lubricant by conducting wetting angle measurement, friction tests using a ball-on-disk set-up and MQL ball milling test. First, wetting angles for a variety of commercially available lubricants including nano-graphene enhanced oil were tested in order to evaluate the wettability of lubricants. Second, the friction coefficients of each lubricant and a dry nano-graphene coated insert were measured as a function of load and speed to determine if the introduction of nano-graphene, either in a discrete particulate, or multiple nano-graphene layer format, will reduce the friction. Third, ball milling tests were performed to evaluate the proposed nano-graphene enhanced lubricant in a practical machining application.

## 6.1 NANO-GRAPHENE ENHANCED LUBRICANT

Exfoliated graphite nanoplatelets (xGnP), produced by XG Sciences, Inc. (East Lansing, Michigan), were obtained from acid intercalated expandable graphite and a microwave exfoliation method [Park et al., 2010 and XG Science, Inc.]. In this chapter, these xGnPs were mixed with vegetable oil to yield a nano-enhanced MQL lubricant, which was patented by Kwon and Drzal [Kwon and Drzal, 2009]. Figure 53 shows the xGnPs used in this study, where the diameters are between 1 to 15μm (Figure 53 (a)) and the thickness are 10nm (Figure 53 (b)).

The MQL vegetable-based oil (provided by Unist, Inc. Grand Rapid, MI) was mixed with 0.1 and 1.0 wt% of xGnPs in a high shear mixer (SpeedMixer DAC 150FVZ-K from FlackTek, Inc.) for a stable suspension. When the xGnP-enhanced lubricant was used in MQL machining, it was expected that the larger size of xGnPs can be easily adhered on the cutting surface. When two interacting surfaces are sliding with the xGnP-enhanced lubricant, the friction is expected to be reduced as one graphene sheet is sliding over another. As shown in Figure 54, however, the large diameter (15μm) xGnP particles with both 0.1 and 1.0wt% were segregated only within a day (Figure 54 (B and C)). The 0.1wt% xGnP with 1μm diameter oil mixture showed the stability even over a year (Figure 54 (A)) while that of 1.0 wt% was separated after a few days (Figure 54 (B)). Therefore, the oil mixed xGnPs with 1μm diameter was only used; 0.1wt% xGnP oil was directly applied using MQL equipment while 1.0wt% oil was applied by means of a magnetic stirrer to keep a uniform concentration spray during the machining.
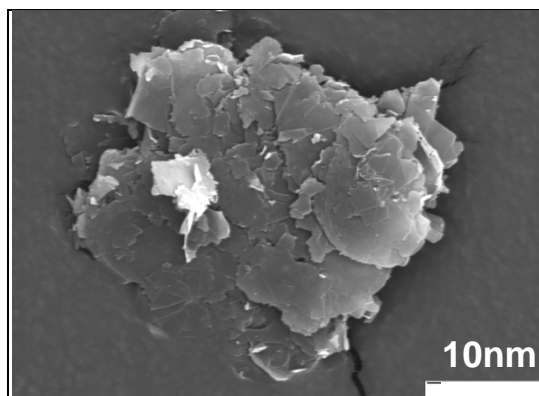
(a) SEM image (Diameter)
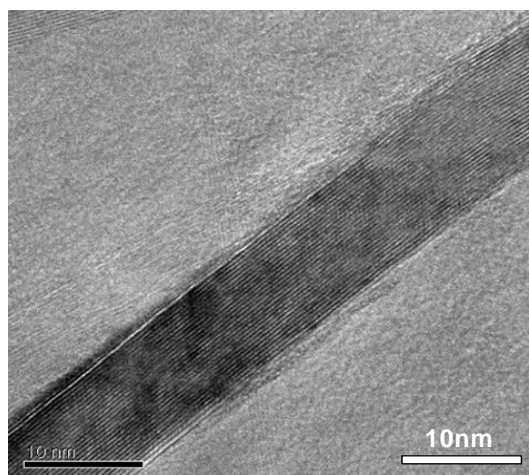


(b) TEM image (Thickness)

**Figure 53 (a) SEM and (b) TEM images of xGnP**



**Figure 54 Suspension stability of xGnP oils (A: 1μm / 0.1wt%, B: 1μm / 1.0wt%, C: 15μm / 0.1wt%, D: 15μm / 1.0wt%)**

## 6.2 EXPERIMENTAL SETUP

### 6.2.1 Wetting angle measurement

The wetting angles of lubricants can be used to evaluate the wetting ability of lubricants on a cutting tool surface. A droplet of lubricant with a high surface tension resting on a low energy solid forms a spherical shape giving a high wetting angle. On the contrary, when the solid surface energy exceeds the liquid surface tension, the flat droplet profile with a low wetting angle is considered to have a good wettablility. As is shown in Figure 55, the wetting angle $\theta$ is defined by measuring the tangent line at the interface between the droplet and the cutting tool surface as shown in Figure 55.

Figure 56 shows the wetting angle measurement setup and various lubricants including tap water were selected for wetting angle measurements on the TiAlN coated carbide. The motorized syringe assembly manufactured by AST Product, Inc. dispenses a 0.5μl droplet onto the coating surface. The CCD camera then captures the droplet image produced by the LED black light. Thus, wetting angles were measured by detecting both boundaries of the droplet and the solid surface in contact angle measurement software.
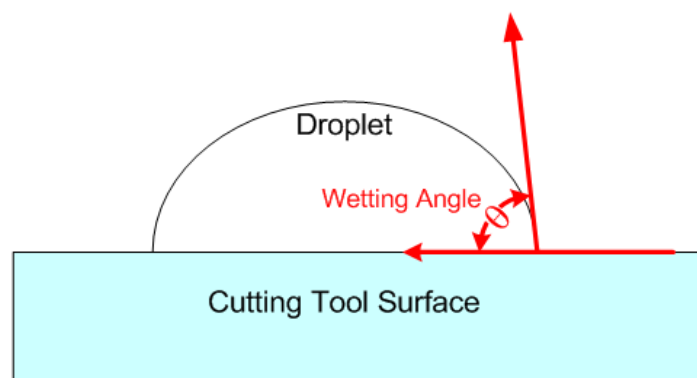


**Figure 55 Wetting angle of a droplet**
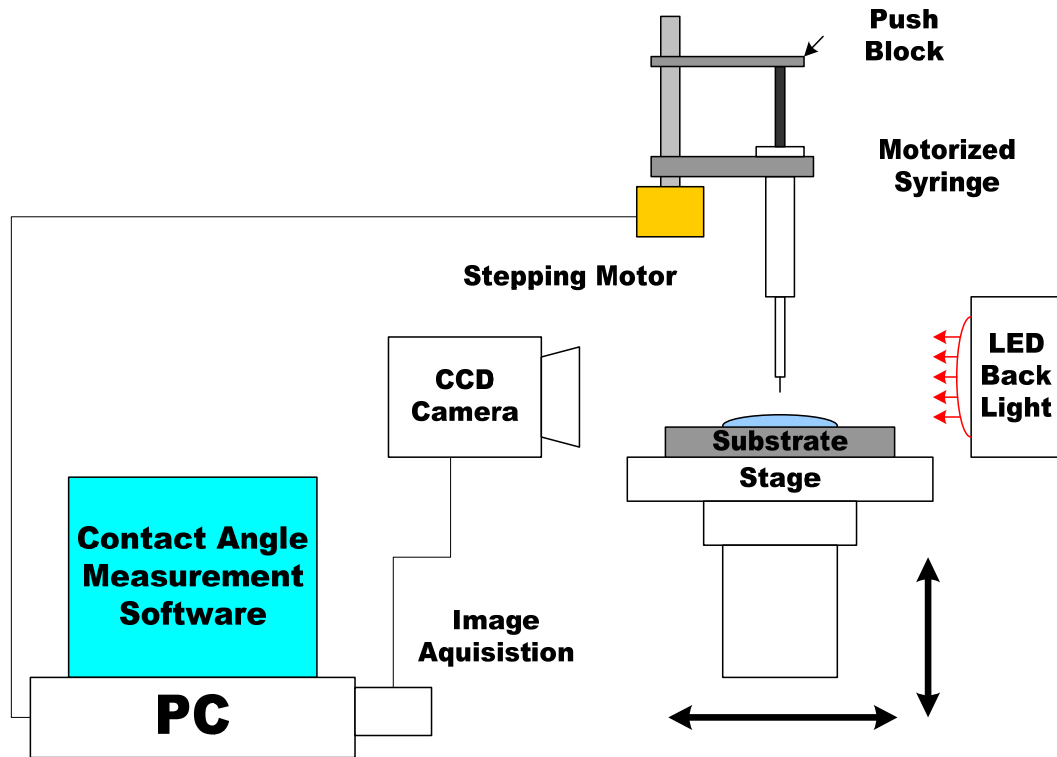
**Figure 56 Wetting angle measurement setup**

## 6.2.2 Tribometer test

As shown in Figure 57, the friction tests were performed with a liner ball-on-disc type tribometer (CSM Instruments) where a steel ball (440C) with 6.36mm in diameter oscillated on a TiAlN-coated carbide flat surface in order to evaluate frictional characteristics in various lubrication conditions. The test conditions include dry, vegetable oil (Unist-Coolube 2210), eight layers of graphene coatings and vegetable oil mixed with graphenes of 0.1 and 1.0wt%. Graphene coating technique can be found in [Biswas and Drzal, 2009], Loadings were 1, 5 and 10N and sliding speeds were 0.25, 1.0 and 2.5cm/s.
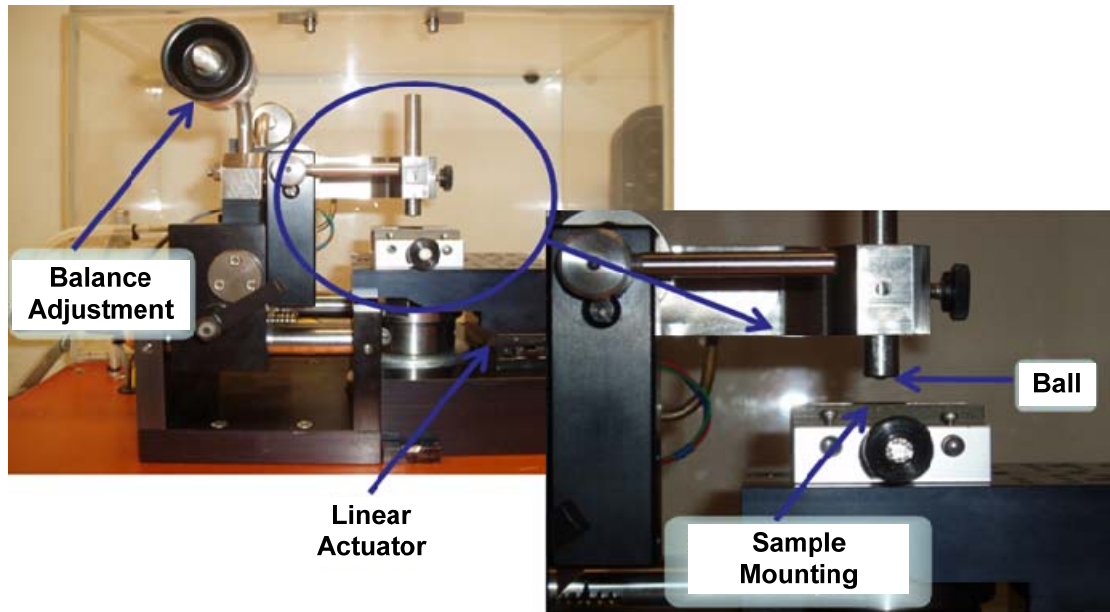
**Figure 57 Tribometer setup**

## 6.2.3 Ball milling Test

The MQL dispensing device (uni-MAX) provided by Unist, Inc. (Grand Rapid, Michigan) was used to provide the lubricant in a mist form to the cutting area. The lubricant, Unist Coolube 2210, was sprayed through an external co-axial nozzle. The nozzle outlet pressure and flow rate can be adjusted with the air metering screw and pulse duration/frequency in the control panel, respectively. However, we have used an optimized output pressure of 8psi and a flow rate of 1.5ml/min determined based on our previous work [Park et al., 2010 and Park et al., 2010(2)].

Ball-milling experiments were performed on a 3-axis vertical milling center (Sharnoa CNC mill) in dry and MQL conditions as shown in Figure 58. AISI 1045 steel (203.2mm×127mm×203.2mm) and 25mm diameter ball-nose TiAlN coated carbide inserts (ZPFG250-PCA12M) produced by Hitachi Tool Engineering were used for work and tool materials, respectively. The cutting started at one corner of the work material in the direction of

203.2mm and continued line by line until a layer of material was completely removed. The tool

wear was also measured after cutting each layer to record the progress of tool wear. The

machining and lubrication conditions are summarized in Table 14.
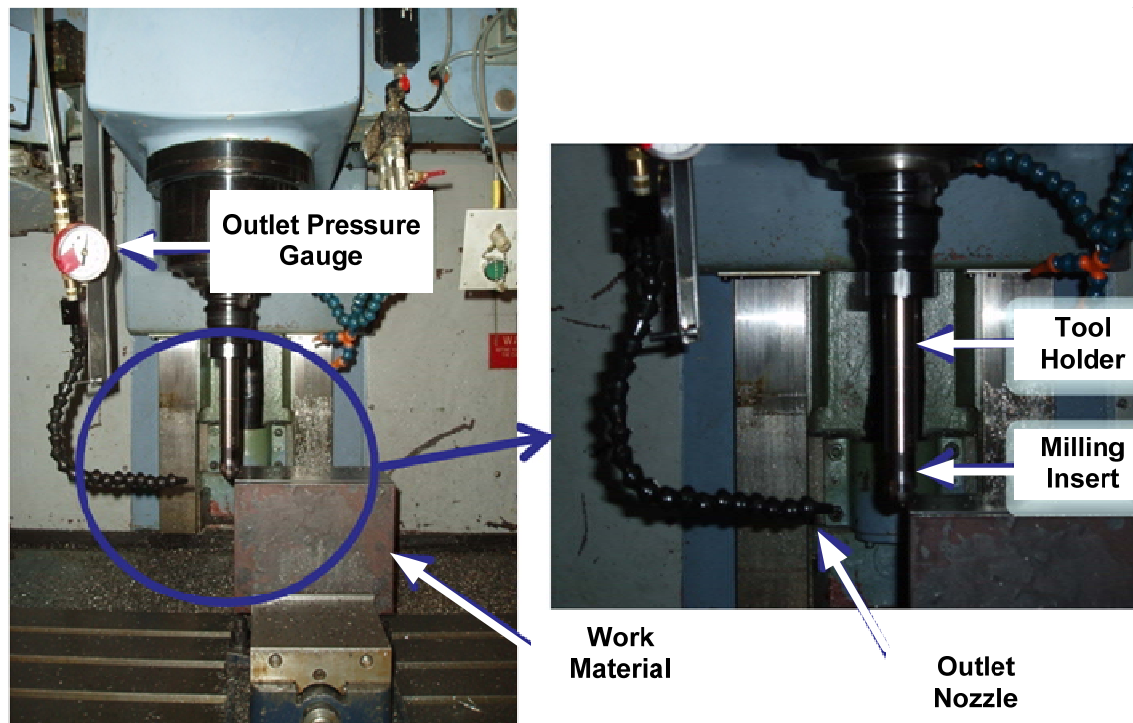


**Figure 58 MQL and ball milling setup**

**Table 14 Machining conditions**

| Cutting Speed (RPM) | 3500 & 4500 |
|---|---|
| Feed Rate (mm/min) | 2500 |
| Axial DOC (mm) | 1 |
| Radial DOC (mm) | 0.6 |
| Lubrication | Dry<br><br>NRG mineral oil 1: 15 (Water)<br><br>Unist Coolube 2210 (Vegetable oil)<br><br>Unist oil with xGnP (0.1 & 1.0wt%) |

Confocal laser scanning microscopy (CLSM) was used for the measurements of tool wear at the center of the ball-nose tool (central wear) and flank surface (flank wear), which were illustrated in Figure 59. Central wear can be attributed to 3-body abrasive wear due to the debris from the work material sliding between tool and work materials while flank wear comes from 2-body abrasion when cutting through complex pearlitic cementite phase constrained within the work material.



(a) Central wear          (b) Flank wear
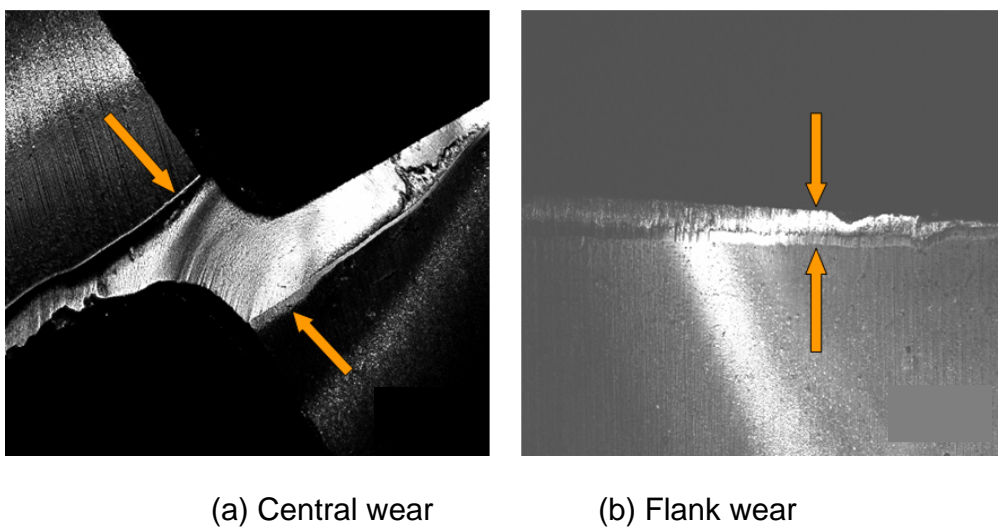
**Figure 59 Tool wear measurements of a ball nose insert**

## 6.3 RESULTS AND DISCUSSIONS

Figure 60 shows the result of wetting angle measurements on various lubricant candidates for MQL machining. Based on the assumption that a smaller wetting angle indicates a better wettablility to the tool surface, the wetting angle can be an important parameter that elucidates the lubrication performance. The result shows that water itself or water-based lubricant showed a higher wetting angle compared to an oil-based lubricant, as expected. Moreover, Unist oil with xGnP showed the best wettablility among the lubricants. It is expected that the xGnP-enhanced lubricant provides effective lubricity at the cutting interface in the machining process. This argument will be verified in ball milling test in this section. The oil based lubricant included 100% mineral oil produced by NRG Resources (NRG oil), which is water soluble oil. However, the pure NRG oil has a high viscosity (hard to spray) and is intended for use as a water soluble lubricant. Therefore, in this study, 100% NRG oil was not tested further.

| (54,52.1) | (26.4,27.3) | (18.3,18.3) | (25.4,26.2) | (35.1,33.5) |
|---|---|---|---|---|
| Water | Unist | Unist+xGnP | NRG 100% | NRG : Water 1:15 |
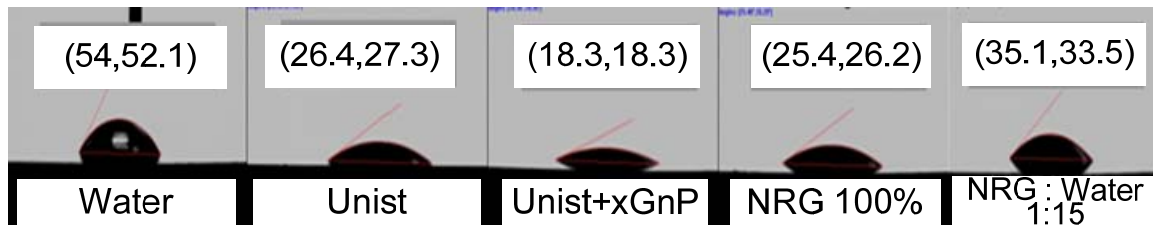
**Figure 60 Wetting angle test results**

Various lubrication conditions including dry, vegetable oil, eight layers of graphene coatings and a combination of the latter two were tested under a variety of loads and speeds for the tribological characteristics. In a dry condition, the friction coefficient was inversely proportional to the relative sliding speed as shown in Figure 61 (a) while as the load applied between ball and TiAlN-coated carbide increased, the friction decreased (Figure 61 (b)).

137

Similarly, Unist oil showed the same result as in dry. When the xGnPs are applied on the track of sliding, it was not effective in reducing the friction because the loosely applied xGnPs cannot be sustained in their positions at the interface between ball and surface. Alternatively, the eight layers of graphene (5nm thickness) have been coated onto the TiAlN coated carbides using the coating technique described in [Biswas and Drzal, 2009], which consequently reduced the friction in the test. Figure 62 (a) and (b) compares the friction coefficients between dry and xGnP-coated samples from beginning to 300s. The graphene layers showed excellent performance in reducing the friction. Even if the most of graphene coatings were delaminated after about 100 seconds, the friction did not increase compared to the dry case because the xGnPs detached from the coating are suspected to be remained at the interface still working as a lubricant. Especially, the friction was fairly stable at the beginning of the run, which represents the outstanding lubricity of the graphene phase. In this regard, it can be stated that the friction can be effectively reduced if the graphene phase can be applied appropriately at interface. However, when Unist oil was applied onto the graphene-layered, TiAlN coated carbides, the friction did not reduce further because the xGnP-debris from the coatings taken from the sliding surface would neither be necessary to relocate into the interface nor be well mixed with the oil being applied. This is why the nano-graphene particles must be uniformly suspended in the oil. Similar to the wetting angle test result, the xGnP-enhanced Unist oil showed the lowest friction coefficient as seen in Figure 63 (a). In addition, the effect of the concentration of xGnP in Unist oil was investigated; and 0.1wt% xGnP of 1μm diameter showed a slightly lower friction coefficient than 1wt% of that and pure Unist oil, as in Figure 63 (b). And note that the xGnP of 15μm diameter lubricant was not tested due to its poor suspension stability in the oil as mentioned in Sec 6.1.
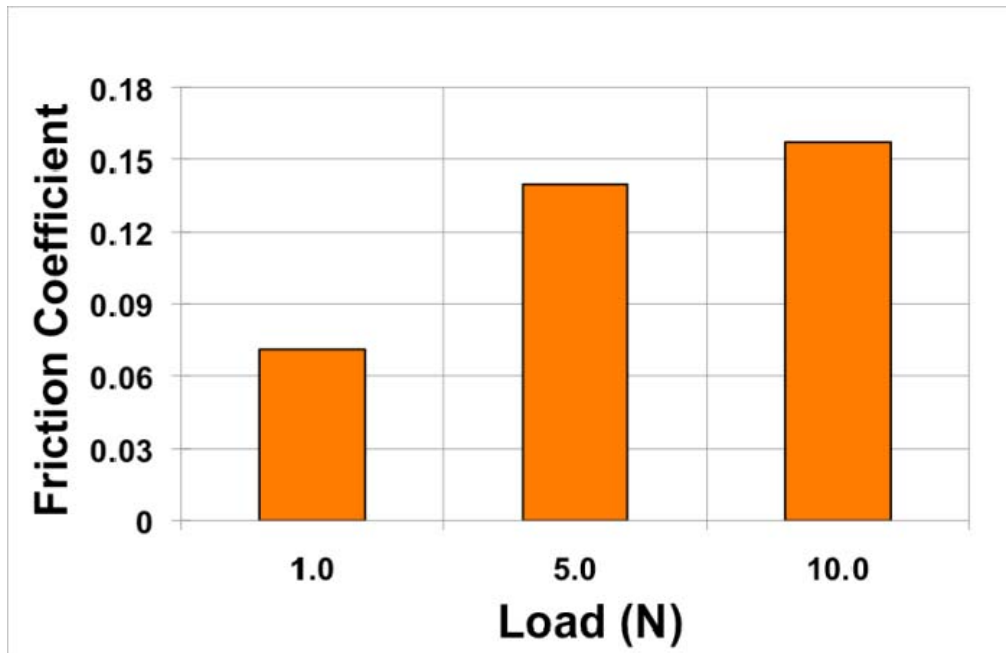
(a) Load effect (Dry)
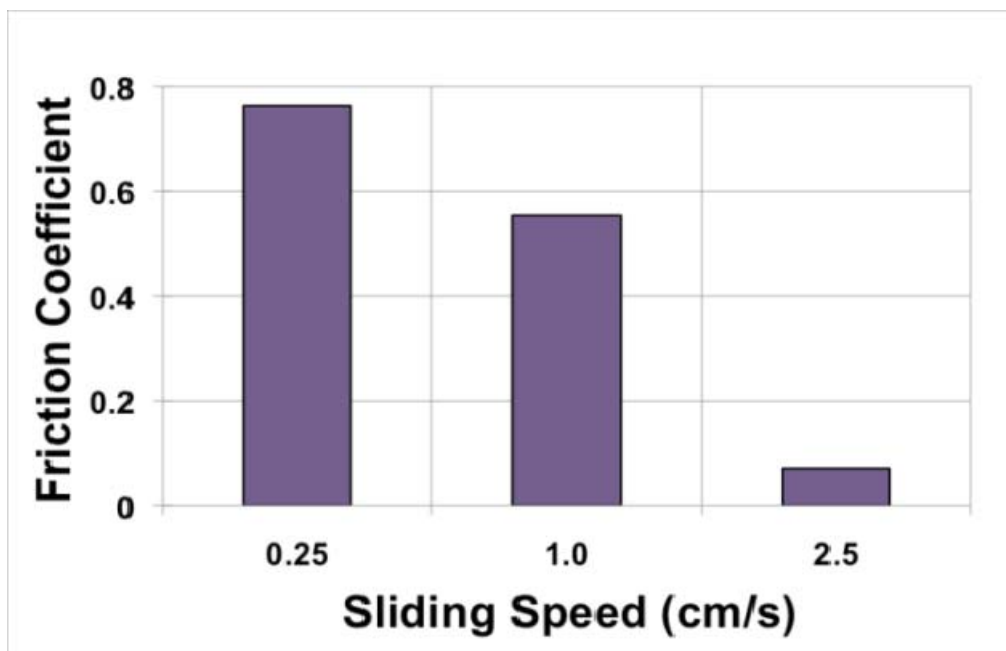


(c) Speed effect (Dry)

**Figure 61 Tribometer test results for various lubricants**

**Figure 61 (cont'd)**
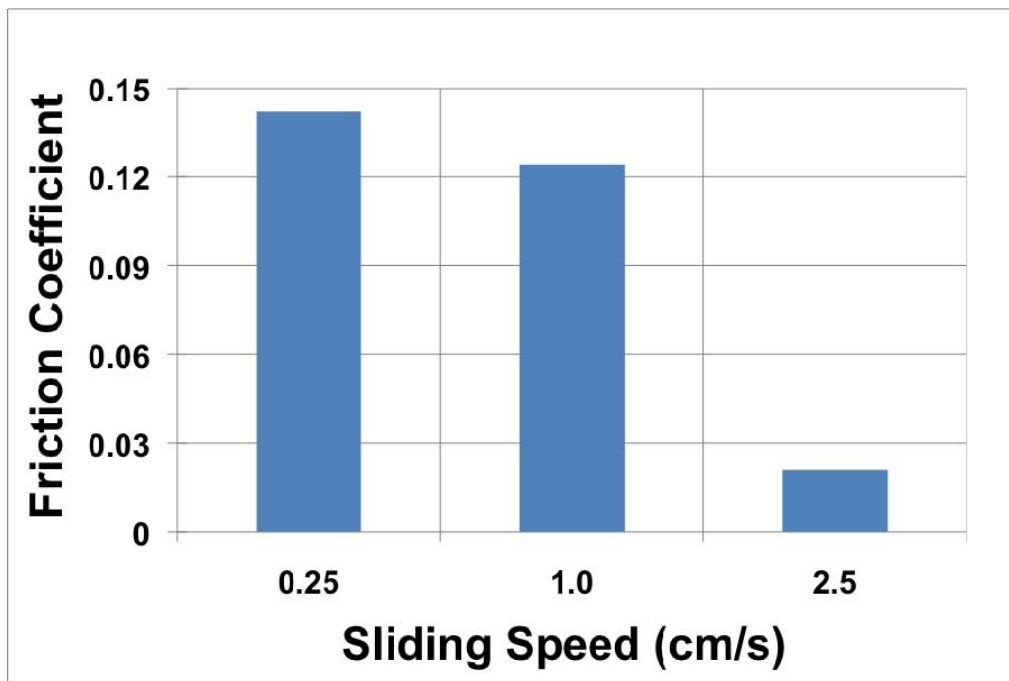


(c) Speed effect (Unist oil)
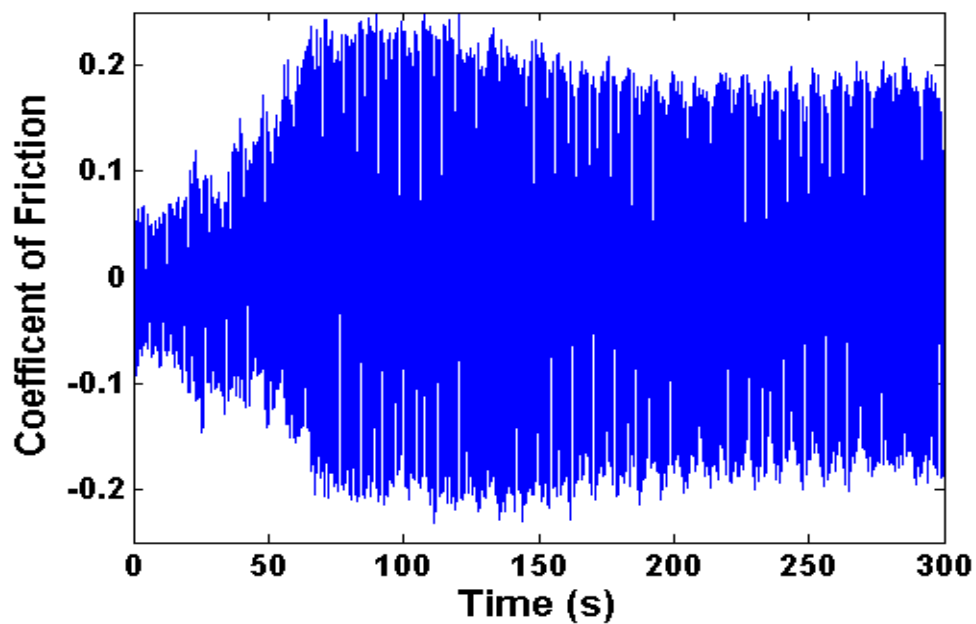


(a) Dry

**Figure 62 Comparison of friction coefficients of dry and xGnP coating**

140

**Figure 62 (cont'd)**
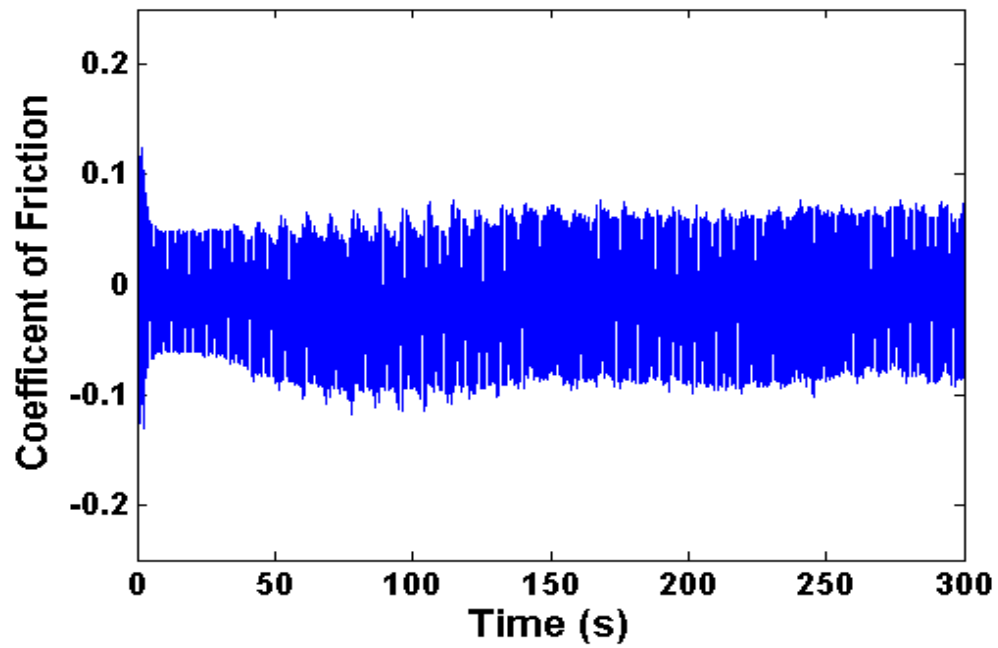


(b) Graphene coating (8 layers)
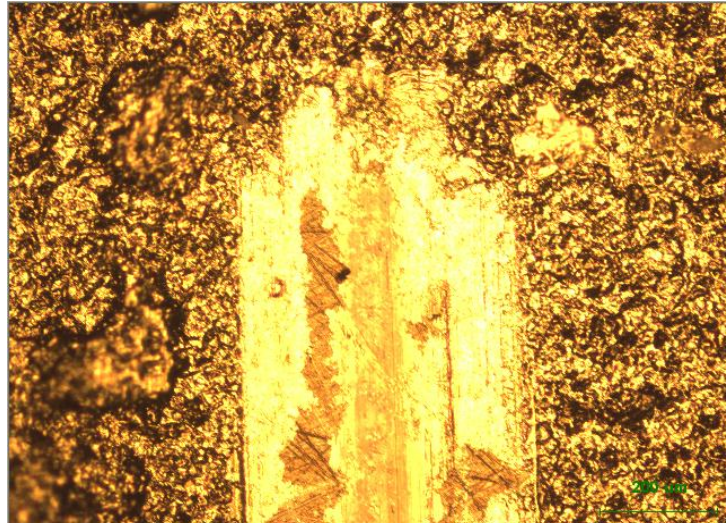


(c) Microscope image after 100s
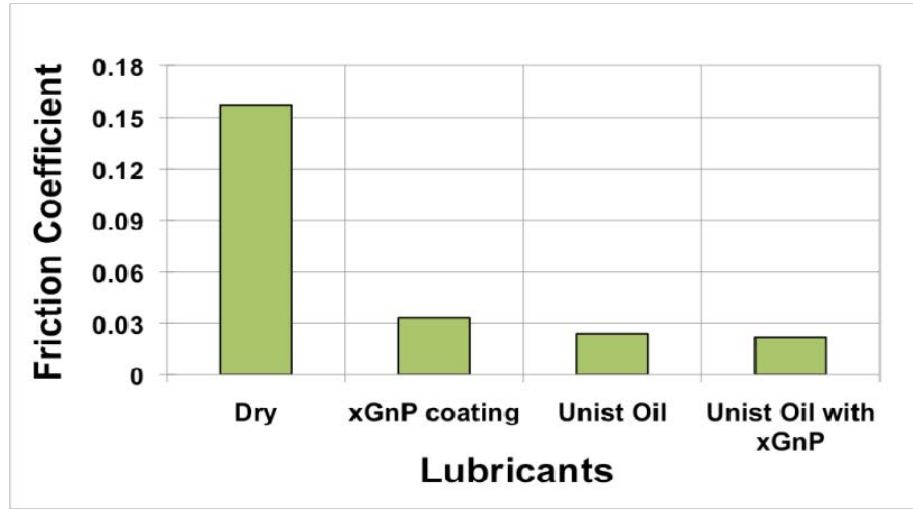
(a) Various lubricants
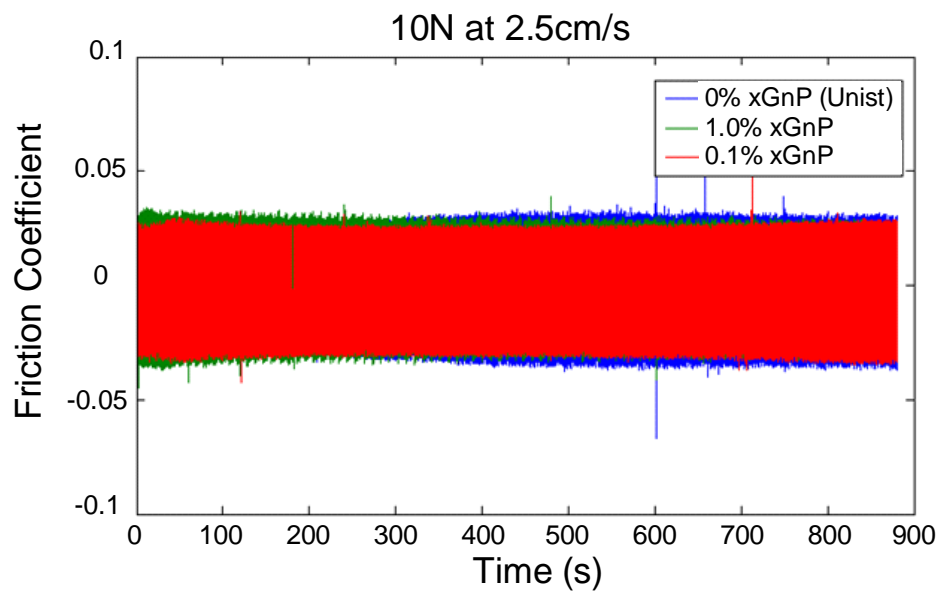


(b) Various xGnP concentrations

**Figure 63 Comparison of friction coefficients of lubricants**

Figure 64 represents the central wear measured at 3500rpm for dry, NRG water-soluble

oil, Unist oil, and Unist oil mixed with xGnP. It was reported that central wear occurred for

coated carbide end mills with relatively low feed rate (less than 1000mm/min) in high-speed

milling [Sokovic et al., 2004]. However, in this test, the central wear was observed, as seen in Figure 64, even with the feed rate of 2500mm/min. Especially in dry machining the central wear became significant because the center of ball nose insert is always contacting the work material without the cutting fluid medium reaching the area. Thus, the wear particles cannot be evacuated and abraded the cutting tool. Unlike Unist oil, the mineral NRG oil did not provide any beneficial effect on the central wear; therefore, the NRG oil was eliminated from any additional experiment.
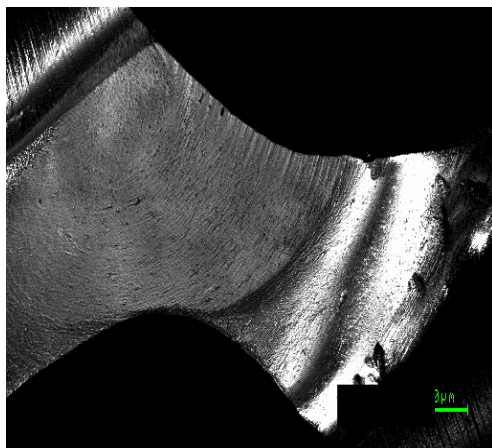


(a) Dry
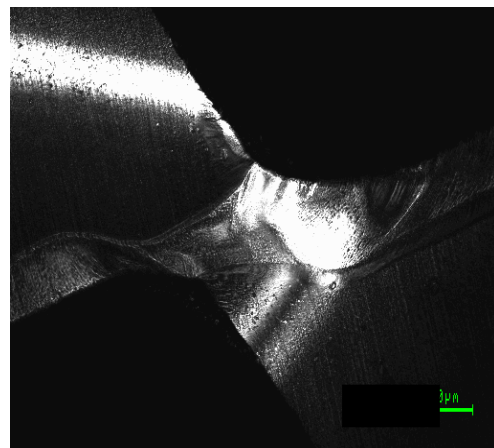
(b) NRG water soluble oil
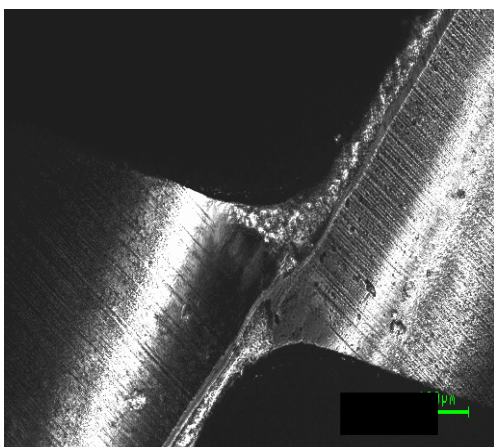


(a) Unist oil
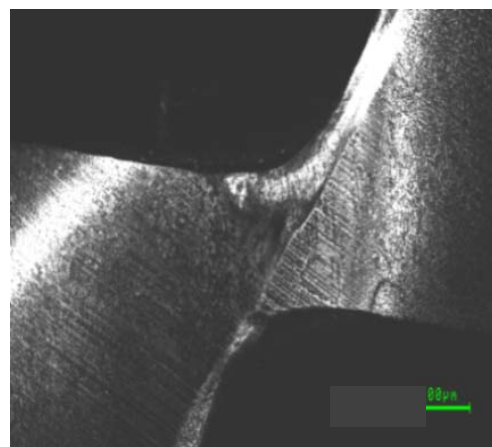
(b) Unist oil with xGnP (0.1wt%)

**Figure 64 Central wear at 3500rpm at 8$^{th}$ layer**

Flank wear was also measured at various conditions. Figure 65 compares the effect of MQL lubricants on the flank wear at the spindle speed of 4500rpm. Unist oil mixed with xGnPs was superior compared to dry and Unist oil only, regardless of the concentration of xGnP. Moreover, considering edge chipping, the beneficial effect of xGnP became more obvious. As seen in Figure 65 (a) and (b), the machining experiments in dry and Unist oil only show chipping at the cutting edge while, as shown in Figure 65 (c) and (d), the cutting edge maintained its sharpness. Therefore, the presence of xGnPs has deterred the chipping at the cutting edge. It can be concluded that the xGnP stay at the cutting interface by providing the lubricity and relieving the mechanical impact generated during the milling process.
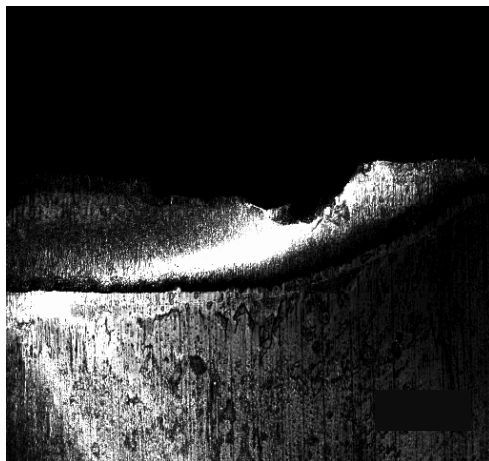


(a) Dry                                    (b) Unist oil only

**Figure 65 Flank wear at 4500rpm at 8$^{th}$ layer**

**Figure 65 (cont'd)**
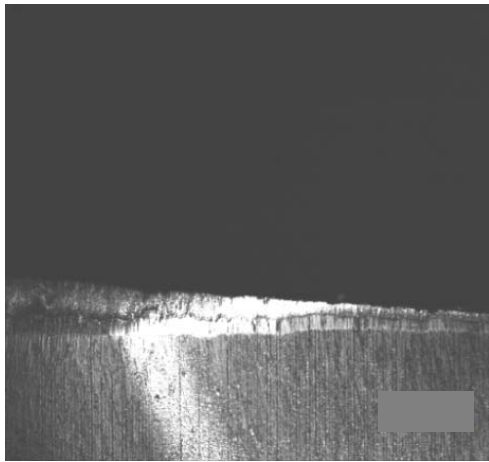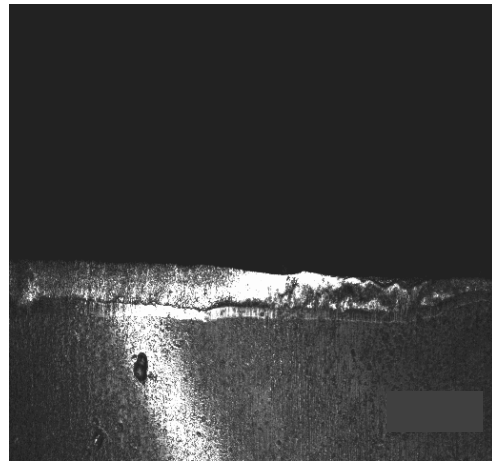


(c) Unist oil with xGnP (0.1wt%)       (d) Unist oil with xGnP (1.0wt%)

To investigate the effect of the xGnP concentration, both central wear and flank wear

measured after machining each layer up to $8^{th}$ layer were plotted against spindle speeds as shown

in Figure 66. In terms of reducing the central wear, the xGnP-enhanced lubricant is substantially

better than traditional MQL vegetable oil at both cutting speeds. The overall performance of the

0.1wt% xGnP oil was superior to that of the 1.0wt% one. This result corresponds with the

friction test result as the higher friction for 1.0wt% xGnP could cause slightly increase in flank

wear. As mentioned in Sec. 6.1, due to the notable amount of the xGnP precipitation for the

concentration of 1.0wt%, it had some difficulty in spraying a uniformly distributed lubricant in a

machining application, which might lead to diminish the effectiveness of xGnP lubricant.

Remarkable improvement on the central wear was observed when the xGnP enhanced lubricant

was used, as shown in Figure 66. In fact, the central wear is almost non-existent with the xGnP-

enhanced vegetable oil with the concentration of 0.1wt%, providing the best results. Therefore, it

can be stated that the optimal concentration of xGnP is around 0.1wt%, which means that the

higher xGnP concentration in the lubricant does not necessary provide any additional benefit on friction reduction and machining performance. In summary, the flank wear ($V_B$) at high cutting speed was larger than that at low cutting speed as seen in Figure 66 (c) and (d)). Only Unist oil showed the larger flank wear at low speed at $6^{th}$ and $7^{th}$ layers. This is due to the catastrophic increase in wear rate during the interrupted cutting process where mechanical and thermal shock can be established. Again, flank wear rates of xGnP 0.1w% at low and high cutting speeds increased steadily while Unist oil showed unstable wear rate, resulting in the outstanding performance of xGnP 0.1wt% oil as MQL lubricant in milling process.
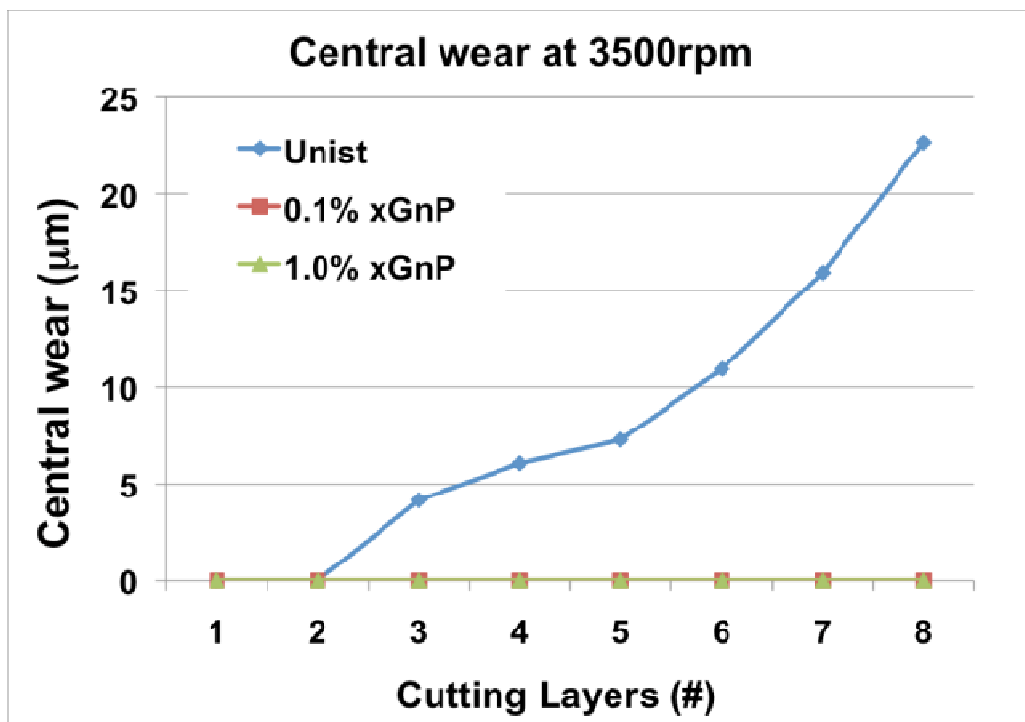


(a) Central wear at 3500rpm

**Figure 66  Central wear and flank wear in terms of concentration of xGnP**

**Figure 66 (cont'd)**
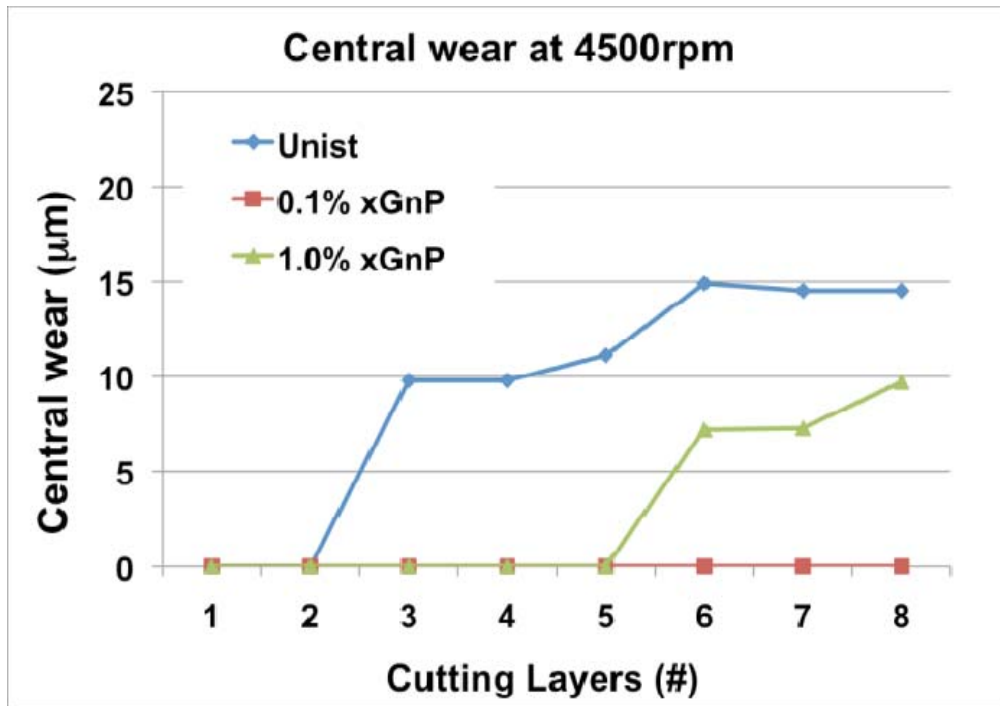


(b) Central wear at 4500rpm
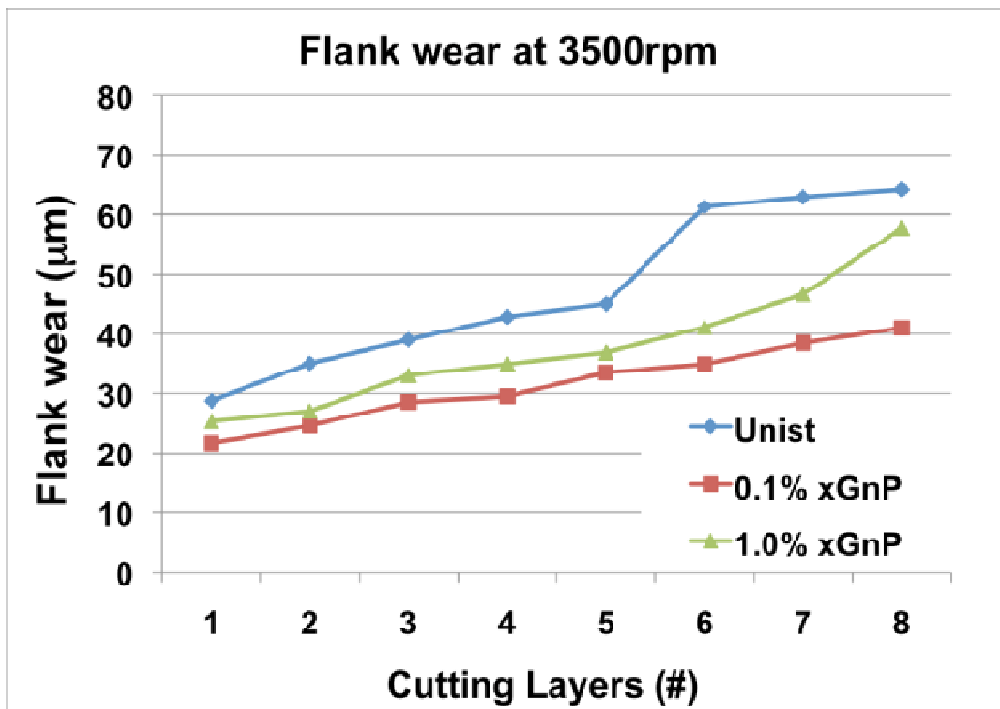


(c) Flank wear at 3500rpm

**Figure 66 (cont'd)**
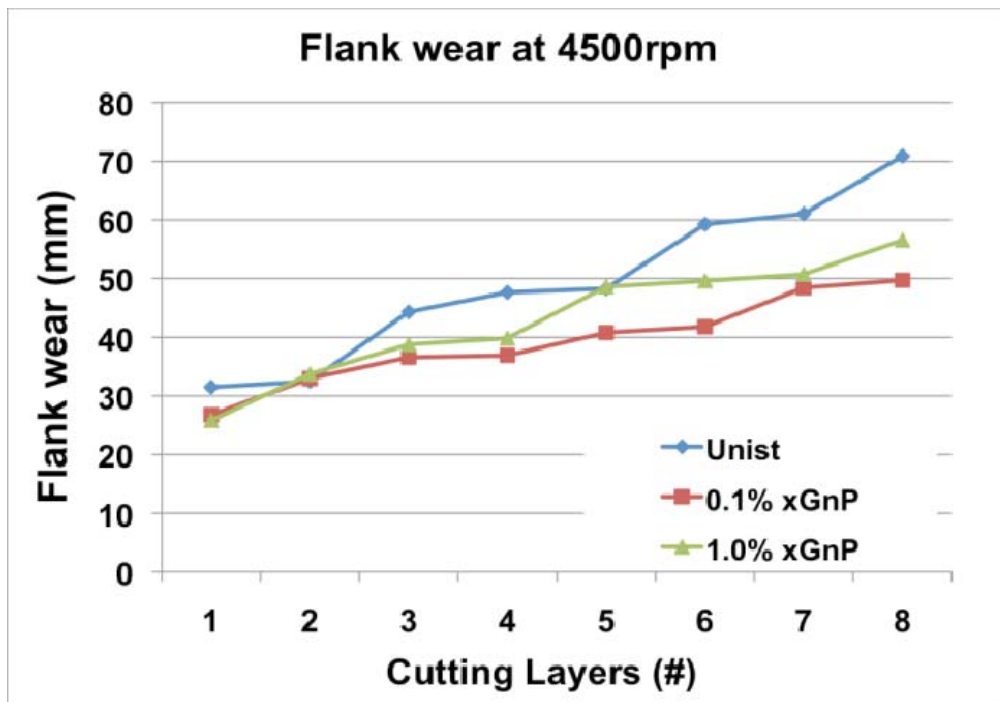


(d) Flank wear at 4500rpm

**6.4 CONCLUSION**

In this chapter, the effect of the nano-graphene additive (xGnP) in vegetable oil was investigated by comparing lubricants (dry, water-soluble oil and vegetable oil only) in the wetting angle measurement, the tribological behavior, and the ball milling. The results from the wetting angle test and the friction coefficient measurement show that xGnP-enhanced vegetable oil improved the wettablility on the cutting surface and reduced the surface friction. These results were verified by the ball milling experiment, which indicates that MQL machining provides better performance, especially for the central wear and chipping at cutting edge. In addition, the larger diameter xGnP did not show a stable suspension in vegetable oil, which caused segregation of graphene and oil. The concentration of xGnP 0.1wt% with 1μm diameter showed outstanding cutting performance without any segregation problem.

Chapter 7

## CONCLUSIONS

In this work, a tool wear analysis in various machining processes, such as turning, milling and drilling , and a study on MQL parameters including droplet size and distribution, nozzle distance, outlet air pressure, lubricant types, etc., which might affect the machining efficiency, were performed. In addition, the combination of CLSM and image processing techniques including wavelet transform was used for obtaining the 3D surface topography and developing droplet size measurement techniques.

In turning of AISI 1045 steel, the dominant wear phenomenon was abrasion by hard inclusion in work material and then adhesion, by high affinity of steel and carbide, took over after carbide was exposed. In addition, 2-body abrasion model in conjunction with FEM simulation was used for flank wear prediction and the predicted wear profiles showed very good results compared with the experimental data. Based on the combination of model and experimental approaches, no significant beneficial effect on multilayer coating was observed for flank wear as a single hard coating is adequate to resist abrasion. In contrast, for the crater wear, multilayer coating was much effective due to not only $Al_2O_3$ middle layer coating, which has high wear resistance against dissolution, but also the changes in interface conditions of multilayer coating as each layer was being exposed, which resulted in the maximum crater location changes instead of concentrating on one location.

In a face milling study, multilayer cutting tools, double (TiN/TiAlN) and triple (TiN/$Al_2O_3$/TiCN) layered coated carbide, processed by PVD and CVD respectively, were evaluated in terms of various cutting conditions. As expected, depth of cut (DOC) did not play a significant

role in the evolution of flank wear while the cutting speed had an important role in flank wear. Similar to the turning case, abrasion was found to be the most dominant tool wear mechanism in milling. Edge chipping and micro-fracture were the tool failure modes. After comparing the performance of the two inserts, it was concluded that the double layer coating was superior to the triple layer coating under various cutting conditions due to the benefit coming from the coating deposition processes themselves. Additionally, it is commonly claimed that the superior performance of the multilayer coating comes from preventing the gross fracture or crack into tool materials instead of propagating the crack along the coating interfaces. However, no such observations were found in both turning and milling experiments. Mainly, the flank wear rate was dependent upon the hardness of the coating materials.

A similar study on drilling has been conducted. In particular, drilling of carbon fiber reinforced polymer (CFRP)/titanium (Ti) stacks was performed using carbide and PCD drills. Due to the dissimilar mechanical and thermal properties of the CFRP/Ti stacks, wear behaviors in drilling CFRP and Ti drastically was changed. The dominant wear mechanism for carbide tools was the abrasion by fibers in CFRP drilling and Ti adhesion, covering entire cutting edge while the main wear behavior of PCD drill was edge chipping. The adhesion of titanium seemed to be the most important factor in tool wear and micro-chipping because the adhered titanium was brushed away by the fibers in CFRP when drilling the composites, which accelerated tool wear in drilling of stacks. PCD drills showed more wear resistance than carbide drills only in terms of flank wear. However, due to the inherent brittleness of PCD drills, chipping was observed at the tool edge when drilling titanium. As expected, higher cutting speeds caused higher torque and thrust force, which resulted in a significant increase in tool wear, especially in drilling of titanium.

151

Finally, for a better understanding of Minimum Quantity Lubrication (MQL) and its effective use in practical industrial applications, MQL parameters such as droplet sizes, the droplet distributions and wetting angles of various lubricants including the nano-graphene (xGnP) enhanced vegetable oil were investigated. The measurement method of droplet size and distribution was proposed using CLSM and wavelet transform. In addition, the empirical droplet size estimation equation was also introduced for extremely small droplets, which is hard to be measured. The distribution of the droplets was also studied to determine the MQL optimal nozzle-workpiece distance and the nozzle discharge pressure using the edge detection algorithm. To extent the applicability of MQL to more aggressive machining conditions, a potential additive to MQL lubricant, which is a mixture of exfoliated nano-graphene particles and vegetable oil, was developed. After the wetting angle and friction tests for the various lubricants, it was found that oil based lubricant, especially nano-enhanced vegetable oil, showed a better wettablility and tribological behavior. MQL-ball milling tests with nano-graphene enhanced lubricant were performed to show a remarkable performance improvement in reducing both central wear and flank wear as well as edge chipping. In addition, it was noted that higher concentration of nano-graphene did not provided any additional benefit on both central and flank wear.

BIBLIOGRAPHY

Alberts, M., Kalaitzidou, K., Melkote, S., 2009, "An investigation of graphite nanoplatelets as lubricant in grinding," *International Journal of Machine Tools & Manufacture*, Vol. 49, pp. 966-970.

Askvik, K.M., Hoiland, S., Fotland, P., Barth, T., Gronn, T. and Fadnes, F. H., 2005, "Calculation of wetting angles in crude oil/water/quartz systems," *Journal of Colloid and Interface Science*, Vol. 287, pp. 657-663.

Barish, H., 1998, "Quality drills contribute to successful titanium tooling," *Cutting Tool Engineering*, Vol. 40, pp. 38-42.

Biswas, S. and Drzal, L.,2009, "A novel approach to create a highly ordered monolayer film of graphene nanosheets at the liquid-liquid interface," *Nano Letters*, Vol. 9, pp. 167-172.

Brinksmeier, E. and Janssen, R., 2002, "Drilling of multi-layer composite materials consisting of carbon fiber reinforced plastics (CFRP), titanium and aluminum alloys," *CIRP Annals-Manufacturing Technology*, Vol. 51, pp. 89-90.

Bull, S.J., Bhat, D.G. and Staia, M.H., 2003, "Properties and performance of commercial TiCN coatings. Part 1: coating architecture and hardness modelling," *Surface and Coatings Technology*, Vol. 163-164, pp. 499-506.

Chen, W.C., 1997, "Some experimental investigations in the drilling of carbon fiber-reinforced plastic (CFRP) composite laminates," *International Journal of Machine Tools & Manufacture*, Vol. 37, pp. 1097-1108.

Chen, L., Wang, S.Q., Zhou, S.Z., Li, J. and Zhang, Y.Z., 2008, "Microstructure and mechanical properties of Ti(C,N) and TiN/Ti(C,N) multilayer PVD coatings," *International Journal of Refractory Metals & Hard Materials*, Vol. 26, pp. 456-460.

Cselle, T. and Barimani, A., 1995, "Today's applications and future developments of coatings for drills and rotating cutting tools," *Surface and Coatings Technology*, Vol. 76-77, pp. 712-718.

Chandrasekaran, H. and Johansson, J.O., 1994, "Chip flow and notch wear mechanisms during the machining of high austenitic stainless steels," *CIRP annals*, Vol. 43, pp. 101-105.

Chung-Chen, T. and Hong, H., 2002, "Comparison of the tool life of tungsten carbides coated by multi-layer TiCN and TiAlCN for end mills using the Taguchi method," *Journal of Materials Processing Technology*, Vol. 123, pp. 1-4.

Davim, J.P., Antonio, C.A.C., 2001, "Optimal drilling of particulate metal matrix composites based on experimental and numerical procedures," *International Journal of Machine Tools & Manufacture,* Vol. 41, pp. 21-31.

Davim, J.P., Sreejith, P.S., Gomes, R. and Peixoto, C., "Experimental studies on drilling of aluminium (AA1050) under dry, minimum quantity of lubricant, and flood-lubricated conditions," *Proceedings of the Institution of Mechanical Engineers, Part B: Journal of Engineering Manufacture*, Vol. 220, pp. 1605-1611.

Dhar, N.R., Islam, M.W., Islam, S. and Mithu, M.A.H., 2006, "The influence of minimum quantity of lubrication (MQL) on cutting temperature, chip and dimensional accuracy in turning AISI-1040 steel," *Journal of Materials Processing Technology*, Vol. 171, pp. 93-99.

Dobrzanski, L.A., Pakula, D., Kriz, A., Sokovic, M. and Kopac, J., 2006, "Tribological properties of the PVD and CVD coatings deposited onto the nitride tool ceramics," *Journal of Materials Processing Technology*, Vol. 175, pp. 179-185.

El-Wardany, T.I., Gao, D. and M.A. Elbestawi, 1996, "Tool condition monitoring in drilling using vibration signature analysis," *International Journal of Machine Tools and Manufacture*, Vol.36, No.6, pp. 687-711.

Faraz,  A., Biermann, D. and Weinert, K., 2009, "Cutting edge rounding: An innovative tool wear criterion in drilling CFRP composite laminates," *International Journal of Machine Tools & Manufacture,* Vol. 49, pp. 1185-1196.

Filipovic, A. and Sephenson, D.A., 2006, "Minimum quantity lubrication (MQL) applications in automotive power-train machining," *Machining Science and Technology,* Vol. 10, pp. 3-22.

Fox, N.J. and Stachowiak, G.W., 2007, "Vegetable oil-based lubricants – A review of oxidation," *Tribology International*, Vol. 40, pp. 1035-1046.

Fu, S., Muralikrishnan, B. and Raja, J., 2003, "Engineering Surface Analysis with Different Wavelet Bases," *Journal of manufacturing Science and Technology*, Vol. 125, pp. 844-852.

Gadelmawla, E.S., Koura, M.M., Maksoud, T.M.A., Elewa, I.M. and Soliman, H.H., 2002, "Roughness parameters," *Journal of Materials Processing Technology*, Vol. 123, pp. 133-145.

Garrick, R., 2007, "Drilling Advanced Aircraft structures with PCD (Poly-Crystalline Diamond) Drills," *Society of American Engineer*,
http://www.sae.org/technical/papers/2007-01-3893

Gu, J., Barber, G.., Tung, S. and Gu, R.-J, 1999, "Tool life and wear mechanism of uncoated and coated milling inserts," *Wear*, Vol. 225-229, pp. 273-294.

Gururaja, S. and Ramulu, M., 2009, "Modified Exit-ply Delamination Model for Drilling FRPs," *Journal of Composite Materials*, Vol. 43, pp. 483-500.
Hanlon, D. N., Todd, I., Peekstok, E., Rainforth, W. M. and van der Zwaag, S., 2001, "The application of laser scanning confocal microscopy to tribological research," *Wear*, Vol. 251, pp. 1159-1168.

Heinemann, R., Hinduja, S., Barrow, G., and Petuelli, G., 2006, "Effect of MQL on the tool life of small twist drills in deep-hole drilling," *International Journal of Machine Tools & Manufacturing*, Vol. 46, pp. 1-6.

Heinke, W., Leyland, A., Matthews, A., Berg, G., Friedrich, C. and Broszeit, E., 1995, "Evaluation of PVD nitride coatings, using impact, scratch and Rockwell-C adhesion tests," *Thin Solid Films*, Vol. 270, pp. 431-438.

Hocheng, H. and Dharan, C.K.H, 1990, "Delamination During Drilling in Composite Laminates," *Transactions of ASME, Journal of Engineering for Industry*, Vol. 112, pp. 236–239.

Hocheng, H. and Tsao, C.C., 2003, "Comprehensive Analysis of Delamination in Drilling of Composite Materials with Various Drill Bits," *Journal of Materials Processing Technology*, Vol. 140, pp. 335–339.

Huang, H.D, Tu, J.P., Gan, L.P. and Li, C.Z., 2006, "An investigation on tribological properties of graphite nanosheets as oil additive," *Wear,* Vol. 261, pp. 140-144.

Hughes, J.I., Sharman, A.R.C. and Ridgway, K., 2004, "The effect of tool edge preparation on tool life and workpiece surface integrity," *Proceedings of the Institution of Mechanical Engineers Part B Journal of Engineering Manufacture* Vol. 218, pp. 1113-1123.

Iliescu, D., Gehin, D., Gutierrez, M.E. and Girot, F., 2010, "Modeling and tool wear in drilling of CFRP," *International Journal of Machine Tools and Manufacture*, Vol. 50, pp. 204-213.

Itoigawa, F., Childs, T.H.C., Nakamura, T. and Belluco, W., 2006, "Effects and Mechanisms in Minimal Quantity Lubrication Machining of Aluminum Alloys," *Wear,* Vol. 29, N. 3, pp. 339-344.

Jain, S. and Yang, D.C.H., 1993, "Effects of Feedrate and Chisel Edge on Delamination in Composites Drilling," *Transactions of ASME, Journal of Engineering for Industry,* Vol. 115, pp. 398–405.

Jawaid, A., Koksal, S. and Sharif, S., 2000, "Wear Behavior of PVD and CVD Coated Carbide Tools when Face Milling Inconel 718," *Tribology Transactions*, Vol. 43, pp. 325-331.

Jiang, X.Q., Blunt, L., Stout, K.J., 1999, "Three-dimensional surface topography characterization for orthopaedic joint prostheses," *Proceedings of the Institution of Mechanical Engineers*, Vol. 213, pp. 49-68.

Jianxin, D., Wenlong, S. and Hui, Z., 2009, "Design, fabrication and properties of a self-lubricated tool in dry cutting," *International Journal of Machine Tools & Manufacture*, Vol. 49, pp. 66-72.

Jun, M.B.G., Joshi, S.S., DeVor, R.E., and Kapoor, S.G., 2008, "An experimental Evaluation of an atomization-based cutting fluid application system for micromachining," *Journal of Manufacturing Science and Engineering*, Vol. 130, pp. 031118-1-031118-8.

Kamata, Y. and Obikawa, T., 2007, "High speed MQL finish-turning of Inconel 718 with different coated tools," *Journal of Materials Processing Technology*, Vol. 192-193, pp. 281-286.

Kanai, M. and Kanda, Y., 1978, "Statistical characteristics of drill wear and drill life for the standardized performance tests." *CIRP ANNALS*, Vol. 27, No.1, pp.61-66.

Kelly, J.F. and Cotterell, M.G., 2002, "Minimal lubrication machining of aluminum alloys," *Journal of Materials Processing Technology,* Vol. 120, pp. 327-334.

Kim, D. and Ramulu, M., 2004, "Drilling process optimization for graphite/bismaleimide titanium alloy stacks," *Composite Structures*, Vol. 63, pp. 101-114.

Kim, D., Doan. X. and Ramulu, M., 2005, "Drilling performance and machinability of PIXA-M and PEEK thermoplastic composites," *Journal of Thermoplastic Composite Materials*, Vol. 18 No. 3, pp. 195-217.

Kim, D. and Ramulu, M., 2007, "Study on the drilling of Titanium/Graphite Hybrid Composites," *ASME Journal of Engineering Materials and Technology,* Vol. 129 pp. 390-396.

Klocke, F. and Eisenblatter, G., 1997, "Dry Cutting," *CIRP Annals-Manufacturing Technology*, Vol. 46, No. 2, pp. 510-526.

Klocke, F. and Wurtz, C., 1999, "PCD in the machining of fibre-reinforced materials," *Industrial Diamond Review (UK),* Vol. 59, pp. 65- 70.

König, W., Wulf, C., Grass, P. and Willerscheid, H., 1985, "Machining of Fiber-reinforced plastics," *Annals of the CIRP*, Vol. 34, pp. 537–548.

Kramer, B.M. and Kwon, P.Y., 1985, "Computational Design of Coating Materials," *Journal of Vacuum Science and Technology*, Vol. A3, No.6, pp. 2349-2444.

Kramer, B.M. and Suh, N.P., 1980, "Tool wear by solution: a quantitative understanding," *ASME Transactions – Journal of Engineering for Industry*, Vol. 102, No. 4, pp. 303–309.

Krishna, P.V. and Rao, D.N., 2008, "Performance evaluation of solid lubricants in terms of machining parameters in turning," *International Journal of Machine Tools & Manufacture*, Vol. 48, pp. 1131-1137.

Kwon, P., 2000, " Predictive models for flank wear on coated inserts," *Journal of Tribology*, Vol. 122, pp. 340–347.

Kwon, P. and Drazl, L., 2008, "Nanoparticle Graphite Based Minimum Quantity Lubrication Method and Composition," Provisional Patent.

Lachuad, F., Piquet, R., Collombet, F. and Surcin, L., 2001, "Drilling of Composite Structures," *Composite Structures*, Vol. 52, pp. 511–516.

Lantrip, J., 2008, "New Tools Needed," *Cutting Tool Engineering*, Vol. 60-8, 8 pages. http://www.ctemag.com/pdf/2008/0808-Holemaking.pdf

Lee, C.-G., Hwang, Y.-J., Choi, Y.-M., Lee, J.-K, Choi, C. and Oh, J.-M., 2009, "A study on the tribological characteristics of graphite nano lubricants," *International Journal of Precision Engineering and Manufacturing,* Vol. 10, pp. 85-90.

Lin, S.C. and Ting, C.J., 1995, "Tool wear monitoring in drilling using force signals," *Wear,* Vol. 180, pp. 53–60.

Lin, S.C. and Chen, I.K., 1996, "Drilling carbon fiber-reinforced composite material at high speed," *Wear,* Vol. 194, pp. 156-162.

Lopez de Lacalle, L. N., Angulo, C.A., Lamikiz and Sanchez, J.A., 2006, "Experimental and numerical investigation of the effect of spray cutting fluids in high speed milling," *Journal of Material Processing Technology*, Vol. 172, pp. 11-15.

Madhavan, V. and Adibi-Sedeh, A.H., 2005, "Understanding of Finite Element Analysis Results under Framework of Oxley's Machining Model," *Machining Science and Technology*, Vol. 9, pp. 345-368.

Maksumov, A., Vidu, R., Palazoglu, A. and Stroeve, P., 2004, "Enhanced feature analysis using wavelets for scanning probe microscopy images of surfaces," *Journal of Colloid and Interface Science*, Vol. 272, pp. 365-377.

Melo, A.C.A., Milan, J.C.G. and Silva, M.B., 2006, "Some Observations on Wear and Damages in Cemented Carbide Tools," *Journal of the Brazilian Society of Mechanical Sciences and Engineering*, Vol. 28, pp.269-277.

Nabhani, F., 2001, "Machining of Aerospace Titanium Alloys," *Robotics and Computer Integrated Manufacturing*, Vol. 17, pp. 99-106.

Nasr, M.N.A., NG, E.-G. and Elbestawi, M.A., 2007, "Modelling the effects of tool-edge radius on residual stresses when orthogonal cutting AISI 316L," *International Journal of Machine Tools & Manufacture,* Vol. 47, pp. 401-411.

National Institute for Occupational Safety and Health (NIOSH), Chap. 1, Recommendation for a Metalworking Fluids Standard, www.cdc.gov/NIOSH/

Olortegui-Yume, J.A. and Kwon, P.Y., 2007, "Tool wear mechanisms in machining," *International Journal Machining and Machinability of Materials*, Vol. 2, pp. 316-334.

Olortegui-Yume, J.A. and Kwon, P.Y., 2007, "Crater Wear Evolution in Multilayer Coated Carbides During Machining Using Confocal Microscopy," *Journal of Manufacturing Process*, Vol. 9, pp. 47-60.

Olortegui-Yume, J.A., Park, K.-H., Kwon, P., Lee, G-B, and Park, S.-B., 2008, "Understanding Tool Wear of Multilayer Coated Carbides in Machining 1045 Steel," *NAMRI/SME Trans.*, XXXIV, pp. 383-390.

Olortegui-Yume, J.A., 2009, "Local tool wear profiles prediction using physics-based models," Ph.D. Dissertation at Michigan State University.

Olortegui-Yume, J.A. and Kwon, P.Y., 2010, "Crater Wear Patterns analysis on Multi-layer Coated Carbides Using the Wavelet Transform," *Wear,* Vol. 268, pp. 493-504.

Ozel, T. and Zeren, E., 2005, "Finite Element Modeling of Stresses Induced By High Speed Machining with Round Edge Cutting Tools," *Proceedings of IMECE'05,* Orlando, Florida, pp. 1-9.

PalDey, S., and Deevi, S.C., 2003, "Single layer and multilayer wear resistant coatings of (TiAl)N: A Review," *Material Science and Engineering A*, Vol. 342, pp. 58-79.

Park, K-H, Olortegui-Yume, J., Joshi, S., Kwon, P., Yoon, M-C, Lee, G-B and Park, S-B, 2008, "Measurement of Droplet size and volumes for Minimum Quantity Lubrication (MQL)," *International Conference on Smart Manufacturing Application*, Gyeonggi-do, Korea.

Park, K.-H. and Kwon, P.Y., 2009, "Flank Wear of Multi-layer Coated Tool and Wear Prediction Using Abrasive Wear Model," *Proceedings of the 2009 ASME International Manufacturing Science and Engineering Conference*, West Lafayette, Indiana, USA.

Park, K.-H., Kwon, P.Y., Castro, G., Kim, D. and Lantrip, J., 2010, "Preliminary study on tool wear in drilling of composite/titanium stacks with carbide and PCD tools," *Transaction of NAMRII/SME*, Vol. 38, pp. 283-290.

Park, K.-H., Shantanu, J., Kwon, P., Drazl, L.T. and Do, I., 2010, "Minimum quantity lubrication (MQL) with nanographene-enhanced lubricates: Ball-milling experiment," *Transaction of NAMRI/SME*, Vol. 38, pp. 81-88.

Park, K.-H., Olortegui-Yume, J., Yoon, M.-C and Kwon, P., 2010, "A study on droplets and their distribution for minimum quantity lubrication (MQL)," *International Journal of Machine Tools & Manufacture,* Vol. 50, pp. 824-833.

Pinkerton, H., 1928, "The reaction to oils and fats in the lung," *Arch Pathology*, Vol. 5, pp. 380–401.

Rabinowicz, E, 1964, "Friction and wear of materials," *John Wiley and Sons Inc.*, 2nd Edition.

Rahman, M., Kumar, A.S. and Salam, M.U., 2002 "Experimental evaluation on the effect of minimal quantities of lubricant in milling," *International Journal of Machine Tools and Manufacture*, Vol. 42, pp. 539-547.

Rahim, E.A., and Sharif, S., 2007, "Tool failure modes and wear mechanism of coated carbide tools when drilling Ti-6Al-4V," *Int. J. Precision Technology*, Vol. 1, No. 1, pp. 30-39.

Raja, J., Muralikrishnan, B. and Fu, S., 2002, "Recent advances in separation of roughness, waviness and form," *Transactions of the ASME*, Vol. 26, pp 222-235.

Ramalingam, S. and Wright, P. K., 1981, "Abrasive wear in machining: experiment with material of controlled microstructure," *Journal of Engineering Materials and Technology*, Vol. 103, pp. 151-156.

Ramulu, M., Faridinia, M., Garbini, J.L. and Jorgensen, J.E., 1991, "Machining of Graphite/Epoxy Composite Material with Polycrystalline Diamond (PCD) Tools," *ASME J. Eng Materials and Technology*, Vol. 113, No. 4, pp. 430-436.

Ramulu, M., Young, P. and Kao, H., 1999, "Drilling of Graphite/Bismaleimide Composite Material," *Journal of Materials Engineering and Performance*, Vol.8, No.3, pp. 330-338.

Ramulu, M., Branson, T. and Kim, D., 2001, "A Study on the Drilling of Composite and Titanium Stacks," *Composite Structures*, Vol. 54, pp. 67-77.

Rawat, S. and Attia, H., 2009, "Wear mechanisms and tool life management of WC–Co drills during dry high speed drilling of woven carbon fibre composites," *Wear*, Vol. 267, No.5-8, pp. 1022-1030.

Raynor, P. C., Kim, S. W. and Bhattacharya, M., 2005, "Mist generation from metalworking fluids formulated using vegetable oils," *Annals of Occupational Hygiene*, Vol. 49, pp. 283-293.

Reddy, N.S.K. and Rao, P.V.R., 2006, "Experimental investigation to study the effect of solid lubricants on cutting forces and surface quality in end milling," *International Journal of Machine Tools & Manufacture*, Vol. 46, pp. 189-198.

Rioul, O. and Vetterli, M., 1991, "Wavelet and signal processing," *Signal Processing Magazine IEEE,* Vol. 8, pp. 14-38.

Sadik, M.I. and Myrtveit, T., 2009, "The Performance of PVD Coated Grade in Milling of ADI 800," *World Academy of Science Engineering and Technology*, Vol. 53, pp. 527-530.

Sanjaya, C., Neemab, M.L. and Chinc, C.W., 2005, "Modeling of tool wear in drilling by statistical analysis and artificial neural network," *Journal of Materials Processing Technology*, Vol 170, Issue 3, pp. 494-500.

Sharif, S. and Rahim, E.A., 2007, "Performance of coated-and uncoated-carbide tools when drilling titanium alloy-Ti-6Al4V," *Journal of materials processing technology*, Vol. 185, No. 1-3, pp. 72-76.

Sharma, B.K., Adhvaryu, A. and Erhan, S.Z., 2009, "Friction and wear behavior of thioether hydroxyl vegetable oil," *Tribology International*, Vol. 42, pp. 353-358.

Sharma, V.S., Dogra, M. and Suri, N.M., 2009, "Cooling techniques for improved productivity in turning," *International Journal of Machine Tools and Manufacture*, Vol. 49, pp. 435-453.

Shen, B., Malshe, A.P., Kalita, P. and Shih, A.J., 2008, "Performance of Novel MoS2 Nanoparticles Based Grinding Fluids in Minimum Quantity Lubrication Grinding," *Transaction of NAMRI/SME*, Vol. 36, pp. 357-364.

Shoskes, M., Banfield, W.G. and Rosenbaum, S.J., 1950, "Effect and fate of oil aerosol particles retained in the lungs of mice," *A.M.A. Archives of Industrial Hygine and Occupational Medicine*, Vol. 1, pp. 20–35.

Sodergberg, S., Sjostrand, M. and Ljungberg, B., 2001, "Advances in coating technology for metal cutting tools," *Metal Powder Report*, Vol. 56, pp.24-30.

Sokovic, M., Kopac, J., Dobrzanski, L.A. and Adamiak, M., 2004, "Wear of PVD-coated solid carbide end mills in dry high-speed cutting," *Journal of Materials Processing Technology*, Vol. 157-158, pp. 422-426.

Sreejith, P.S. and Ngoi, B.A., 2000, "Dry machining: Machining of the future," *Journal of Materials Processing Technology*, Vol. 101, No.1-3, pp. 287-291.

Stephenson, D.A. and Agapiou, J.S., 2006, "Metal Cutting Theory and Practice," *Taylor & Francis*, 2nd Edition.

Suda, S., Yokota, H., Inasaki, I. and Wakabayashi, T., 2002, "A synthetic ester as an optimal cutting fluid for minimal quantity lubrication machining," *CIRP Annals*, Vol. 51, pp. 95-98.

Tao, X., Jiazheng, Z. and Kang, X., 1996, "The ball-bearing effect of diamond nanoparticles as an oil additive," *Journal of Physics D: Applied Physics*, Vol. 29, pp. 2932-2937.

Tasdelen, B., Wikblom, T. and Ekered, S., 2008, "Studies on minimum quantity lubrication (MQL) and air cooling at drilling," *Journal of Materials Processing Technology*, Vol. 200, pp. 339-346.

Teti, R., 2002, "Machining of composite materials," *CIRP ANNALS, Manufacturing Technology*, Vol. 51, pp. 611-634.

Thornburg, J. and Lieth, D., 2000, "Size distribution of mist generated during metal machining," *Applied Occupational and Environmental Hygiene*, Vol. 15, pp. 618-628.

Trent, E.M., 1963, "Cutting steel and iron with cemented carbide tools – Part I: An Analysis of Tool Wear," *Journal of the Iron and Steel Institute*, Vol. 201, pp. 847-855.

Tsao, C.C., 2008, "Prediction of thrust force of step drill in drilling composite material by Taguchi method and radial basis function network," *International Journal of Advanced Manufacturing Technology*, Vol. 36, pp. 11–18.

Ueda, T., Hosokawa, A. and Yamada, K., 2006, "Effect of oil mist on tool temperature in cutting," *Journal of Manufacturing Science and Engineering*, Vol. 128, pp. 130-135.

Upadhyay, P.C. and Lyons, J.S., 1999, "On the Evaluation of Critical Thrust for Delamination-free Drilling of Composite Laminates," *Journal of Reinforced Plastics and Composites,* Vol. 18, pp. 1287–1303.

Varadarajan, A.S., Philip, P.K. and Ramamoorthy, B., 2002, "Investigations on hard turning with minimal cutting fluid application (HTMF) and its comparison with dry and wet turning," *International Journal of Machine Tools and Manufacture*, Vol. 42, pp. 193-200.

Wakabayashi, T., Inasaki, I. and Suda, S., 2006, "Tribological action and optimal performance: Research activities regarding MQL machining fluids," *Machining Science and Technology*, Vol. 10, pp. 59-85.
Wang, D.-Y., Chang, C.-L., Wong, Y.-W., Li, Y.-W., and Ho, Y.-Y., 1999, "Improvement of the interfacial integrity of (Ti,Al)N hard coatings deposited on high speed steel cutting tools," *Surface and Coatings Technology*, Vol. 120-121, pp. 388-394.

Weinert, K. and Kempmann, C., 2004, "Cutting temperatures and their effects on the machining behavior in drilling reinforced plastic composites," *Advanced Engineering Materials*, Vol. 6, pp. 684-689.

Weinert, K., Inasaki, I., Sutherland, J.W. and Wakabayashi, T., 2004, "Dry machining and minimum quantity lubrication," *CIRP Annals*, Vol. 53, pp. 511-537.

Whitehouse, D.J., 2002, "The Handbook of Surface and Nanometrology," *Taylor & Francis*, 1st Edition.

Wong, T., Kim, W. and Kwon, P.Y., 2004, "Experimental support for a model-based prediction of tool wear," *Wear*, Vol. 257, pp. 790–798.

Wright, P.K. and Bagchi, A., 1981, "Wear Mechanisms that Dominate Tool-Life in Machining," *Journal of Applied Metal Working*, Vol. 1, No. 4, pp.15-23.

XG Science, Inc. http://www.xgsciences.com/products/about-xgnp.php

Xu, J., Zhu, M.H. and Zhou, Z.R., 2004, "Fretting wear behavior of PTFE-based bonded solid lubrication coatings," *Thin Solid Films*, Vol. 457, pp. 320-325.

Yang, X. and Liu, C.R., 1999, "Machining titanium and its alloys," Machining *Science and Technology*, Vol. 3, pp. 107-139.

Yen, Y.-C., Jain, A., Chigurupati, P., Wu, W.-T. and Altan, T., 2004, "Computer Simulation of Orthogonal Cutting Using a Tool with Multiple Coatings," *Machining Science and Technology*, Vol. 8, pp. 305-326.

Yoshimura, H., Itoigawa, F., Nakamura, T. and Niwa, K., 2005, "Development of nozzle system for oil-on-water droplet metalworking fluid and its application to practical production line," *JSME International Journal,* Vol. 48, pp. 723-729.

Zhang, L.B., Wang, L.J. and Liu. X.Y., 2001, "Mechanical Model for Predicting Critical Thrust Forces in Drilling Composite Laminates," *Proceedings of the Proceedings of the Institution of Mechanical Engineers Part B Journal of Engineering Manufacture,* Vol. 215, pp. 135–146.

Zhang, P.F., Churi, N.J., Pei, Z.J. and Treadwell, C., 2008, "Mechanical drilling processes for titanium alloys: A literature review," *Machining Science and Technology*, Vol. 12, pp. 417-444.

Zhao, S., Zhang, J., Weng, D. and Wu, X., 2003, "A method to form well-adhered    -Al$_2$O$_3$ layers on FeCrAl metallic supports," *Surface and Coatings Technology*, Vol. 167, pp. 97-105.

Zhu, L. and Wang, J., 2006, "A study on titanium alloys deep-hole drilling technique," *Material Science Forum*, Vol. 532-533, pp. 945-948.

Zitoune, R., Krishnaraj, V. and Collombet, F., 2010, "Study of drilling of composite material and aluminum stack," *Composite Structures*, Vol. 92, pp. 1246-1255.